Numerical investigation of solar energetic particle transport between the Sun, Earth, and Mars

PKN Heita

orcid.org 0000-0002-9827-5197

Dissertation submitted in fulfilment of the requirements for the degree *Master of Science in Astrophysical Sciences* at the North-West University

Supervisor: Prof RDT Strauss

Graduation May 2019

29915554

Man is an artifact designed for space travel.
He is not designed to remain in his present biologic state
any more than a tadpole is designed to remain a tadpole.

William S. Burroughs

Abstract

Solar energetic particles pose a danger to spacecraft electronics, and even more significantly, to a future spacecraft crew beyond the Earth's magnetosphere. Given the current NASA and SpaceX interest in interplanetary space travel, solar energetic particles have therefore become the focus of much space physics and space weather research. Noting the frequent use of the Hohmann transfer (*Hohmann*, 1925) in interplanetary space travel, this study, assuming the Hohmann-Parker effect (*Posner et al.*, 2013) addresses the propagation of potentially harmful 4 and 32 MeV protons along a Hohmann transfer trajectory between Earth and Mars. This is done using a one-dimensional finite-difference solar energetic particle transport model based on the *Roelof* (1969) equation. Different finite-difference numerical schemes/techniques are investigated, whereafter the model is compared to various contemporary models to establish its validity. An investigation into the spatial (z coordinate) and radial (r coordinate) dependence of the solar energetic particle peak intensities, anisotropies, and the so-called time of maximum, is presented. It is shown that the peak intensities and anisotropies along the Hohmann transfer display a power-law decrease, and that the peak intensities have an average functional form of $\sim z^{-1.06}$, which is found to decrease if smaller radial mean free path values are used. The peak anisotropies are found to have a functional form of $\sim z^{-0.18}$. The corresponding radial dependence of the solar energetic particle peak intensities is shown to have an average functional form of $\sim r^{-1.74}$, which is in consensus with the numerical studies of *Lario et al.* (2007) and *He et al.* (2017), and encouragingly, with the observational study of *Lario et al.* (2013). Assuming 4 MeV protons and varying scattering conditions, it is shown that a spacecraft crew halfway to Mars, along the Hohmann transfer trajectory, will have a "warning time" of approximately one hour once an SEP event peaks at Earth.

Keywords:

`Solar energetic particles, Finite-difference methods, Hohmann transfer, Hohmann-Parker effect, Space weather, Interplanetary travel`

Acronyms and Abbreviations

Listed below are abbreviations used in the text. For the purposes of clarity, they are written out in full when they appear for the first time in the text.

1D	One Dimensional
2D	Two Dimensional
AU	Astronomical Unit (1 AU = 1.49×10^8 km)
SEP	Solar Energetic Particle
eV	electron Volt (1eV = 1.60×10^{-19} J; 10^3 eV = 1 keV, 10^6 eV = 1 MeV, 10^9 eV = 1 GeV)
CIR	Co-Rotating Interaction Region
CME	Coronal Mass Ejection
HCS	Heliospheric Current Sheet
HMF	Heliospheric Magnetic Field
SW	Solar Wind
GLE	Ground Level Enhancement
QLT	Quasi-Linear Theory
TS	Termination Shock
PDE	Partial Differential Equation
PADC	Pitch-Angle Diffusion Coefficient
FD	Finite-Difference
FTCS	Forward Time Central Space
FTBS	Forward Time Backward Space
TVD	Total Variation Diminishing
LOD	Locally One-Dimensional
MSL	Mars Science Laboratory
ICD	Inner Connection Distance
OCD	Outer Connection Distance
GPR	Gaussian Process Regression

Contents

CHAPTER 1

Introduction

Solar energetic particles (SEPs) are particles (mostly electrons, protons, and alpha particles) that are generated in solar flares and/or at shocks driven by coronal mass ejections, resulting in suprathermal particles with energies from a few keV up to several GeVs. These high energy particle increases pose a danger to astronauts in space, can lead to the degradation of precious satellites and other Earth infrastructure, and even closer to home, they can result in a radiation hazard for airline passengers (see e.g., *Moldwin*, 2008).

The current NASA and SpaceX interest in interplanetary missions, aspirations of a Mars research base, and eventually a colony, has propelled SEP research to the forefront of space physics and space weather research. An important aspect of this research has been the spatial dependence of SEP peak intensities (see e.g., *McGuire et al.*, 1983; *Hamilton et al.*, 1990; *He et al.*, 2017), which is used to estimate the potential impact of SEPs on spacecraft and, more importantly, on the spacecraft crew on interplanetary space missions. It is worth noting that, to date, the most commonly used means of transferring spacecraft between two planetary orbits (Earth and Mars in this study) is the Hohmann transfer orbit (*Hohmann*, 1925). The latter involves accelerating a spacecraft onto an elliptical orbit between an inner and outer planet. *Posner et al.* (2013) found that a spacecraft undergoing a Hohmann transfer orbit has a strong tendency to remain magnetically well connected to either planet during different phases of the transfer, this circumstance they termed the Hohmann-Parker effect. Using the Hohmann-Parker effect (*Posner et al.*, 2013), this study addresses the one-dimensional propagation of SEPs along these transfer orbits by numerically solving the *Roelof* (1969) equation by means of finite-difference methods. This is done to obtain power-law functional forms for both the peak intensities and anisotropies encountered by a spacecraft fleet positioned along the Hohmann transfer orbit.

The study is structured in the following manner:

In Chapter 2, the necessary background and context for the present study is provided. This includes an introduction to solar activity (flares, coronal mass ejections, and the solar wind), and the *Parker* (1958) heliospheric magnetic field (HMF), which modulates SEP intensities and fluences within the inner heliosphere. Solar energetic particles, their classification, sources, and the various turbulence models used to describe turbulent particle transport are discussed. Lastly, an overview of SEP transport, as described by the *Roelof* (1969) equation, along with the relevant SEP transport mechanisms assumed in this study (1D streaming along the mean HMF, focusing in diverging field lines, and pitch-angle scattering), is given.

In Chapter 3, a brief introduction to finite-difference (FD) methods and general second-order partial differential equations is given. The FD method is applied to the diffusion and advection equations, paying close attention to numerical stability and diffusiveness. In this study, the Forward-Time Central Space (FTCS), Lax-Wendroff, and the Forward Upwind schemes are considered. Lastly, Flux-limiters (see e.g., *Trac and Pen*, 2003) such as the van Leer, Minmod, and Superbee, used in minimizing the diffusiveness present in the Forward Upwind scheme, are discussed, and a new limiter, named Tan (due to its use of the tan trigonometric function), is developed.

Chapter 4 examines the mathematical aspects of the SEP transport model used in this study, along with key assumptions and relevant SEP transport coefficients. The various mathematical terms (1D streaming along the mean HMF, focusing, and pitch-angle scattering), as encompassed in the *Roelof* (1969) equation, are described along with their finite-difference numerical implementation. The chapter also gives an outline of the standard model parameters and the corresponding values assumed for this study.

The finite-difference numerical model is compared to various contemporary models in Chapter 5, with the goal of obtaining the best flux-limiter combinations for both the distance along the magnetic field line z and the pitch-angle cosine μ coordinates. The model characteristics with respect to an electron SEP event are also discussed.

Having passed validation, the numerical model is applied to the study of SEP propagation along Hohmann transfer orbits in Chapter 6. The Hohmann-Parker effect (*Posner et al.*, 2013) is introduced, along with a discussion of its scientific implications. Simulation results for virtual spacecraft, positioned at varying distances along the Hohmann transfer, are presented and analysed. The spatial dependences of the peak intensities and anisotropies and the radial dependence of the peak intensities arising from the simulation results is investigated. Conclusions are drawn regarding the functional forms $z^{-\alpha}$ and $r^{-\alpha}$, and $z^{-\beta}$ of the peak intensities, anisotropies, the so-called time of maximum, and the "warning time".

Chapter 7 provides a summary of the work presented in this study, along with the key conclusions drawn from its results.

CHAPTER 2

The Inner Heliosphere and Energetic Particles

2.1 Introduction

The Sun moves through the galactic medium, "dragging" the Earth, Mars, and other objects in the solar system along with it. This thermonuclear fireball continuously ejects large quantities of particles radially into space, forming the solar wind, which flows out into all directions with the Sun's turbulent magnetic field embedded in it. The magnetic bubble arising from the outwards radial motion of the solar wind is called the heliosphere (from the Greek word "helios" meaning Sun ; *Parker* 1958). In this chapter, various aspects of solar activity, including sunspots, solar flares, coronal mass ejections (CMEs), the high-speed solar wind, and the heliospheric magnetic field (HMF) will be discussed. Furthermore, the modulation of solar energetic particles (SEPs) within the inner heliosphere, and the various processes that govern their propagation as encompassed in the *Roelof* (1969) equation shall also be considered, with a primary focus on particle streaming along the magnetic field line, focusing associated with diverging field lines, and the scattering of particles at magnetic field irregularities.

2.1.1 Sunspots and Solar Flares

Sunspots are dark visible patches that appear on the Sun's surface (see Figure 2.1). They occur mostly at latitudes between 40°N and 40°S (*Hathaway*, 2010). The dark patches can be attributed to the temperature of the sunspots being much lower compared to the surface temperature of the Sun, $\sim$ 4000 K (*Meyer-Vernet*, 2007). Magnetic field strengths inside the sunspots can vary from a few hundred to several thousand times the intensity of the surrounding field (*Meyer-Vernet*, 2007).

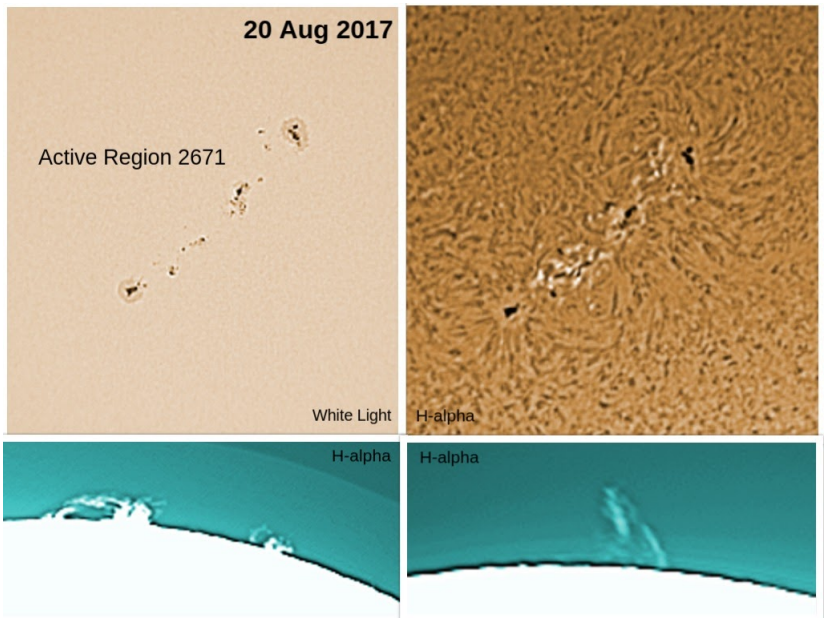

Figure 2.1: *Sunspots and solar filaments on the surface of the Sun. The bottom panels show sunspots in white light and H-alpha respectively, whereas the lower panels show solar filaments being ejected from the surface of the Sun. Credit: http://www.nwuheliolab.co.za/.*

To better grasp the essential mechanisms behind the formation of sunspots, it is vital to note that matter revolves faster at lower latitudes in contrast to higher latitudes and even faster near the interior of the Sun's surface (*Snodgrass*, 1983). These rotations result in complex magnetic field structures forming as a result of the distorted field lines. As the field lines increase in density, a pore forms on the surface, resulting in the formation of intense magnetic field flux tubes perpendicular to the surface (*Phillips*, 1992). These intense field lines limit/suppress effective cross-field heat conduction, resulting in a drop of temperature and eventually the formation of a sunspot. It is worth noting that convection and tacholine transition in the Sun's interior are also critical to sunspot formation, and that differential rotation is only one part of the story.

Sunspot numbers are intrinsically dependent on solar activity, i.e. during periods of low activity, there are few or no sunspots, whereas active periods, as shown in Figure 2.1, yield a higher number of sunspots.

In Figure 2.2, it is evident from the observations that the Sun has an almost periodic ~ 11 year solar cycle (*Schwabe*, 1843), characterized by periods of solar maximum and minimum. Magnetic polarities of the sunspots alternate between negative and positive, from one ~ 11 year cycle to the next. This is known as Hale's polarity law (*Hale*, 1908).

2.1.2 Coronal Mass Ejections

CMEs, as shown in Figure 2.3, were discovered at the dawn of the 1970s (*Tousey* 1973 ; *MacQueen et al.* 1974). CMEs are quite often related to solar flares, however they have been observed to occur in

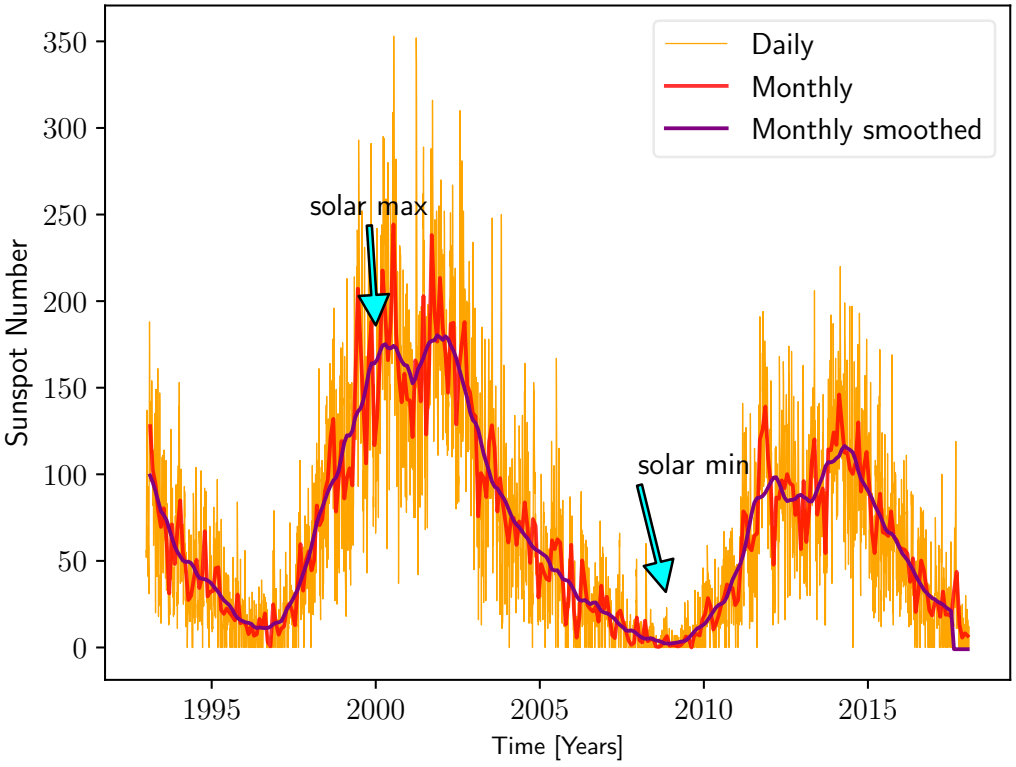

Figure 2.2: *Daily and monthly sunspot numbers, from the year 1993 to early 2018. Data From: SILSO data/image, Royal Observatory of Belgium, Brussels.*

the absence of solar flares. They are characterized by an expulsion ranging from speeds of 20 km·s^{-1} to well over 3000 km·s^{-1} (*Manchester et al.*, 2006) of plasma and magnetic field from the corona into the solar wind and eventually interplanetary space. To get a scale of how much plasma is released in these expulsions, imagine a "molten juice" with the volume of a quarter of a million Nimitz aircraft carriers ($\geq 10^{16}g$; *Antiochos et al.* 1999) being suddenly released from the corona.

2.2 The Solar Wind

The continuous outflow of solar material from the Sun was confirmed approximately six decades ago, when studies by *Biermann* (1951, 1957) showed that comets' tails consistently pointed radially away from the Sun. This outward flow was initially called *solar corpuscular* radiation, and later *Parker* (1958) introduced the name solar wind. He predicted the solar wind to be a supersonic flow of plasma into interplanetary space, assuming that, due to the high temperatures of $\sim 10^6$ K on the Sun's corona, the gravitational force would be inadequate to hold back solar particles. The prediction by *Parker* (1958) was eventually confirmed by *in situ* observations of the supersonic solar wind by various spacecraft (see e.g., *Gombosi*, 1998).

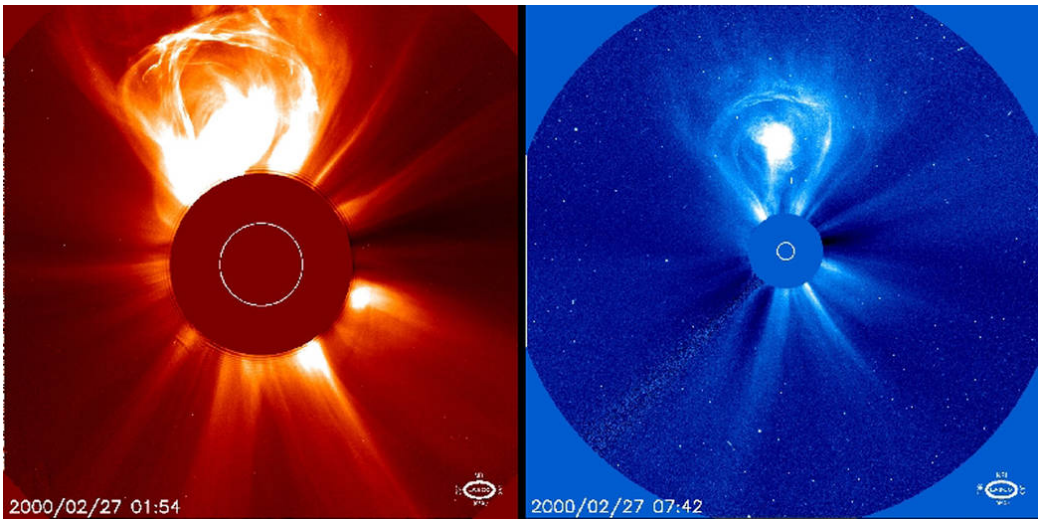

Figure 2.3: *A coronal mass ejection on Feb. 27, 2000 taken by SOHO LASCO C2 and C3. Credit: SOHO, ESA, and NASA.*

The solar wind, and various electromagnetic waves are for the most part emitted from the photosphere, which is the visible surface of the Sun. Local magnetic field lines on the Sun that are a result of plasma convection, connect the local North and South poles, along which plasma travels. The solar wind carries the magnetic field lines embedded within it to the outer regions of the Sun and on into interplanetary space without the magnetic field lines disconnecting from the Sun's surface. Once the magnetic field lines detach from the Sun's surface, the magnetic field is called the interplanetary magnetic field (IMF; discussed in section 2.4). The solar wind blows out at speeds of 300 - 800 km·s^{-1} and primarily consists of protons with energies ranging from 0.5 - 3 keV (*Reames*, 2004).

The launch of the Ulysses spacecraft in the year 1990 allowed for measurements to be taken over the polar regions of the Sun. From these observations (see e.g., *McComas et al.*, 2000) it was established that the solar wind speed is latitude-dependent and consists of two regimes, namely the fast and slow solar wind, as shown in both Figure 2.4, and the top panel of Figure 2.5.

These two regimes are mainly attributed to the Sun's complex magnetic field at different points on the solar surface. Close to the solar surface, magnetic field lines form loops during solar minimum conditions which connect two points on the solar surface, forming the so-called coronal streamer belts. These loops are oriented almost perpendicular to the radial outflow. The orientation of the streamer belts causes them to act as a barrier to the radially out-flowing solar wind, limiting its speed to $\sim$ 400 km·s^{-1}. Several studies have also suggested that the edges of coronal holes may result in a slow solar wind (see e.g., *Smith*, 2000; *Ofman*, 2004; *Schwenn*, 2006; *Wang*, 2011).

In contrast to the solar equatorial regions, the polar regions are distinguished by low density regions in the corona called coronal holes. Coronal holes are characterized by open magnetic field lines extending into interplanetary space. These magnetic field lines are directed parallel to the out-flowing solar wind and so do not inhibit its radial outflow but rather assist it, giving rise to the fast solar wind (see e.g.,

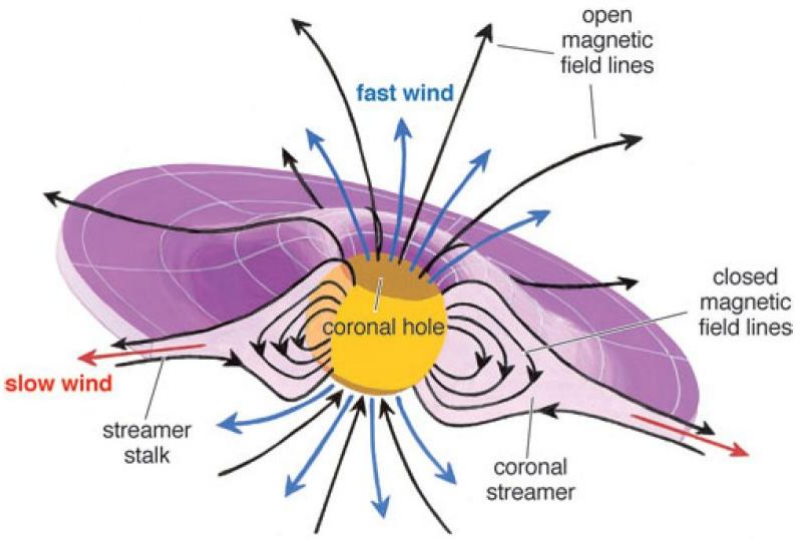

Figure 2.4: *Illustration of the role of coronal holes and the magnetic field in producing the fast and slow solar wind. Slow wind (red) emanates from the edge of coronal holes, flowing along the streamer belts, whereas the fast solar wind (blue) emanates from coronal holes along parallel magnetic field lines. Figure taken from http://www.americanscientist.org.*

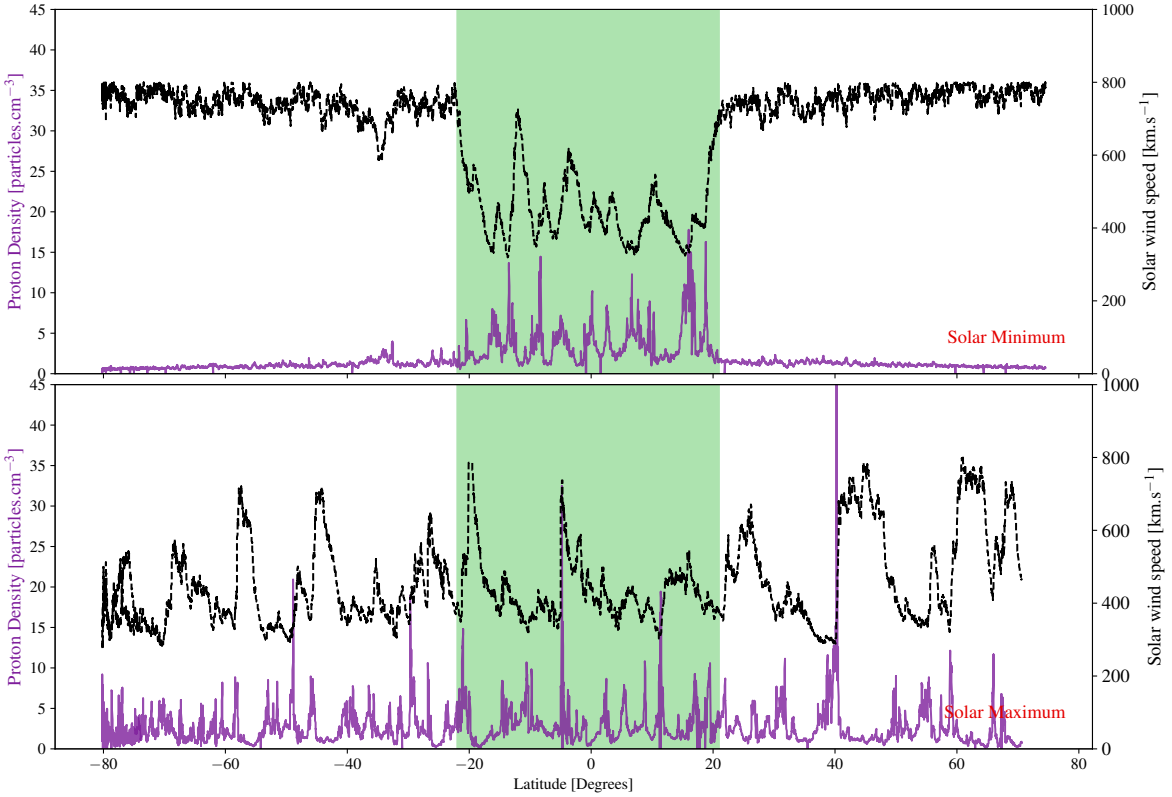

Figure 2.5: *Ulysses spacecraft observations of the solar wind speed and proton density, during periods of solar minimum (top panel, September 1994 - July 1995) and maximum (bottom panel, October 2000 - September 2001), respectively. Data from http://cohoweb.gsfc.nasa.gov.*

Cranmer, 2009; *Wang*, 2009). The fast solar wind has a characteristic speed of ~ 800 km·s^{-1}. During solar maximum periods the latitude dependence of the solar wind is not discernible, as shown in the bottom panel of Figure 2.5.

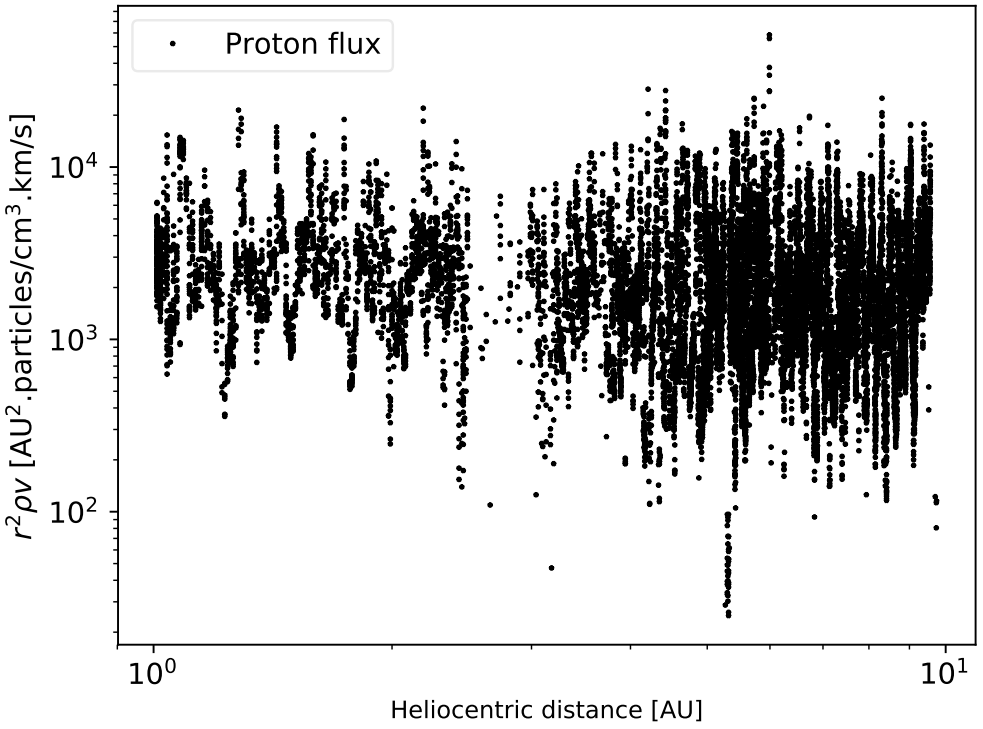

Figure 2.6: *The product of solar wind speed, the proton density and the square of the heliocentric distance is found to be constant with heliocentric distance (see, e.g., Gazis, 1984). Voyager 1 data from: http: // cohoweb.gsfc.nasa.gov/.*

It can also be seen in the top panel of Figure 2.5 that the proton density rises with a decrease in solar wind speed. To make sense of this, consider the continuity equation in spherical coordinates, along with the assumption of a temporally constant proton density, i.e.

$$\frac{1}{r^2}\frac{\partial}{\partial r}\left(r^2 \rho v\right) = 0, \tag{2.1}$$

which implies that

$$r^2 \rho v = \text{constant}, \tag{2.2}$$

which can be readily confirmed, as shown in Figure 2.6, using Voyager 1 data (in this case from the launch day on September 1977 to the year 1980). The spacecraft heliocentric distance (AU) is taken as r, the proton density (particles·cm^{-3}) as ρ and v is taken to be the proton flow speed (km·s^{-1}).

The radial extent of the solar wind marks the frontier of the region defined by the Sun's plasmatic influence. This region is called the heliosphere. The Sun's gravitational influence on the other hand extends much further outwards (Oort cloud). As the solar wind expands outwards, it interacts with interstellar matter, slowing down to subsonic speeds, until it can no longer push back the interstellar

medium. This results in a solar wind termination shock (TS; *Choudhuri* 1998). Voyager 1 and 2 observations places this boundary at approximate distances of 94 and 84 AU, respectively (*Stone et al.*, 2008). Beyond the TS lies the Heliopause, which marks the boundary between solar wind and interstellar plasma.

2.3 Corotating Interaction Regions

With increasing heliocentric distance, the fast and slow solar wind regimes, embedded with varying magnetic fields, become radially aligned. The fast solar wind stream slams into the slower moving wind ahead of it. This leads to a forward shock in front of the high speed stream, and a reverse shock on the trailing edge of the slow wind stream (*Parker*, 1963; *Hundhausen*, 1972; *Gosling and Pizzo*, 1999). The different properties of the respective streams, such as the magnetic field lines embedded in them, prevent the two streams from merging, thus forming an interaction region (IR). High pressure interaction regions (bounded by the forward and reverse shocks) that are stable enough to last over several solar rotations are called corotating interaction regions (CIRs; *Smith and Wolfe* 1976).

CIRs are usually identified from stream interfaces, which are characterized by a sudden change in entropy, a drop in particle density, and a rather significant increase in proton temperature (see e.g., *Belcher and Davis*, 1971; *Burlaga*, 1974; *Gosling et al.*, 1978).

2.4 The Heliospheric Magnetic Field

When the magnetic field lines are dragged into interplanetary space, they form part of the so called interplanetary magnetic field or heliospheric magnetic field (HMF). The HMF spans the entire heliosphere, governing the modulation of cosmic rays, energetic and solar particles (*Manuel*, 2013). Several models of the HMF have been proposed (for a review see *Hitge and Burger*, 2010). This section will primarily focus on the Parker spiral field.

2.4.1 The Parker Heliospheric Magnetic Field

The Sun's magnetic field lines become radial at a heliocentric distance of $\sim 2.5\mathrm{r}_\odot$, marking the source surface (see e.g., *Wang and Sheeley*, 1995; *Lockwood and Stamper*, 1999). The basic assumption is that the field lines are dragged into interplanetary space after which the Sun's rotation winds the HMF lines into a spiral, called the Parker spiral (*Parker*, 1958). Parker's analytical description of the HMF is given as

$$\mathbf{B} = B_o \left(\frac{r_o}{r}\right)^2 \left(\mathbf{e}_r - \frac{\omega_\odot (r - r_\odot)\sin\theta}{v_{sw}}\mathbf{e}_\phi\right), \tag{2.3}$$

with B_o being the HMF magnitude at Earth, ~ 5 nT at solar minimum, $r_o = 1$ AU, and the radial and azimuthal directions are denoted by unit vector components $\mathbf{e}_r$ and $\mathbf{e}_\phi$, respectively.

The Parker spiral angle ψ is defined as the angle between the radial direction and the average HMF at a given point. The spiral angle gives a measure of the extent to which the HMF has been wound up. Mathematically the spiral angle takes the form

$$\tan\psi = \frac{\omega_\odot (r - r_\odot)\sin\theta}{v_{sw}}, \tag{2.4}$$

where $\omega_\odot$ is the synodic rotation rate of the Sun, θ is the polar angle, r is the heliocentric radial distance, $r_\odot$ the radius of the Sun, and v_{sw} the radial solar wind speed.

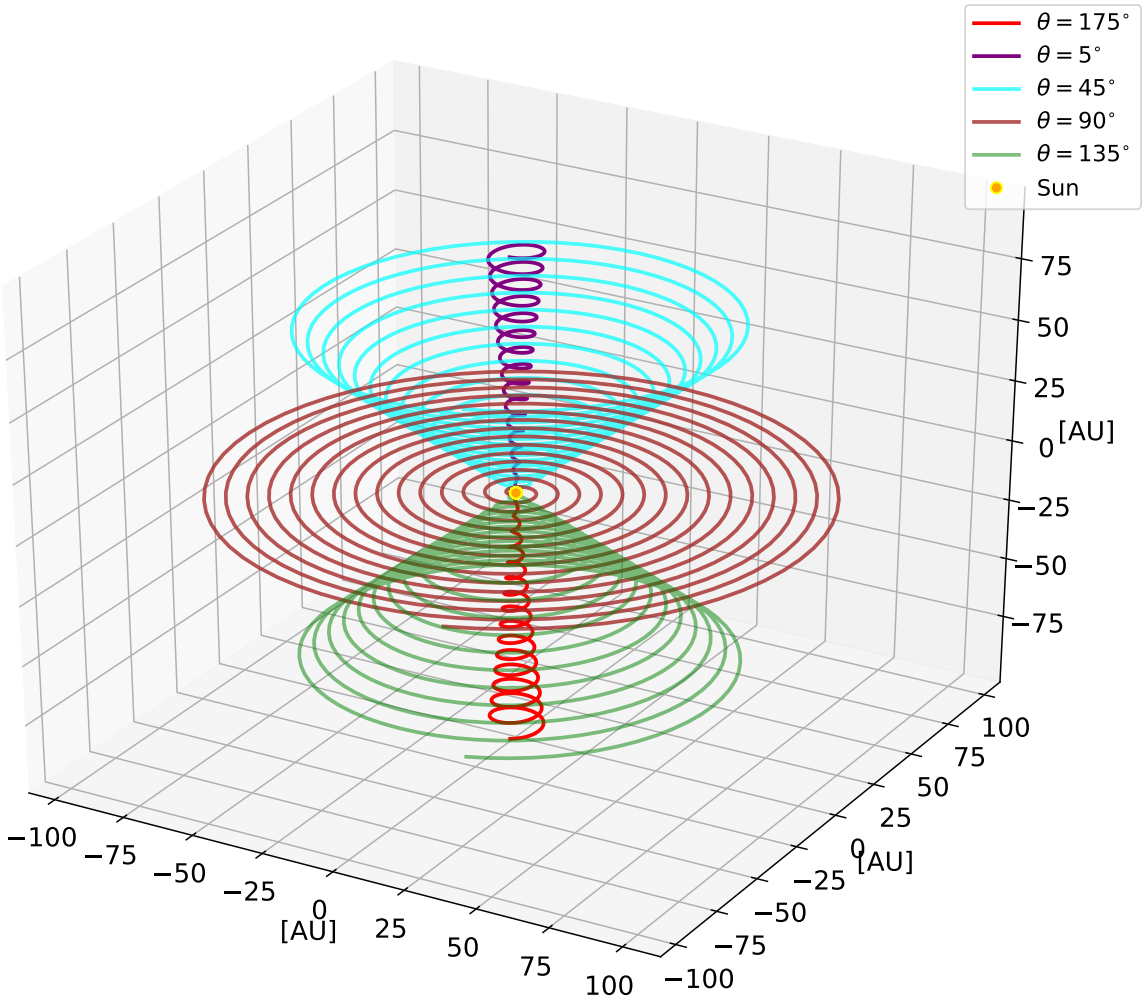

Figure 2.7: *Parker (1958) magnetic field lines for five different latitudes. Values used are* $r_\odot \approx 0.005$ AU, $\omega_\odot = 2.67 \times 10^{-6}$ rad·s^{-1}, *and* $v_{sw} = 2.79 \times 10^{-6}$ AU·s^{-1}.

Figure 2.7 shows the Parker spiral emanating from the Sun for different polar angles, i.e. 5° (purple), 45° (cyan), 90° (brown), 135° (green) and 175° (red), as similarly shown by *Manuel* (2013). Spacecraft observations have confirmed the presence of a Parker spiral HMF at mid to low latitudes (see e.g., *Thomas and Smith*, 1980; *Bruno and Bavassano*, 1997). However, its structure at the polar regions is still being debated (see e.g., *Smith*, 2011; *Sternal et al.*, 2011).

2.4.2 The Heliospheric Current Sheet

The heliospheric current sheet (HCS) marks the boundary between oppositely-directed open magnetic field lines emanating from the northern and southern hemispheres of the Sun. This boundary stretches out into interplanetary space, essentially dividing the heliosphere into two magnetic halves of opposite magnetic polarity as shown in Figure 2.8. At 1 AU the thickness of the current sheet is $\sim$ 10000 km (*Smith*, 2001).

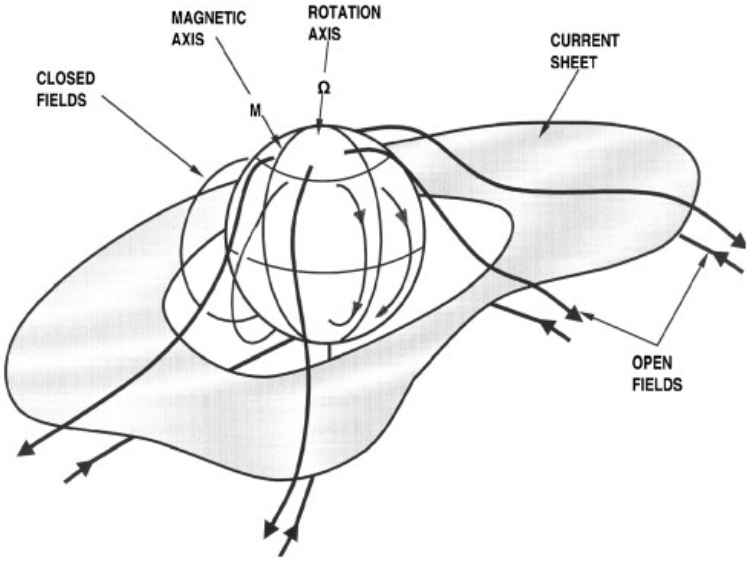

Figure 2.8: *A schematic illustration of the HCS. The magnetic and rotation axes of the Sun are also shown. Figure taken from Smith (2001).*

The shape of the HCS (see Figure 2.9) is largely influenced by a combination of solar rotation, wind speed, and the tilt angle, and is thus strongly correlated with solar activity. Solar maximum conditions see an increase of the tilt angle to $\sim 75°$, resulting in a very wavy structure propagating outwards, whereas solar minimum conditions see a decrease in tilt angle to $\sim 5°$ - $10°$, reducing the waviness of the structure (*Burger et al.*, 2008). In most cases the current sheet is so wavy that observers within the ecliptic plane sample both negative and positive polarities (*Posner et al.*, 2013).

The radially out-flowing solar wind drags both the HMF and HCS out into interplanetary space (see Figure 2.10). Depending on the solar wind speed variations within the ecliptic plane, the HCS reacts accordingly, i.e. fast solar wind speeds result in a less wavy current sheet in contrast to slow solar wind speeds (see e.g., *Balogh and Smith*, 2001; *Riley et al.*, 2002; *Czechowski et al.*, 2010). One equation describing the HCS for constant and radial solar wind speed was derived by *Jokipii and Thomas* (1981) and is given by,

$$\theta' = \frac{\pi}{2} + \sin^{-1}\left(\sin\left(\alpha_T\right)\sin\left[\phi + \frac{\omega_\odot(r - r_\odot)}{v_{sw}}\right]\right), \tag{2.5}$$

with θ' being the polar angle of the HCS, α_T the tilt angle, and ϕ the azimuthal angle. For a small tilt angle, Equation (2.5) reduces to

$$\theta' \approx \frac{\pi}{2} + \alpha_T \sin\left[\phi + \frac{\omega_\odot (r - r_\odot)}{v_{sw}}\right]. \tag{2.6}$$

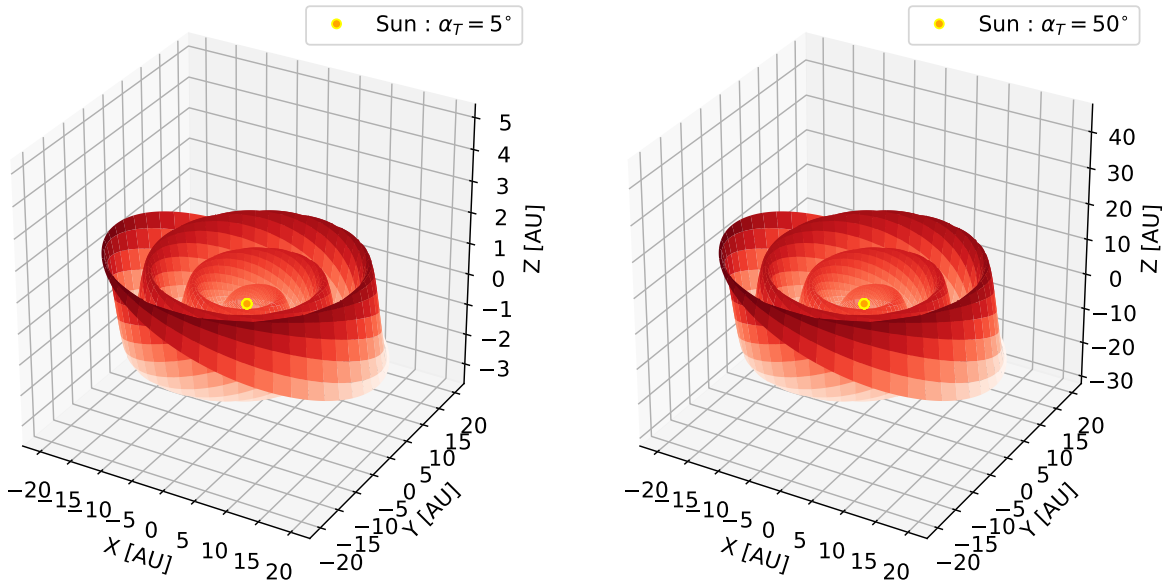

Figure 2.9: *Wavy heliospheric current sheet shown for two different tilt angles i.e., $\alpha_T = 5°$ (left panel) and $\alpha_T = 50°$ (right panel). A source surface $r_\odot = 0.005$ AU was used, solar wind speed, $v_{sw} = 400$ km·s^{-1}, and an equatorial rotation rate ($\omega_\odot$), of 2.67×10^{-6} rads·s^{-1} in both cases.*

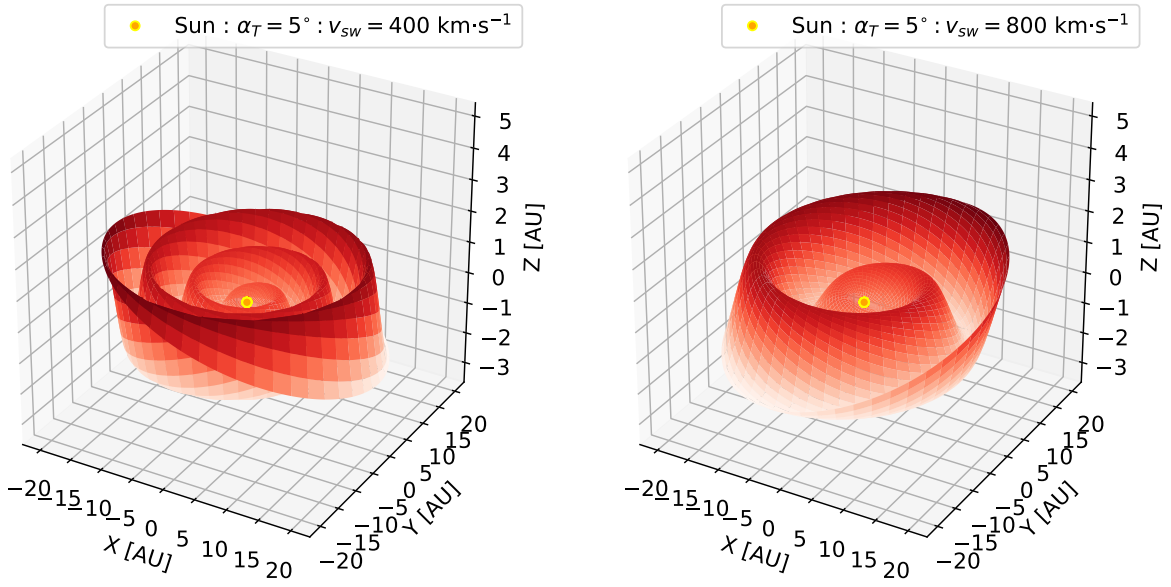

Figure 2.10: *Influence of solar wind speed, v_{sw}, on the heliospheric current sheet.*

In Figure 2.9, the significance of the tilt angle is clearly shown, with a tilt angle of 5° resulting in wavy structures extending to latitude distances (z-direction) of $\sim$ 2 AU (left panel), whereas an increase in the tilt angle to 50° causes the structures to extend to latitude distances of $\sim$ 20 AU (see right panel).

2.5 Energetic Particles

The interaction of energetic charged particles with the interplanetary medium reduces the original intensity of these particles: a process that is referred to as modulation. Cosmic ray species within the heliosphere can be grouped into various populations:

- Galactic cosmic rays (GCRs): GCRs originate in regions far beyond the Heliosphere. Blast waves from supernova remnants, pulsars, and active galactic nuclei (AGN) accelerate particles (for a review, see e.g., *Ellison and Reynolds*, 1991; *Axford et al.*, 1977; *Bell*, 1978), resulting in energy distributions from a few hundred keV all the way up to energies as high as $3{\times}10^{21}$ eV. Beyond $\sim 10^{15}$ eV, GCRs are assumed to be of extragalactic origin (see e.g., *Schlaepfer*, 2003; *Aharonian et al.*, 2012).

- Anomalous cosmic rays (ACRs): Charge exchange between interstellar neutral atoms and the radially outflowing solar wind results in the ionization of the neutral atoms, which are subsequently picked up by the outflowing solar wind. These particles are called pick-up ions (PUIs). The latter process leads to a PUI population at the heliospheric termination shock. Through diffusive shock acceleration, PUIs are accelerated out of this population and enter the heliosphere as ACRs (*Fisk et al.*, 1974; *Fichtner*, 2001; *Florinski and Pogorelov*, 2009; *Strauss et al.*, 2010). It is worth noting however that recent observations by both Voyager 1 and 2, while crossing the termination shock have put this long standing paradigm of ACR acceleration at the termination shock into question (see e.g., *Cummings and Stone*, 2013).

- Jovian electrons: The fly-by of Jupiter by the Pioneer 10 spacecraft in 1973 observed energetic particles with energies in excess of $\sim$ 30 MeV (*Simpson et al.*, 1974). The timing of these observations hinted at the magnetosphere of Jupiter as a strong source of energetic electrons (*Ferreira et al.*, 2001; *Ferreira*, 2002), termed Jovian electrons. These energetic electrons are continuously discharged into the interplanetary medium, dominating low energy electron/cosmic ray intensities in the inner heliosphere (see e.g., *Strauss et al.*, 2013).

- Solar energetic particles (SEPs): SEPs are particles (mostly electrons, protons and alpha particles) that are generated in a solar flare or at a shock driven by a CME, resulting in suprathermal particles with energies from a few keV up to several GeVs. SEPs are routinely observed at Earth during events lasting from several hours to several days (see e.g., *Balogh et al.*, 2008; *Usoskin*, 2008; *Dresing et al.*, 2014).

This study will focus on SEP propagation within the inner heliosphere.

2.5.1 Single Particle Motion

To better understand the transport of SEPs, it is essential to have a rudimentary understanding of the behaviour of individual charged particles in the inner heliosphere with respect to the solar wind plasma.

The motion of an energetic particle of charge q, mass m, and moving in interplanetary space at speed $\mathbf{v}$ (subject to electromagnetic fields $\mathbf{E}$ and $\mathbf{B}$) is governed by the Lorentz force $\mathbf{F}_L$,

$$\mathbf{F}_L = \frac{d(m\mathbf{v})}{dt} = q(\mathbf{E} + \mathbf{v} \times \mathbf{B}). \tag{2.7}$$

In the case of a uniform magnetic field $\mathbf{B}$ and negligible electric field $\mathbf{E} = 0$, the Lorentz force becomes

$$\mathbf{F}_L = q(\mathbf{v} \times \mathbf{B}), \tag{2.8}$$

which acts perpendicular to the velocity $\mathbf{v}$, changing the particle's direction while simultaneously keeping its kinetic energy constant. The velocity $\mathbf{v}$ is characterized by a parallel ($v_\parallel$) and perpendicular ($v_\perp$) component with respect to $\mathbf{B}$.

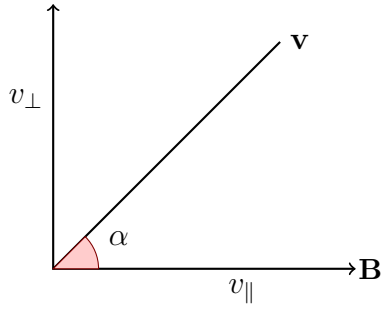

Figure 2.11: *Parallel and perpendicular velocity components, $v_\parallel$ and $v_\perp$.*

The angle α shown in Figure 2.11 is the so-called pitch-angle, defined as the angle that the particle's trajectory makes with the magnetic field line, and given as $\tan(\alpha) = v_\perp / v_\parallel$. The pitch-angle cosine, $\mu = \cos(\alpha)$, gives a measure of the extent of the particle's gyro-radius as projected onto the magnetic field direction.

As stated earlier, the circular motion of a charged particle is strictly a result of $v_\perp$ interacting with $\mathbf{B}$. The radius of the gyration motion, or more formally the Larmor radius (see Figure 2.12), is obtained by balancing the Lorentz force $qv_\perp B$ against the centrifugal force $mv_\perp^2/r$, resulting in

$$r_L = \frac{mv_\perp}{|q|B}. \tag{2.9}$$

The gyration frequency, or better yet the cyclotron frequency ω_c, is given by

$$\omega_c = \frac{|q|B}{m}. \tag{2.10}$$

The instantaneous center of rotation is called the guiding center, which moves along the constant uniform background magnetic field at a velocity $v_{\parallel}$.

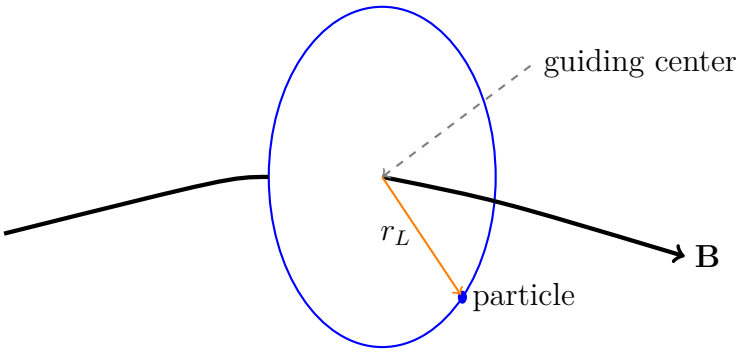

Figure 2.12: *Schematic representation of gyration along a magnetic field line. r_L denotes the gyration radius and* **B** *the background uniform magnetic field.*

In the case of a non-uniform magnetic field, the guiding center motion is also affected by curvature and gradient-drift. When the magnetic field strength **B** changes slowly along a direction perpendicular to the magnetic field direction, the curvature and/or transverse gradient of the magnetic field lines can lead to a drift motion. Given the radius of curvature R_c of a curved field line (see Figure 2.13), a particle moving along this field line at a speed $v_{\parallel}$ will be subject to a centrifugal force $F = mv_{\parallel}^2/R_c$, resulting in the curvature drift velocity

$$v_c = \frac{mv_{\parallel}^2}{qB^2}\mathbf{B} \times \nabla_{\parallel}\mathbf{b}, \tag{2.11}$$

where $\nabla_{\parallel}$ is the gradient along **B**, and $\nabla_{\parallel}\mathbf{b} = -\mathbf{R}_c/R_c^2 = \nabla_{\perp}B/B$ is a vector perpendicular to **B**. The symbol $\nabla_{\perp}$ denotes a component of the gradient in a direction perpendicular to **B**.

On the other hand, the gradient-drift arises from variations along the transverse gradient of the magnetic field strength. It is worth noting that particle orbits in regions of a strong magnetic field have a much smaller radius of curvature r_L as opposed to orbits in weak field regions. This leads to the so-called ∇B-drift, which acts perpendicular to both the magnetic field and it's gradient (see e.g., *Chen*, 1974; *Kallenrode*, 2004; *de Blank*, 2006) and is given as

$$v_{\nabla B} = \frac{mv_{\perp}^2}{2qB^3}\mathbf{B} \times \nabla_{\perp}B. \tag{2.12}$$

The total drift velocity due to both curvature and ∇B-drift is found by adding Equation (2.11) and Equation (2.12), resulting in

$$V_D = \left(mv_{\parallel}^2 + \frac{mv_{\perp}^2}{2}\right)\frac{\mathbf{B} \times \nabla_{\perp}B}{qB^3}. \tag{2.13}$$

Magnetic flux tubes, as shown in Figure 2.14, are defined as regions of space containing a magnetic field (*Parker*, 1979), characterized by an "enclosing" surface parallel to **B**, an almost cylindrical symmetry, and a zero divergence of the magnetic field. Therefore, the total magnetic flux within the

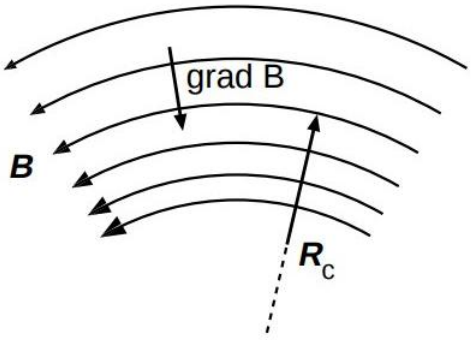

Figure 2.13: *Curvature radius and the field gradient, assuming a force-free* **B***-field. Figure adapted from de Blank (2006).*

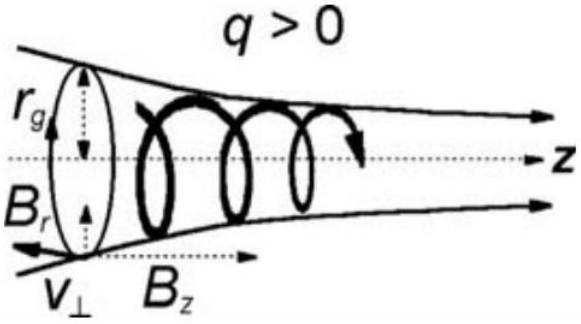

Figure 2.14: *Schematic of particle motion towards regions of increasing magnetic field. Figure adapted from Meyer-Vernet (2007).*

flux tube remains constant. In this case, the Lorentz force acts along the magnetic field assumed to be parallel to direction **z**, and is given as

$$F_z = |qv_\perp|B_r, \tag{2.14}$$

with $B_r < 0$ being some radial component. The particle experiences a deceleration in parallel velocity when moving towards regions of strong **B**, and an acceleration when moving towards a region of weaker **B**. The magnetic field's radial component at some distance r is given by

$$B_r = -\frac{r}{2}\frac{dB}{dz}. \tag{2.15}$$

Substitution of Equation (2.15) into Equation (2.14), and noting that $r = r_L$, results in

$$F_z = -ms\nabla_z B, \tag{2.16}$$

where ∇_z is the gradient component along $\mathbf{B}$, and s is the magnetic moment per unit particle mass, given as (*Meyer-Vernet*, 2007; *de Blank*, 2006)

$$s = \frac{v_\perp^2}{2B}. \tag{2.17}$$

2.5.1.1 Magnetic moment

The magnetic moment as given in Equation (2.17) is the product of some current $I = q\omega_c/2\pi$ and the area πr_L^2 enclosed by the current loop (*Meyer-Vernet*, 2007). Averaging over one gyro-orbit shows that the particle gyration can be approximated by a current loop of magnetic moment s, which is opposite to the magnetic field direction (see e.g., *Chen*, 1974; *Meyer-Vernet*, 2007).

Slow variations in the magnetic field result in an approximately constant magnetic moment (on both temporal and spatial scales) of a gyrating particle. The magnetic moment s is called an adiabatic invariant, which is said to be the case when a system varies slowly compared with the characteristic time of the periodic motion, and the action integral remains approximately constant (see e.g., *de Blank*, 2006; *Kallenrode*, 2004; *Meyer-Vernet*, 2007).

2.5.1.2 Magnetic mirrors

Particles are said to be mirrored when the particle's guiding center is moving towards regions of increasing magnetic field strength, i.e. converging field lines. The Lorentz force, having a gyro-averaged component acting opposite to $\nabla\mathbf{B}$, produces a mirroring force identical to the force on a magnetic dipole (Equation 2.16), given as

$$F_\parallel = -ms\nabla_\parallel B. \tag{2.18}$$

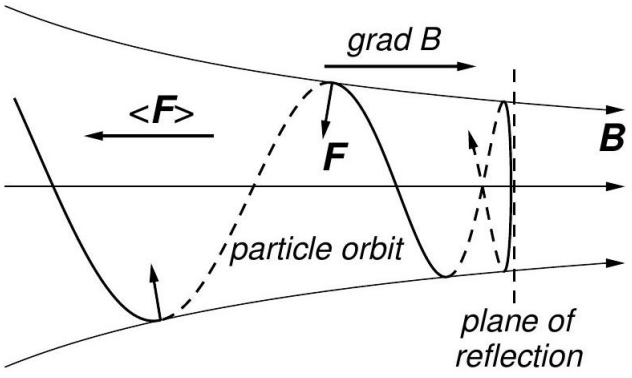

Figure 2.15: *Particle orbit in a magnetic mirror. Figure adapted from de Blank (2006).*

According to *de Blank* (2006), forces parallel to the magnetic field direction cause a parallel acceleration, given by

$$\frac{dv_{g,\parallel}}{dt} = \frac{F_{\parallel}}{m}. \tag{2.19}$$

Considering Equations (2.18) and (2.19), one can see that the mirroring force results in a parallel deceleration given by

$$\frac{dv_{g,\parallel}}{dt} = -s\nabla_{\parallel}B. \tag{2.20}$$

This force slows down the particle's parallel motion. Furthermore, the particle's perpendicular energy $mv^2 \sin^2 \alpha$ scales with $\mathbf{B}$, and by keeping s constant, the particle's velocity v also remains constant. The pitch-angle α on the other hand varies. Once it increases to approximately $\pi/2$ (the plane of reflection), the particle is reflected back to regions of weaker magnetic field (*Meyer-Vernet*, 2007), as shown in Figure 2.15.

2.6 Turbulence

2.6.1 Properties of Turbulence

The particle motions described in the previous section are crude approximations of charged particle transport. In reality, particle propagation in interplanetary space is also influenced by the turbulence associated with the magnetic field-lines embedded within the solar wind plasma. This section will briefly introduce turbulence, and the various models used to describe turbulent fluctuations, i.e. slab or (1D) turbulence, two-dimensional (2D) turbulence, a combination of the two called composite (two-component) turbulence (*Bieber et al.*, 1994), and the foot-point random motion model (see e.g., *Jokipii and Parker*, 1970; *Giacalone et al.*, 2006). The last two models are especially crucial in studies of energetic particle transport in space.

Turbulence is defined as the presence of random fluctuations in fluids which are irregular on both spatial and temporal scales (see e.g., *Antonia et al.*, 2017). Turbulence is quite often expressed as a summation of a uniform background magnetic field $\mathbf{B}_o$ and some fluctuating component $\delta\mathbf{b}$ (*Taylor*, 1938), i.e

$$\mathbf{B} = \mathbf{B}_o + \delta\mathbf{b}. \tag{2.21}$$

Fluctuations in the magnetic field have been observed by the Ulysses spacecraft and various other platforms (*Jokipii and Kota*, 1995; *Balogh et al.*, 1995). Observations hint at a Kolmogorov power-law relation (*Kolmogorov*, 1941) between the power of turbulent magnetic field, P_B and the spatial wave number κ (*Coleman*, 1968), i.e

$$P_B \propto \kappa^{-5/3}. \tag{2.22}$$

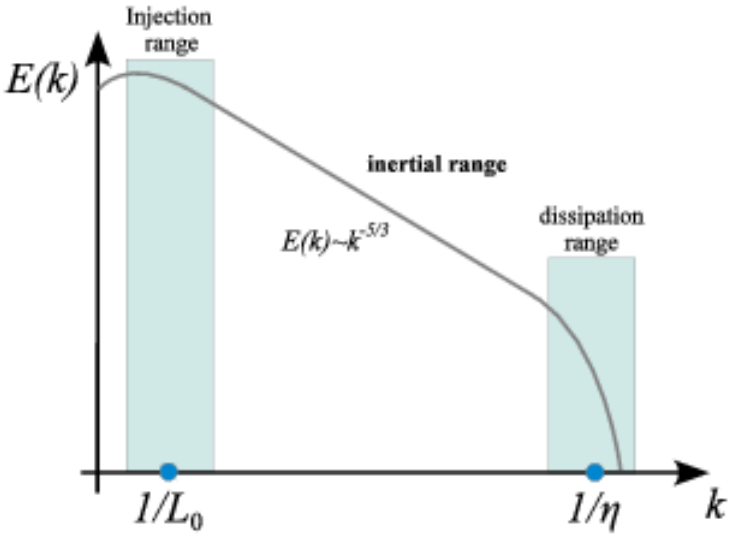

Figure 2.16: *Kolmogorov turbulence energy spectrum.* $1/L_o$ *and* $1/\eta$ *denote the length scale of the largest and smallest eddies respectively. Figure taken from Springel (2016).*

The power law spectrum can be interpreted as meaning that there is a transfer of energy at a constant rate in the fluctuations (*Erdős*, 2003), from the largest to the smallest eddies, through the so-called inertial range (as shown in Figure 2.16), with dissipation occurring at the smallest eddies. The injection range, shown at low wave numbers in Figure 2.16, highlights the region where energy is injected into the fluctuations k (*Bieber et al.*, 1994; *Teufel and Schlickeiser*, 2003). The correlation length, i.e. the scale of the eddies in the turbulent magnetic field corresponds to $\sim 10^6$ km at 1 AU, and subsequently increases with heliocentric distance (see e.g., *Bruno and Carbone*, 2013).

2.6.2 Models

2.6.2.1 Slab Turbulence

Slab turbulence is characterized by a fluctuating magnetic field, perpendicular to the mean field but only dependent on the coordinate z along the field (*Bieber et al.*, 1996). Irrespective of the relative positions in the (x, y) plane, flux tubes originating at the same position along the uniform magnetic field $\mathbf{B}_o$ remain identical as a result of the fluctuating component $\delta\mathbf{b}$ being strictly dependent only on z (*Matthaeus et al.*, 1995). The magnetic field arising as a result of these fluctuations is expressed as (see e.g., *Engelbrecht*, 2008)

$$\begin{aligned}\mathbf{B} &= B_o\mathbf{e}_z + \mathbf{b}_{slab}(z) \\ &= B_o\mathbf{e}_z + b_{slab,x}(z)\mathbf{e}_x + b_{slab,y}(z)\mathbf{e}_y,\end{aligned} \tag{2.23}$$

with the total variance given by

$$\delta B^2_{slab} = \delta b^2_{slab,x} + \delta b^2_{slab,y}. \tag{2.24}$$

For a turbulent flow that is axisymmetric with respect to the mean magnetic field direction $\hat{z}$, the x and y components are indistinguishable, and thus

$$\delta B^2_{slab} = 2\delta b^2_{slab,x} = 2\delta b^2_{slab,y}. \tag{2.25}$$

2.6.2.2 2D Turbulence

The fluctuations in a 2D turbulence model are assumed to be functions of the (x, y) coordinates, transverse to the mean magnetic field, and independent of the coordinate along the mean field z. The total magnetic field can then be expressed by

$$\begin{aligned} \mathbf{B} &= B_o \mathbf{e}_z + \mathbf{b}_{2D}(x, y) \\ &= B_o \mathbf{e}_z + b_{x,2D}(x, y)\mathbf{e}_x + b_{y,2D}(x, y)\mathbf{e}_y. \end{aligned} \tag{2.26}$$

The assumption of the 2D fluctuations being a function of coordinates perpendicular to the uniform background magnetic field leads to a "braiding" and "shredding" of the magnetic flux tubes (*Matthaeus et al.*, 2003), and as a result magnetic flux tubes starting at different (x, y) positions would not be identical, as in the slab turbulence case (*Engelbrecht*, 2008).

The variance of the 2D turbulence model is given by

$$\delta B^2_{2D} = \delta b^2_{2D,x} + \delta b^2_{2D,y}. \tag{2.27}$$

Furthermore, as is similarly shown for the slab turbulence model, the assumption of turbulence that is axisymmetric with respect to the uniform magnetic field direction leads to

$$\delta B^2_{2D} = 2\delta b^2_{2D,x} = 2\delta b^2_{2D,y}. \tag{2.28}$$

2.6.2.3 Composite Turbulence

The composite (two-component) model, often used in studying the transport of energetic particles in space, is largely based on observations pertaining to the turbulent solar wind (*Matthaeus et al.*, 1990). The composite model is expressed as a sum of the slab and 2D turbulence models (see e.g., *Engelbrecht*, 2008), i.e.

$$\mathbf{b} = \mathbf{b}_{slab}(z) + \mathbf{b}_{2D}(x, y). \tag{2.29}$$

Observations of the solar wind further hint that the inertial range of the composite turbulence model is dominated by $\sim 70\% - 90\%$ of 2D turbulence, with the remainder being attributed to slab turbulence (*Matthaeus et al.*, 1990; *Bieber et al.*, 1996). The total variance associated with the composite model is given by *Matthaeus et al.* (1995) as

$$\delta B^2 = \delta B^2_{slab} + \delta B^2_{2D}. \tag{2.30}$$

For an axisymmetric composite turbulence model,

$$\delta B^2 = 2\delta B_{slab,x}(z)^2 + 2\delta B_{2D,x}(x,y)^2. \tag{2.31}$$

2.6.2.4 Foot-point random motion turbulence

A foot-point random motion turbulence model came about from suggestions by *Jokipii and Parker* (1970) and *Giacalone et al.* (2006). The authors suggested that magnetic fluctuations can be generated by random motions of HMF foot-points. The assumptions of this model involve a uniform background magnetic field B_o, along $\hat{z}$, with a source surface situated in the (x, y) plane at $z = 0$. The fluctuating component δb_{fp} of the foot-point random motion is given by

$$\delta \mathbf{b}_{fp} = \frac{B_o}{U}\mathbf{v}_{fp}(x, y, t - z/U), \tag{2.32}$$

where U is the solar wind convective speed, and $\mathbf{v}_{fp}(x, y, t)$ describes the surface foot-point motion on the source surface, with respect to an arbitrary streaming function ψ, and is given as

$$\mathbf{v}_{fp}(x, y, t) = \nabla \times \psi(x, y, t). \tag{2.33}$$

The composite and foot-point models are crucial in describing the transport of energetic particles in turbulent magnetic fields. It is, however, worth noting that non-linear structures present in the magnetic turbulence such as small scale current sheets, which quite possibly play a significant role in particle transport, are not included and as such these models do not necessarily give the overall picture of turbulence in the solar wind.

2.7 Solar Energetic Particles

Solar energetic particles (SEPs), also called "solar cosmic rays", were initially detected by neutron monitors (*Simpson*, 1957) in the 1940s as ground level enhancements (GLEs ; *Forbush* 1946). A correlation between the GLEs, as observed by the then large neutron monitor network with the largest solar flares and with what are now known to be CMEs (*Tousey*, 1973; *MacQueen et al.*, 1974) confirmed the Sun as the source of these charged particles. SEPs pose a real danger to astronauts in space, can lead to a degradation of precious satellites and other Earth infrastructure, and even closer to home, they can result in a radiation hazard for airline passengers.

The Earth's magnetosphere provides a relatively "safe zone" against SEPs, reducing the influx of potentially harmful SEPs for near-Earth objects (see e.g., *Moldwin*, 2008; *Dorman and Pustil'Nik*, 2008). For spacecraft outside this "safe zone", such as those transferring from Earth to Mars orbit, SEPs pose an even greater threat. The study (observations and numerical simulations) of SEPs is thus crucial when it comes to interplanetary travel and becomes even more important, when one considers

the current NASA and SpaceX aspirations of founding a Mars research base, and eventual colony, given the rather significantly weaker SEP shielding at Mars (see e.g., *Hassler et al.*, 2014).

2.7.1 Observations

Observations of SEPs are in most cases carried out by measuring particle fluxes in various energy ranges (see e.g., *Torsti et al.*, 1995; *Dresing et al.*, 2014).

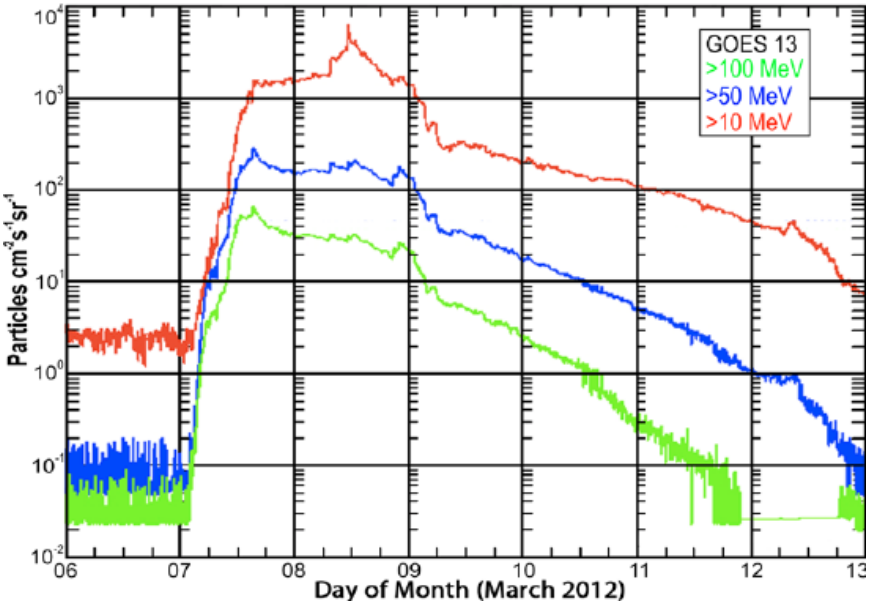

Figure 2.17: *Solar energetic particle event proton fluxes as seen by GOES for various energy ranges. Figure taken from Hassler et al. (2012).*

The detection of these particles is due to the ever increasing array of observation spacecraft within the Sun-Earth-Mars environment, examples of which include the Solar and Heliospheric Observatory (SOHO), the Advanced Composition Explorer (ACE), and Wind. These are located at the Lagrange point L1, a point in space where the gravitational forces of the Sun and Earth balance out. The Solar Dynamics Observatory (SDO) is in geosynchronous orbit around the Earth, with the twin Solar Terrestrial Relations Observatory (STEREO) spacecraft following Earth's orbit around the Sun, with STEREO A ahead of Earth, and STEREO B following behind Earth. Other notable spacecraft missions include the Payload for Antimatter Matter Exploration and Light-nuclei Astrophysics (PAMELA), which can detect particles with energies in the GeV and TeV range, the much-anticipated Parker Solar Probe (PSP), and Solar Orbiter missions. The near Mars environment is monitored by the Mars Atmosphere and Volatile EvolutioN (MAVEN) mission (*Larson et al.*, 2015). It is, however, worth noting that there is limited observational data taken at Mars. Figure 2.17 shows SEP proton fluxes as seen by the Geostationary Operational Environmental Satellite (GOES) from March 7, 2012 for varying energy ranges as a function of time (*Hassler et al.*, 2012).

2.7.2 Sources of Solar Energetic Particles

The acceleration of solar energetic particles is mainly due to two physical mechanisms. These mechanisms have been confirmed by observations of type III bursts (associated with selective heating of outward streaming electrons and magnetic reconnection) and type II bursts, which are associated with CMEs and subsequent shock waves. The mechanisms described above respectively result in *impulsive* and *gradual* events (*Reames*, 2013), as illustrated in Figure 2.18.

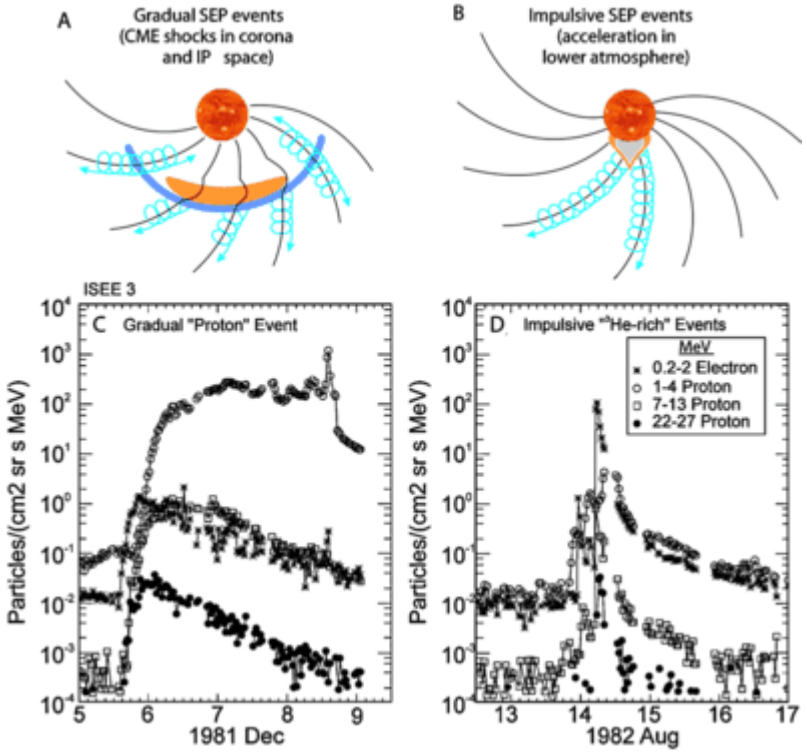

Figure 2.18: *Sources of SEP events.* ***(A)*** *An illustration of a gradual proton event produced by an expanding CME-driven shock wave.* ***(B)*** *An illustration of an impulsive solar flare event, and particle streaming along well-connected interplanetary magnetic field (IMF) lines. The intensity-time profiles of electrons and protons in a large gradual event and a small impulsive event, are respectively shown in panels* ***(C)*** *and* ***(D)****. Figure taken from McComas et al. (2016).*

2.7.2.1 Impulsive events

Impulsive events occur on time-scales ranging from several minutes to hours. They are related to solar flares, with the particles presumably accelerated via magnetic reconnection (see e.g., *Reames*, 2013; *Kallenrode*, 2004). They are characterized by high charge states of Fe and Si, as well as an enrichment of heavier ions, particularly ^{3}He/^{4}He (see e.g., *Reames*, 1988), Fe/C and Fe/O relative to the background plasma properties.

2.7.2.2 Gradual events

In contrast to impulsive events, gradual events can occur on time-scales of hours to several days. Gradual events are associated with coronal mass ejections (CMEs). As the CMEs propagate outwards they form a shock, and with increasing time this shock slows down and weakens. Therefore shocks, as seen in Figure 2.18 (panel **A**), are only efficient at particle acceleration within ∼20 solar radii (*McComas et al.*, 2016). The shock accelerates the particles by means of diffusive shock acceleration (*Vainio*, 1999). The overall composition of particles originating from these events is similar to solar wind abundances. Additionaly, shocks gradually accelerate protons to high energies, whereas electrons easily escape the shock region due to their lower mass. Behind the shock is the so-called 'reservoir', which according to *Reames* (2013) is "a spatially extensive trapped volume of uniform SEP intensities with invariant energy-spectral shapes where overall intensities decrease with time as the closing 'magnetic bottle' expands adiabatically". The intensity decrease, as shown in Figure 2.18 (panel **C**), can be in part attributed to these reservoirs.

It is worth noting that, regardless of the acceleration mechanisms, SEP events contain particles from both flare and shock acceleration (see e.g., *Kallenrode*, 2003). This reality makes the interpretation of spacecraft data quite difficult in terms of the sources and acceleration mechanisms responsible for observed SEP events (*Lampa*, 2011). The upcoming NASA Parker Solar Probe mission is expected to provide deeper insight into the acceleration of energetic particles, through its Integrated Science Investigation of the Sun (ISIS) instrument (*McComas et al.*, 2016).

2.7.3 Solar Energetic Particle Transport

The propagation of SEPs in the inner heliosphere is influenced by a variety of physical processes. These processes, in combination, result in changes in SEP intensities at various heliocentric distances and are described by the one-dimensional (1D) transport equation, given by *Ruffolo* (1995) for a local solar wind frame, and given by

$$
\begin{aligned}
\frac{\partial f(t,\mu,z,p)}{\partial t} &= -\frac{\partial}{\partial z}\mu v f(t,\mu,z,p) \\
&- \frac{\partial}{\partial z}\left(1-\mu^2\frac{v^2}{c^2}\right) v_{sw}\sec(\psi) f(t,\mu,z,p) \\
&- \frac{\partial}{\partial \mu}\frac{v}{2L(z)}\left[1+\mu\frac{v_{sw}}{v}\sec(\psi)-\mu\frac{v_{sw}v}{c^2}\sec(\psi)\right](1-\mu^2) f(t,\mu,z,p) \\
&+ \frac{\partial}{\partial \mu} v_{sw}\left(\cos(\psi)\frac{d}{dr}\sec(\psi)\right)\mu(1-\mu^2) f(t,\mu,z,p) \\
&+ \frac{\partial}{\partial \mu}\frac{D_{\mu\mu}(\mu)}{2}\frac{\partial}{\partial \mu}\left(1-\mu\frac{v_{sw}v}{c^2}\sec(\psi)\right) f(t,\mu,z,p) \\
&+ \frac{\partial}{\partial p} p v_{sw}\left[\frac{\sec(\psi)}{2L(z)}(1-\mu^2)+\cos(\psi)\frac{d}{dr}\sec(\psi)\mu^2\right] f(t,\mu,z,p)
\end{aligned}
\tag{2.34}
$$

where the particle distribution function is given by

$$f(t,\mu,z,p) = \frac{d^3N}{dzd\mu dp}. \tag{2.35}$$

This distribution function is dependent on time t, distance z along the field line, the cosine of the pitch-angle μ, the momentum of the particle p, the spiral angle ψ, the focusing length L, and the number of particles N within a given flux tube (*Ng and Wong*, 1979). The various terms in Equation (2.34) describe the streaming, convection, focusing, differential convection, scattering, and deceleration of particles (for a review see, *Ruffolo*, 1995).

In this study, it is assumed that the SEPs are energetic enough so that $v_{sw} \ll v$, making it possible to set $v_{sw} = 0$ in Equation (2.34). This results in the transport equation described by *Roelof* (1969)

$$\frac{\partial f(z,\mu,t)}{\partial t} = -\frac{\partial}{\partial z}(\mu v f) - \frac{\partial}{\partial \mu}\left(\frac{1-\mu^2}{2L} v f\right) + \frac{\partial}{\partial \mu}\left(D_{\mu\mu}(z,\mu)\frac{\partial f}{\partial \mu}\right), \tag{2.36}$$

where the particle velocity parallel to the HMF is given by $v_{\parallel}{=}\mu v$, with v being the particle speed. The streaming direction is determined by the unit vector $\hat{b}$, which is directed along the mean field. For simplicity it is assumed that the mean field is directed along the z-direction, i.e. $\hat{b} = \hat{z}$.

2.7.3.1 SEP streaming along mean HMF

In general, the term describing particle motion along the mean HMF is given by

$$\frac{\partial f}{\partial t} = -\nabla\cdot(\mu v \hat{b} f). \tag{2.37}$$

In spherical coordinates $\hat{b}$ can be written as

$$\hat{b} = \cos\psi \hat{r} - \sin\psi \hat{\phi}, \tag{2.38}$$

with ψ being the Parker spiral angle (*Parker*, 1958) discussed earlier. If $\mathbf{B} = B\hat{z}$, Equation (2.37) reduces to

$$\frac{\partial f}{\partial t} = -\frac{\partial}{\partial z}(\mu v f). \tag{2.39}$$

2.7.3.2 Focusing

In a locally diverging magnetic field line, the magnetic field strength decreases which in turn leads to a decrease in the particle gyration energy. The helical orbits of particles streaming along the magnetic flux tube become increasingly field-aligned with increasing heliocentric distance. This results in the pitch-angle α tending towards zero, which results in the cosine of the pitch-angle tending towards unity.

The temporal change of μ can be derived in several ways in order to obtain the second term in Equation (2.36). This section shall follow a derivation presented by *Lampa* (2011), in which the focusing term is defined as

$$\frac{\partial f}{\partial t} = \frac{\partial \mu}{\partial t}\frac{\partial f}{\partial \mu}. \tag{2.40}$$

Utilizing the chain rule, the temporal change of the pitch-angle is found to be

$$\frac{\partial \mu}{\partial t} = \frac{\partial \mu}{\partial B}\frac{\partial B}{\partial z}\frac{\partial z}{\partial t}. \tag{2.41}$$

Charged particles moving in magnetic fields of increasing strength experience a decrease in $v_\perp$ and a subsequent reversal of their direction of motion at the so-called "magnetic mirror". This point occurs when (*Lampa*, 2011)

$$\mu = \sqrt{1 - \frac{B}{B_z}}, \tag{2.42}$$

with B and B_z being some magnetic field strengths at two arbitrarily chosen points. Taking the derivative of Equation (2.42) with respect to the magnetic field B, yields

$$\frac{\partial \mu}{\partial B} = -\frac{1}{2}\left(1 - \frac{B}{B_z}\right)^{-1/2} \cdot \frac{1}{B_z}. \tag{2.43}$$

Solving for B_z in Equation (2.42), and substituting it into Equation (2.43), yields

$$\frac{\partial \mu}{\partial B} = \frac{1}{2\mu}\frac{(1-\mu^2)}{B}. \tag{2.44}$$

From the further substitution of Equation (2.44) into Equation (2.41), and noting that $\partial z/\partial t = v_\parallel = \mu v$, it follows that

$$\frac{\partial \mu}{\partial t} = -\frac{1}{2\mu}\frac{(1-\mu^2)}{B}\frac{\partial B}{\partial z}\mu v = -\frac{(1-\mu^2)}{2L(z)}v, \tag{2.45}$$

where $L(z) = B(z)/(\partial B(z)/\partial z)$ describes the focusing length. Final substitution of Equation (2.45) into Equation (2.40) then yields the focusing term as

$$\frac{\partial f}{\partial t} = -\frac{1-\mu^2}{2L(z)}v\frac{\partial f}{\partial \mu}. \tag{2.46}$$

This term gives insight into particle transport along a magnetic flux tube.

2.7.3.3 Pitch-angle scattering

Alfvén waves propagating parallel to the IMF (as in the slab turbulence model) cause fluctuations in the magnetic field and current density. Wave-particle interactions occur when particle gyration along the magnetic field is in resonance with the field fluctuation's wavelength (*Jokipii*, 1966). These waves are said to scatter/diffuse SEPs in interplanetary space (*Roelof*, 1969). The fourth term in Equation (2.36) describes the small deviations in the particle's trajectory in terms of scattering in pitch-cosine

space, and is given as

$$\frac{\partial}{\partial \mu}\left(D_{\mu\mu}(z,\mu)\frac{\partial f}{\partial \mu}\right), \tag{2.47}$$

where $D_{\mu\mu}$ is the pitch-angle diffusion coefficient (PADC), which describes the pitch-angle scattering of the particle. The quantity $D_{\mu\mu}$ is related to the field parallel mean free path by (*Hasselmann and Wibberenz*, 1968)

$$\lambda_{\parallel}(r,\mu) = \frac{3v}{8}\int_{-1}^{+1}\frac{(1-\mu^2)^2}{D_{\mu\mu}(r,\mu)}d\mu, \tag{2.48}$$

with v being the particle speed, and r the heliocentric distance. The form of the PADC can be described using quasi-linear theory (QLT ; *Jokipii* 1966). In this study, the PADC is taken to be of the form (see e.g., *Dröge et al.*, 2010; *Strauss and Fichtner*, 2015)

$$D_{\mu\mu}(r,\mu) = D_{\mu\mu,0}(r,\mu)(1-\mu^2)\left\{|\mu|^{q-1}+H\right\}, \tag{2.49}$$

where $D_{\mu\mu,0}$ describes the fluctuations in the magnetic field, and q is the spectral index of the inertial Kolmogorov range on the turbulence power spectrum. When $q = 1$, diffusion of SEPs is uniform, whereas increasing values of q result in the so-called resonance gap around $\mu = 0$. The parameter H is used to simulate non-linear corrections. For even larger values of q, i.e. $q \geq 2$, there is a decoupling, meaning that particles are no longer able to reverse direction (*Lampa*, 2011).

2.7.3.4 Perpendicular Transport

The perpendicular transport of SEPs results in the diffusive transport of particles in a direction perpendicular to the mean background magnetic field. Early observations of the previously discussed "reservoirs" within the inner heliosphere (see e.g., *McKibben et al.*, 2003), and the more recent wider than expected longitudinal extent of SEPs (see, e.g., *Dresing et al.*, 2012) hint at some sort of process responsible for SEP transport perpendicular to the mean magnetic field.

The importance of perpendicular diffusion in SEP transport, with emphasis on the longitudinal extent of events has become evident in recent numerical models (see, e.g., *Zhang et al.*, 2009; *He et al.*, 2011; *Laitinen et al.*, 2013; *Dröge et al.*, 2014; *Strauss and Fichtner*, 2015; *Strauss et al.*, 2017), with observations by various spacecraft confirming this (see, e.g., *Zhang et al.*, 2003; *He and Wan*, 2012; *Dresing et al.*, 2012, 2014). In this study, however, the perpendicular transport of SEPs is not considered.

2.7.4 Observable Quantities

In this study, model solutions will be obtained in terms of various directly observable quantities such as differential and omni-directional intensities and particle anisotropies. This section will focus on the mathematical expressions used to define the abovementioned quantities.

Differential Intensity

The differential intensity describes the number of particles in an energy interval $[E, E + dE]$, passing through a location $\mathbf{x}$ of area $d\mathbf{A}$, from direction $\mathbf{n}$ and surrounded by a solid angle $d\mathbf{\Omega}$, in a time interval $[t, t + dt]$ (*Kallenrode*, 2004). This is given by

$$I(\mathbf{x}, E, \mathbf{n}, t)dE.d\mathbf{\Omega}.d\mathbf{A}.dt, \tag{2.50}$$

where $I(\mathbf{x}, E, \mathbf{n}, t)$ denotes some particle distribution.

Omni-directional Intensity

The quantity most often measured by spacecraft is the omnidirectional intensity, obtained by averaging over all possible directions $\mathbf{n}$. This results in

$$I_{\text{omni}}(\mathbf{x}, E, t) = \frac{\iint I(\mathbf{x}, E, \mathbf{n}, t)\, d\mathbf{\Omega}}{\iint d\mathbf{\Omega}} = \frac{1}{4\pi} \iint I(\mathbf{x}, E, \mathbf{n}, t)\, d\mathbf{\Omega}. \tag{2.51}$$

For the case of an isotropic angular distribution, the omni-directional intensity is comparable to the differential intensity (*Lampa*, 2011). The unit of omni-directional intensity most commonly used is $\text{cm}^{-2}\cdot\text{sr}^{-1}\cdot\text{s}^{-1}\cdot\text{MeV}^{-1}$.

Anisotropy

The particle anisotropy gives a measure of particle flux direction with respect to the background magnetic field. Assuming a gyrotropic particle distribution, this is given by

$$\mathbf{A}(\mathbf{x}, E, t) = 3\frac{\int_{-1}^{+1} I(\mathbf{x}, E, \mu, t)\mu d\mu}{\int_{-1}^{+1} I(\mathbf{x}, E, \mu, t)d\mu}, \tag{2.52}$$

with $I(\mathbf{x}, E, \mu, t)$ representing some pitch angle distribution. An anisotropy value of 3 means that all the particles are moving forward, i.e. along the magnetic field, whereas $\mathbf{A}(\mathbf{x}, E, t) = -3$ would imply the reverse. A zero value implies an equal amount of particles moving forward and backwards, implying an isotropic particle distribution.

2.8 Summary

This chapter serves to provide some background and context for the present study. Solar activity and the solar wind are discussed. The solar wind, with the magnetic field embedded in it to form the HMF, is responsible for changes in SEP intensities within the inner heliosphere. The form of the HMF

assumed in this study is the Parker spiral (*Parker*, 1958). The spiral field lines act as a "highway" for SEPs originating from solar flares and/or CMEs. These SEPs are occasionally observed by spacecraft at various positions within the inner heliosphere. The form of the *Roelof* (1969) equation, as given in Equation (2.36), will be used in the following chapters to model the propagation of SEPs to heliocentric distances somewhat beyond Mars' orbit.

CHAPTER 3

An Introduction to Finite-Difference Methods

3.1 Introduction

In this chapter an introduction to finite-difference (FD) methods and the classification of partial differential equations (PDEs) will be given. This will be used to identify the respective parts of the *Roelof* (1969) equation in a later chapter. Methods used to numerically solve diffusion and advection equations, including the Lax-Wendroff (*Lax and Wendroff*, 1960) and the Forward-Upwind schemes (*Lapidus and Pinder*, 1982), are discussed. The chapter concludes by looking at "random" numerical oscillations and their suppression in numerical methods using so-called flux limiters.

3.2 Finite Difference Methods

Most of the phenomena in fields as varied as space science, meteorology, and civil engineering are governed by complex PDEs, which in most cases have no analytical solutions. In these cases, numerical methods such as the FD schemes have become invaluable tools in providing solutions to real-life problems. This has provided insight into physically or geometrically complex problems.

Finite difference methods involve approximating the derivatives in an equation by differential quotients. Space and time domains are partitioned into grids with definite boundaries and the solutions are calculated at these space or time points, usually by means of a Taylor series expansion. The discrete approximations resulting from the expansion are called finite-difference formulae.

3.2.1 Deriving Finite Difference Formulae

Given the scales and regions involved in SEP propagation, the Roelof equation's numerical solution may behave differently in certain regions. A fine mesh would be much more suitable to rapid changes in the solution, keeping the code stable, whereas for regions with little or no change in the solution a fine mesh would be computationally expensive and thus wasteful (*Steenkamp*, 1995). To resolve this predicament, a technique used by *Steenkamp* (1995) is considered in which the well known finite-difference formulae are derived for an uneven numerical grid.

Consider the following 1D uneven grid:

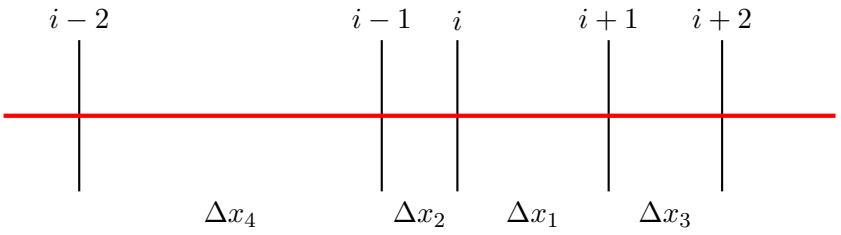

The solutions of the function f at the different grid points are denoted by

$$f_{i-2} = f(x - \Delta x_2 - \Delta x_4), \tag{3.1}$$

$$f_{i-1} = f(x - \Delta x_2), \tag{3.2}$$

$$f_i = f(x), \tag{3.3}$$

$$f_{i+1} = f(x + \Delta x_1), \tag{3.4}$$

and

$$f_{i+2} = f(x + \Delta x_1 + \Delta x_3). \tag{3.5}$$

Consider a Taylor series expansion of f about a small interval called the *smallness parameter* Δx

$$f(x \pm \Delta x) = f(x) \pm \Delta x f' + \frac{(\Delta x)^2}{2} f'' \pm ..., \tag{3.6}$$

where f' and f'' are respectively the first and second order derivatives $\partial f/\partial x$ and $\partial^2 f/\partial x^2$.

The discretization error after n terms is given by

$$\sum_{i=n}^{\infty} \frac{(\Delta x)^i}{i!} f^{(i)}, \tag{3.7}$$

with $f^{(i)}$ being the i-th derivative with respect to the spatial position x (*Steenkamp*, 1995). The discretization or truncation error reflects the fact that only a finite part of the Taylor series is used in the approximation. From the substitution of Equation (3.6) into the right hand side of Equations (3.4) and (3.2), it follows that

$$f_{i+1} \simeq f(x) + \Delta x_1 f' + \frac{(\Delta x_1)^2}{2} f'' + ... \tag{3.8}$$

and

$$f_{i-1} \simeq f(x) - \Delta x_2 f' + \frac{(\Delta x_2)^2}{2} f'' + ... \tag{3.9}$$

Truncating the series after two terms and using Equation (3.3), Equations (3.8) and (3.9) yield

$$f_{i+1} \simeq f_i + \Delta x_1 f', \tag{3.10}$$

and

$$f_{i-1} \simeq f_i - \Delta x_2 f'. \tag{3.11}$$

The first order one-sided derivatives can be obtained by solving for f' in both Equations (3.10) and (3.11) so that

$$f' = \frac{f_{i+1} - f_i}{\Delta x_1}, \tag{3.12}$$

and

$$f' = \frac{f_i - f_{i-1}}{\Delta x_2}, \tag{3.13}$$

which are the well known forward difference and backward difference formulas, and are correct to first order in Δx, denoted by $\mathcal{O}(\Delta x)$.

The second order truncations can be found from Equations (3.1), (3.2), (3.4), and (3.5) in the same way as Equations (3.10) and (3.11):

$$f_{i+1} \simeq f_i + (\Delta x_1) f' + \frac{(\Delta x_1)^2}{2} f'' + \mathcal{O}[(\Delta x_1^3)], \tag{3.14}$$

$$f_{i+2} \simeq f_i + (\Delta x_1 + \Delta x_3) f' + \frac{(\Delta x_1 + \Delta x_3)^2}{2} f'' + \mathcal{O}[(\Delta x_1 + \Delta x_3)^3], \tag{3.15}$$

$$f_{i-1} \simeq f_i - (\Delta x_2) f' + \frac{(\Delta x_2)^2}{2} f'' + \mathcal{O}[(\Delta x_2)^3], \tag{3.16}$$

and

$$f_{i-2} \simeq f_i - (\Delta x_2 + \Delta x_4) f' + \frac{(\Delta x_2 + \Delta x_4)^2}{2} f'' + \mathcal{O}[(\Delta x_2 + \Delta x_4)^3], \tag{3.17}$$

which are all correct to second order, $\mathcal{O}[(\Delta x)^2]$.

To obtain the first central derivative formula, the following expression is used

$$(\text{Eq}\cdot 3.14) \times (\Delta x_2)^2 - (\text{Eq}\cdot 3.16) \times (\Delta x_1)^2, \tag{3.18}$$

which leads to

$$(\Delta x_2)^2 f_{i+1} - (\Delta x_1)^2 f_{i-1} = [(\Delta x_2 - \Delta x_1) - (\Delta x_2 + \Delta x_1)] f_i + \Delta x_1 \Delta x_2 [\Delta x_2 + \Delta x_1] f'. \tag{3.19}$$

Now solving Equation (3.19) for f' leads to

$$f' = \frac{-\Delta x_1}{\Delta x_2(\Delta x_1 + \Delta x_2)} f_{i-1} + \frac{\Delta x_1 - \Delta x_2}{\Delta x_1 \Delta x_2} f_i + \frac{\Delta x_2}{\Delta x_1(\Delta x_1 + \Delta x_2)} f_{i+1}. \tag{3.20}$$

The second central derivative formula is obtained in a similar fashion, by using (Eq·3.14) $\times \Delta x_2 +$ (Eq·3.16) $\times \Delta x_1$, to yield

$$f'' = \frac{2}{\Delta x_2(\Delta x_1 + \Delta x_2)} f_{i-1} - \frac{2}{\Delta x_1 \Delta x_2} f_i + \frac{2}{\Delta x_1(\Delta x_1 + \Delta x_2)} f_{i+1}. \tag{3.21}$$

To obtain the second order one-sided differences, the following expression is utilized

$$(\text{Eq}\cdot 3.16) \times (\Delta x_2 + \Delta x_4)^2 - (\text{Eq}\cdot 3.17) \times (\Delta x_2)^2, \tag{3.22}$$

which leads to

$$(\Delta x_2 + \Delta x_4)^2 f_{i-1} - (\Delta x_2)^2 f_{i-2} = \Delta x_4 [2\Delta x_2 + \Delta x_4] f_i - \Delta x_2 \Delta x_4 (\Delta x_2 + \Delta x_4) f'. \tag{3.23}$$

Solving Equation (3.23) for f' results in

$$f' = \frac{2\Delta x_2 + \Delta x_4}{\Delta x_2(\Delta x_2 + \Delta x_4)} f_i - \frac{\Delta x_2 + \Delta x_4}{\Delta x_2 \Delta x_4} f_{i-1} + \frac{\Delta x_2}{\Delta x_4(\Delta x_2 + \Delta x_4)} f_{i-2}. \tag{3.24}$$

The second-order one-sided difference is obtained in a similar fashion, by (Eq·3.14) $\times (\Delta x_1 + \Delta x_3)^2 -$ (Eq·3.15) $\times (\Delta x_1)^2$, such that

$$f' = \frac{-(2\Delta x_1 + \Delta x_3)}{\Delta x_1(\Delta x_1 + \Delta x_3)} f_i + \frac{\Delta x_1 + \Delta x_3}{\Delta x_1 \Delta x_3} f_{i+1} + \frac{\Delta x_1}{\Delta x_3(\Delta x_1 + \Delta x_3)} f_{i+2}. \tag{3.25}$$

The method described above allows the finite-difference formulae to be expressed in terms of an even grid mesh, by setting $\Delta x_1 = \Delta x_2 = \Delta x_3 = \Delta x_4 = \Delta x$. From Equations (3.10) and (3.11), the well-known first-order accurate one-sided difference formulae are obtained as

$$f' = \frac{f_{i+1} - f_i}{\Delta x}, \tag{3.26}$$

and

$$f' = \frac{f_i - f_{i-1}}{\Delta x}. \tag{3.27}$$

The second-order accurate central difference formulae result from Equations (3.20), (3.21), (3.24), and (3.25)

$$f' = \frac{f_{i+1} - f_{i-1}}{2\Delta x}, \tag{3.28}$$

$$f'' = \frac{f_{i-1} - 2f_i + f_{i+1}}{\Delta x^2}, \tag{3.29}$$

$$f' = \frac{3f_i - 4f_{i-1} + f_{i-2}}{2\Delta x}, \tag{3.30}$$

and

$$f' = \frac{-3f_i + 4f_{i+1} + f_{i+2}}{2\Delta x}. \tag{3.31}$$

As discussed earlier there are many ways in which PDEs can be discretized, with varying accuracy. As

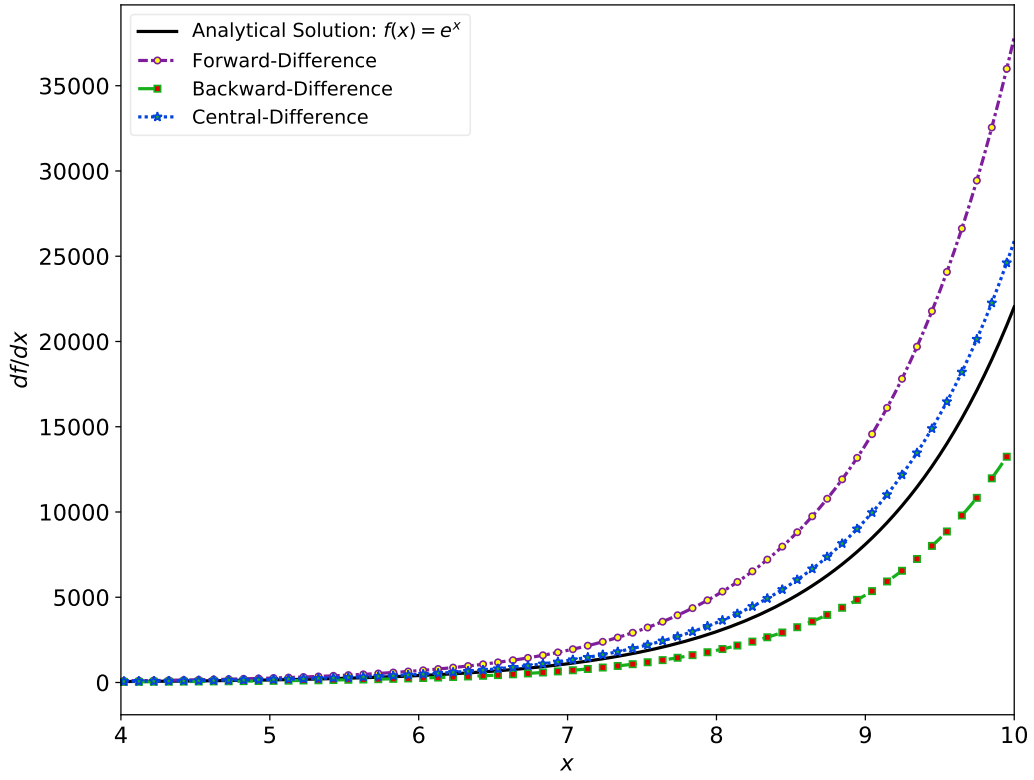

Figure 3.1: *Illustration of the accuracy of different finite-difference formulae. See the text for details.*

an example consider the function $f(x) = e^x$. Using the discretizations discussed above, the derivative is calculated and shown in Figure 3.1. It is clear from Figure 3.1 that the forward difference formula overestimate the solution, whereas the backward difference formula underestimate the solution. The central difference formula provides a compromise, falling "roughly" half-way between the other two. This makes sense, as the first two scenarios are only first order accurate, whereas the last is accurate to second order in Δx.

3.3 Second-Order Partial Differential Equations

3.3.1 Classifying Second-order PDEs

The first step in numerical modelling should always be to identify whether the PDE is elliptic, parabolic or hyperbolic. This identification provides insight into whether discontinuities exist or not, so as to accommodate for them in the numerical method. Also, different numerical schemes are only valid for different classes of PDEs. Consider the general second-order PDE

$$A\frac{\partial^2 f}{\partial x^2} + B\frac{\partial^2 f}{\partial x \partial y} + C\frac{\partial^2 f}{\partial y^2} + D\frac{\partial f}{\partial x} + E\frac{\partial f}{\partial y} + Ff + G = 0, \tag{3.32}$$

where A, B, C, D, E, F and the free term G are in general functions of the independent variables x, y and do not depend on the unknown function f (*Grigoryan*, 2010). Equation (3.32) can also be expressed in the following manner

$$Af_{xx} + Bf_{xy} + Cf_{yy} + Df_x + Ef_y + Ff + G = 0. \tag{3.33}$$

This is a second-order equation, and as such the coefficients of the second-order terms are expected to dominate, allowing the lower terms to be set equal to a function H,

$$A\frac{\partial^2 f}{\partial x^2} + B\frac{\partial^2 f}{\partial x \partial y} + C\frac{\partial^2 f}{\partial y^2} = -H(x, y, f, f_x, f_y), \tag{3.34}$$

where $H = -(D\frac{\partial f}{\partial x} + E\frac{\partial f}{\partial y} + Ff + G)$.

In general the highest order terms can be continuous/discontinuous across certain lines, called characteristic lines, which are defined as lines along which the solution is constant (*Scott*, 2003). From Equation (3.34) it follows that

$$f_x = f(x, y) \implies df_x = \frac{\partial f_x}{\partial x}dx + \frac{\partial f_x}{\partial y}dy = f_{xx}dx + f_{xy}dy, \tag{3.35}$$

and

$$f_y = f(x, y) \implies df_y = \frac{\partial f_y}{\partial x}dx + \frac{\partial f_y}{\partial y}dy = f_{yx}dx + f_{yy}dy. \tag{3.36}$$

Casting Equations (3.34), (3.35), and (3.36) in matrix form results in

$$\begin{bmatrix} A & B & C \\ dx & dy & 0 \\ 0 & dx & dy \end{bmatrix} \begin{bmatrix} f_{xx} \\ f_{xy} \\ f_{yy} \end{bmatrix} = \begin{bmatrix} -H \\ -df_x \\ df_y \end{bmatrix}. \tag{3.37}$$

These characteristic lines exist were the determinant is zero. In order for f_{xx}, f_{xy}, and f_{yy} to be discontinuous, which would imply a characteristic line, the determinant has to be zero (*Scott*, 2003)

$$\begin{bmatrix} A & B & C \\ dx & dy & 0 \\ 0 & dx & dy \end{bmatrix} = 0, \tag{3.38}$$

resulting in a quadratic function

$$A\left(\frac{dy}{dx}\right)^2 - B\left(\frac{dy}{dx}\right) + C = 0, \tag{3.39}$$

which has a solution

$$\frac{dy}{dx} = \frac{B \pm \sqrt{B^2 - 4AC}}{2A}. \tag{3.40}$$

Depending on the sign of the discriminant $d = \sqrt{B^2 - 4AC}$, PDEs are classified into three types, namely

- Parabolic PDEs, if $d = \sqrt{B^2 - 4AC} = 0$: This would mean that one real characteristic exists.
- Hyperbolic PDEs, if $d = \sqrt{B^2 - 4AC} > 0$: This means two real characteristics exist.
- Elliptic PDEs, if $d = \sqrt{B^2 - 4AC} < 0$: This type implies no real characteristics exist.

Parabolic PDEs describe initial value boundary problems (*Hoffman and Frankel*, 2001), in the sense that the propagation of the perturbation in the domain depends on the initial conditions at $t = t_0$. For parabolic PDEs, the velocity at which the perturbation propagates is infinite and time dependent (*Brio et al.*, 2010). Parabolic PDEs are usually solved using the so-called "marching" methods (*Sethian*, 1996). The diffusion equation (*Giordano and Nakanishi*, 2006) is one example of a parabolic PDE

$$\frac{\partial \rho}{\partial t} = \frac{\partial}{\partial x}\left(D\frac{\partial \rho}{\partial x}\right), \tag{3.41}$$

with D being the diffusion coefficient.

Hyperbolic PDEs also describe initial value boundary problems, and are also solved using "marching" methods. However, in contrast to parabolic equations, the speed at which the perturbations propagate in the hyperbolic PDEs is finite. An example of a hyperbolic PDE is the wave equation (*Giordano and Nakanishi*, 2006)

$$\frac{\partial^2 f}{\partial t^2} = v^2 \frac{\partial^2 f}{\partial x^2}, \tag{3.42}$$

with v being the finite velocity.

Elliptic PDEs are quite interesting in the sense that a disturbance at a point in the domain propagates isotropically at an infinite speed. In the physical sense, the propagation tries to nullify the steep difference in the gradient (*Brio et al.*, 2010). Compared to the parabolic and hyperbolic PDEs,

elliptic PDEs are solved numerically using "relaxation" methods (*Hoffman and Frankel*, 2001). The Poisson equation (*Giordano and Nakanishi*, 2006) is a good example of an elliptic PDE

$$\frac{\partial^2 f}{\partial x^2} + \frac{\partial^2 f}{\partial y^2} = \rho(x, y), \tag{3.43}$$

with ρ an arbitrary function.

3.3.2 Boundary Conditions

Each PDE has a domain on which it can be solved in n-dimensional space, which contains an infinite number of possible solutions. Sufficient information must therefore be specified on the boundaries of this domain to determine the unique solution. The sets of information specified at the boundary nodes are called *boundary conditions* of the governing equation. Below, the three most common boundary conditions on the interval $[0, N]$ are discussed.

3.3.2.1 Dirichlet or Fixed Value Boundary conditions

$$u\,(0) = u_L\,;\, u\,(N) = u_R. \tag{3.44}$$

The solution is specified at the boundary nodes (*Mazumder*, 2015) with u_L and u_R, representing the left and right boundaries.

3.3.2.2 Neumann or Derivative Boundary conditions

$$u\,(0) = u_L\,;\, \frac{du}{dx}\Big|_{x=N} = \text{constant}. \tag{3.45}$$

The solution is specified on the left boundary node, whereas on the right boundary node the slope is specified (*Mazumder*, 2015).

3.3.2.3 Robbins or Mixed Boundary conditions

$$u\,(0) = u_L\,;\, a\frac{du}{dx}\Big|_{x=N} + bu(N) = \text{constant}. \tag{3.46}$$

The solution is specified on the left boundary node. On the right boundary node, a combination of the solution and the slope is specified. The *Robbins condition* encompasses the *Dirichlet* and *Neumann conditions*, i.e setting $a = 0$ in Equation (3.46) yields the *Dirichlet condition* whereas setting $b = 0$ yields the *Neumann condition* (*Mazumder*, 2015).

3.4 The Diffusion Equation

The previous section provided a physical meaning to the diffusion equation, whereas this section shall now consider it numerically. As given by *Giordano and Nakanishi* (2006), the diffusion equation can be written as

$$\frac{\partial \rho}{\partial t} = \frac{\partial}{\partial x}\left(D\frac{\partial \rho}{\partial x}\right). \tag{3.47}$$

Utilizing Equations (3.26) and (3.29) on the left and right hand sides of Equation (3.47), respectively, the discretized version is obtained as

$$\frac{\rho_i^{n+1} - \rho_i^n}{\Delta t} = D\frac{\rho_{i+1}^n - 2\rho_i^n + \rho_{i-1}^n}{(\Delta x)^2}. \tag{3.48}$$

Note that a constant value of D is assumed in Equation (3.48). By rearranging Equation (3.48) the density ρ, at time step $n+1$, is obtained

$$\rho_i^{n+1} = \rho_i^n + \frac{D\Delta t}{(\Delta x)^2}[\rho_{i+1}^n + \rho_{i-1}^n - 2\rho_i^n]. \tag{3.49}$$

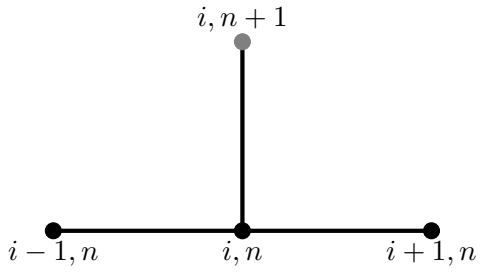

Figure 3.2: *The numerical stencil of the forward-difference explicit method.*

Equation (3.49) is called the forward-time central space (FTCS) method, and its numerical stencil is shown in Figure 3.2. An explicit scheme involves a simple updating procedure, which does not depend on other values at the current level, whereas an implicit scheme contains information at the current level which requires the solving of simultaneous equations (*Iserles*, 1986).

Equation (3.47) was solved numerically using the FTCS numerical scheme for an initial delta-function specified as $\delta(x,t)$, with boundary conditions of $\rho[0] = 0$, and $\rho[N] = 0$ on an interval of $N = 100$, with spatial and temporal time-steps of $dx = 0.01$ and $dt = 3.0609 \times 10^{-5}$. Figure 3.3 shows the density ρ at three different time-steps. It is clear that the density "smears" out for larger time steps. To understand this, consider the fact that at any particular time the spatial distribution has a Gaussian form. As the time steps increase, the density retains it's Gaussian form, but the width increases with time (*Giordano and Nakanishi*, 2006).

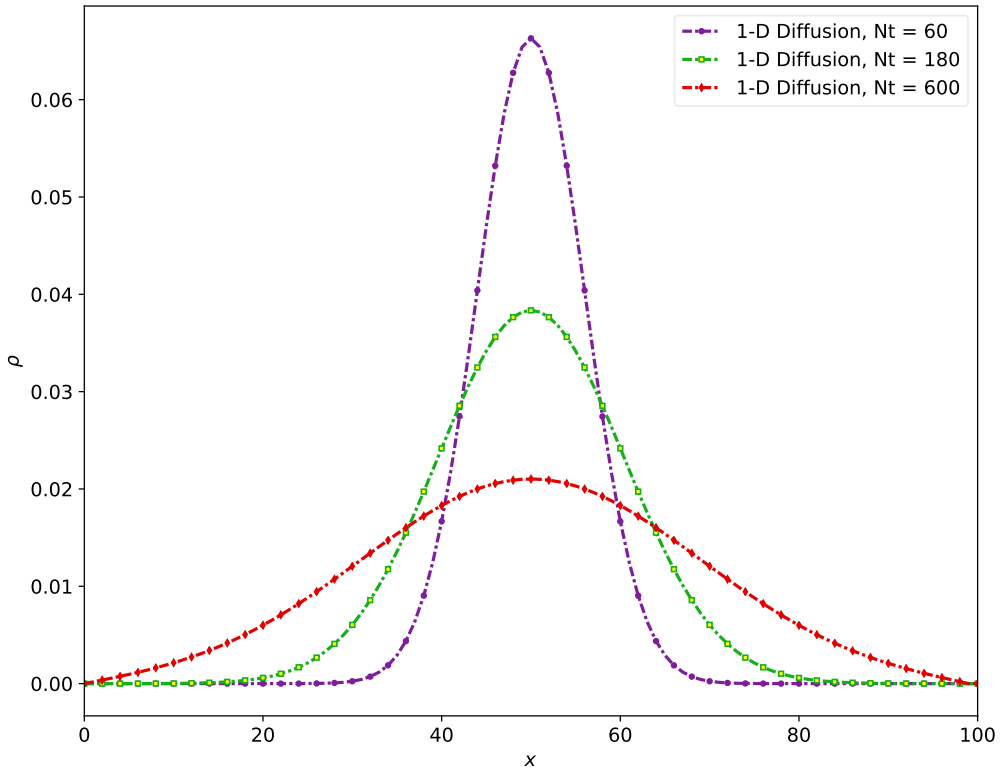

Figure 3.3: *Numerical solution of the diffusion equation for different time steps for $D = 1$.*

3.5 Stability Considerations

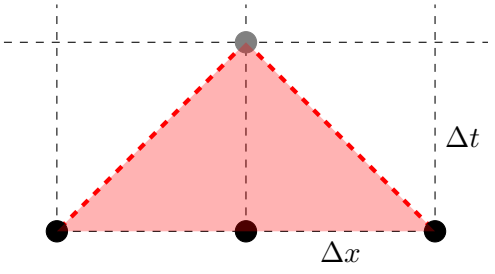

Figure 3.4: *Example of a 1D numerical grid. The red area indicates the distance that information can travel during one integration step (Δt), based on the stencil given in Fig. 3.2.*

For numerical stability, the choice of time step Δt has to depend upon the spatial grid size Δx and the speed at which information propagates in the system under consideration. Under the Courant-Friedrichs-Levy (CFL) condition (*Courant et al.*, 1967), stability is ensured when

$$\frac{u\Delta t}{\Delta x} \leq 1 \implies u\Delta t \leq \Delta x. \tag{3.50}$$

The CFL condition is implemented for each of the methods used to solve the 1D diffusion and advection equations, where u is the magnitude of the physical speed.

As shown in Figure 3.4, the distance $u\Delta t$ covered by the numerical method in one time step Δt must remain within the domain of dependence (and thus not exceed Δx) in order to satisfy the CFL condition, subsequently allowing the numerical scheme to remain stable. Figure 3.5a is an example of a stable numerical scheme, where the blue characteristic line lies within the domain of dependence.

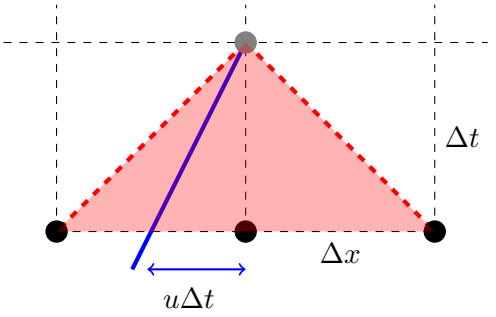

(a) *An example of a stable numerical scheme.*

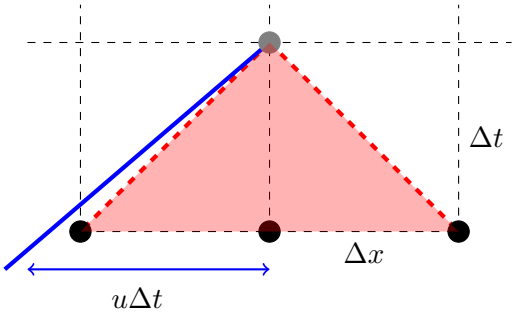

(b) *An an example of an unstable numerical scheme.*

Figure 3.5: *Example solutions of stable and unstable numerical schemes associated with finite-difference methods.*

An unstable numerical scheme would be one in which physical information moves faster than the speed at which the numerical scheme updates the information. In a numerical scheme, information travels a distance Δx during each integration step Δt. Information therefore travels at a speed of $\Delta x/\Delta t$, which is the so-called numerical speed v_{num}. For a numerical scheme to be stable, physical information travelling at speed u needs to move more slowly than v_{num}. This is the case shown in Equation (3.50). Conversely, for an unstable numerical scheme, as shown in Figure 3.5b,

$$u\Delta t \geq \Delta x. \tag{3.51}$$

To interpret the above discussion fully, consider the diffusion equation, where particles propagate diffusively at a speed of (*Strauss et al.*, 2011)

$$U_{\text{diff}} = \frac{2D}{\Delta x}. \tag{3.52}$$

Inserting Equation (3.52) into Equation (3.50) yields

$$\frac{\Delta x}{\Delta t} \geq \frac{2D}{\Delta x}, \tag{3.53}$$

or equivalently

$$v_{\text{num}} \geq U_{\text{diff}}. \tag{3.54}$$

Equation (3.54) implies that the numerical speed in the diffusion equation must be greater than the physical diffusion speed as given by Equation (3.52) for the numerical scheme to remain stable. The condition in Equation (3.54) holds for all other numerical schemes, i.e. the numerical scheme has to propagate the information in a realistic manner, otherwise physical changes will not be accounted for by the numerics (*Brio et al.*, 2010).

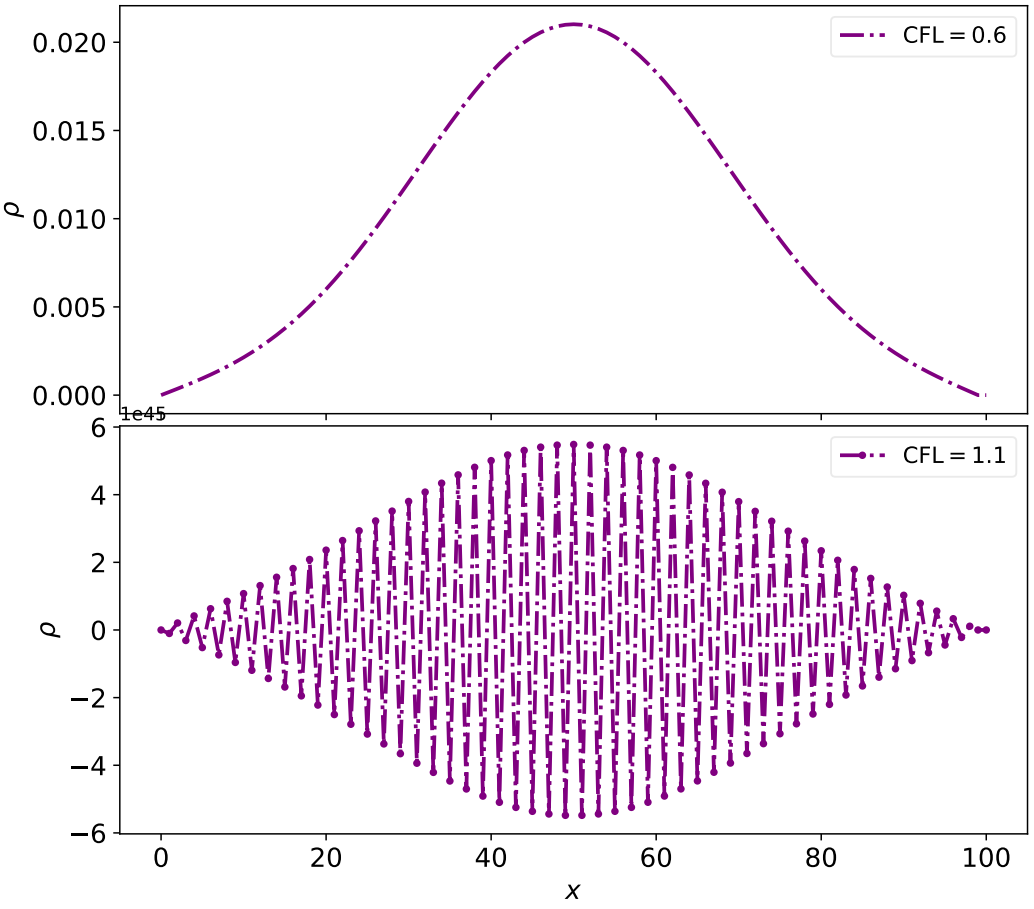

Figure 3.6: *Numerical solution of the diffusion equation for two choices of the CFL coefficient.*

To demonstrate, Equation (3.47) was solved again, using the same conditions described for Figure 3.3. However, in this case two different values of the CFL condition were used, i.e. CFL = 0.6 and CFL = 1.1, where $\Delta t = \text{CFL} \cdot \Delta x / u$. A time-step of $Nt = 600$ was used in both cases. Figure 3.6 illustrates the results of this. As expected, the diffusion equation is stable for CFL < 1, and becomes woefully unstable for CFL > 1.

3.6 Advection Equations

Various flux assignment methods that can be used to solve conservation laws are discussed below. Advection equations are a special class of conservative hyperbolic equations in which the temporal

derivative of the conserved quantity is proportional to the spatial derivative of the conserved quantity (*Trac and Pen*, 2003). Consider the 1D linear advection equation as a simple test case, given by

$$\frac{\partial u}{\partial t} + \frac{\partial F(u)}{\partial x} = 0, \tag{3.55}$$

where $F(u) = vu$, with u being the conserved quantity and v the assumed constant speed. The general analytical solution of Equation (3.55) is $u(x,t) = u(x - vt, 0)$, which represents a wave moving in the positive x-direction with a constant speed v.

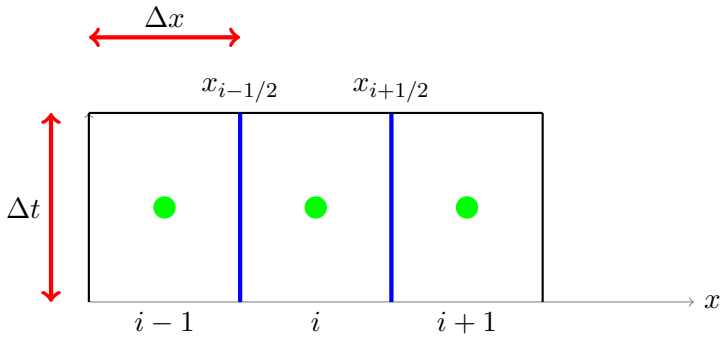

Figure 3.7: *A schematic illustration of flux propagation at cell interfaces.*

Writing Equation (3.55) in an integral flux conservation form yields

$$\frac{\partial}{\partial t}\int_{x_1}^{x_2} u(x,t)dx + \int_{x_1}^{x_2} \frac{\partial F(u)}{\partial x}dx = 0, \tag{3.56}$$

where $x_1 = x_{i-1/2}$ and $x_2 = x_{i+1/2}$. As shown in Figure 3.7, the fluxes of u through the cell interfaces (blue lines) $x_{i+1/2}$ and $x_{i-1/2}$ are denoted by $F^n_{i+1/2}$ and $F^n_{i-1/2}$, respectively. The discretized solution is therefore

$$u_i^{n+1} = u_i^n + \left(\frac{F^n_{i+1/2} - F^n_{i-1/2}}{\Delta x}\right)\Delta t \tag{3.57}$$

where $u(x,t) = u(i\Delta x, n\Delta t) = u(i,n)$.

3.6.1 Central Space Finite-Difference Method

From Figure 3.7, it can be seen that the fluxes at the cell interfaces (blue lines in Figure 3.7) can be expressed in terms of a linear average of the cell center values

$$F^n_{i+1/2} = \frac{F^n_{i+1} + F^n_i}{2}, \tag{3.58}$$

and

$$F^n_{i-1/2} = \frac{F^n_i + F^n_{i-1}}{2}. \tag{3.59}$$

Inserting Equations (3.58), and (3.59) into Equation (3.57) yields

$$u_i^{n+1} = u_i^n + \left(\frac{F_{i+1}^n - F_{i-1}^n}{2\Delta x} \right) \Delta t, \tag{3.60}$$

which is equivalent to the FTCS scheme, as given by the stencil in Figure 3.2. Unfortunately this scheme is numerically unstable (*Trac and Pen*, 2003).

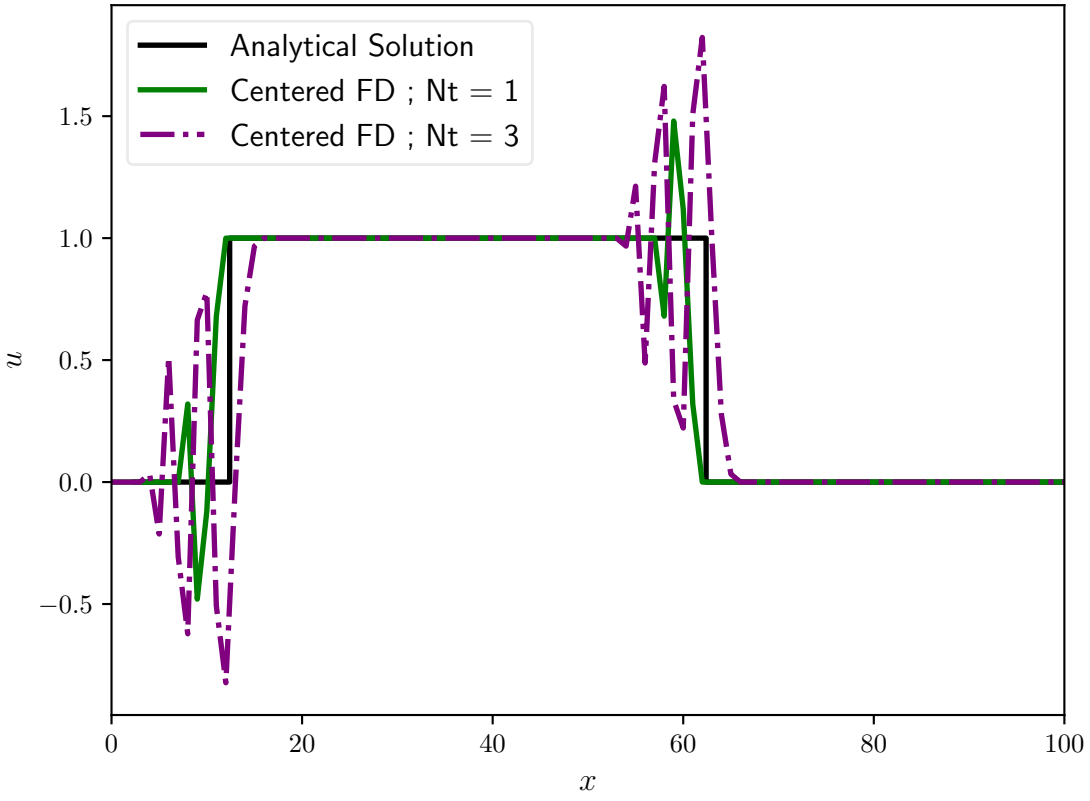

Figure 3.8: *An example of the instability in a first-order central space scheme.*

Equation (3.55) was solved numerically at two time-steps ($Nt = 1$ and $Nt = 3$) using the first-order central space (CS) numerical scheme for a block wave moving at an arbitrary speed $v = 1$, with boundary conditions of $u[0] = 0$ and $u[N] = 0$ on an interval of $N = 100$, with $dx = 0.01$ and $dt = 0.009$. As can be seen in Figure 3.8, the first-order CS scheme is numerically unstable (clearly visible even for smaller time-steps) and is thus not suitable for solving the linear advection equation. Von Neumann linear stability analysis can also be used to show that this numerical scheme is unstable (see e.g., *Trac and Pen*, 2003).

3.6.2 The Lax-Wendroff Scheme

Since the first-order central space scheme discussed in the previous section is numerically unstable for the 1D linear advection equation, the next logical step would be to try and solve the linear advection equation with a second-order numerical scheme. The Lax-Wendroff scheme (*Lax and Wendroff*, 1960) is second-order accurate in space and time, and should thus stabilize the first-order scheme in the previous section. To interpret this, consider a Taylor series expansion for $u(x, t + \Delta t)$,

$$u(x, t + \Delta t) = u(x, t) + \frac{\partial u}{\partial t}\Delta t + \frac{\partial^2 u}{\partial t^2}\frac{\Delta t^2}{2} + \mathcal{O}(\Delta t^3). \tag{3.61}$$

Using the conservation law, as given by Equation (3.55), Equation (3.61) becomes

$$u(x, t + \Delta t) = u(x, t) - \frac{\partial F}{\partial x}\Delta t + \frac{\partial}{\partial x}\left(\frac{\partial F}{\partial u}\frac{\partial F}{\partial u}\frac{\partial u}{\partial x}\right)\frac{\Delta t^2}{2} + \mathcal{O}(\Delta t^3), \tag{3.62}$$

where the time derivatives are replaced with spatial derivatives (*Trac and Pen*, 2003). Discretizing using the central difference formula, and noting that for the linear advection equation $\partial F/\partial u = v$, yields

$$u_i^{n+1} = u_i^n - \left(\frac{F_{i+1}^n - F_{i-1}^n}{2\Delta x}\right)\Delta t + \left(\frac{F_{i+1}^n - F_i^n}{\Delta x} - \frac{F_i^n - F_{i-1}^n}{\Delta x}\right)\frac{v\Delta t^2}{2\Delta x}. \tag{3.63}$$

Equation (3.63) is called the Lax-Wendroff scheme, where $u(x, t) = u(i\Delta x, n\Delta t) = u(i, n)$, and has the numerical stencil illustrated in Figure 3.9.

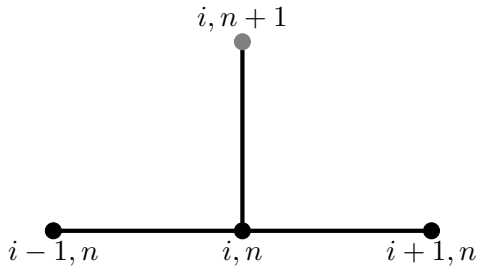

Figure 3.9: *The numerical stencil of the Lax-Wendroff numerical scheme. This stencil is identical to that of the FTCS scheme, shown in Figure 3.2.*

The Lax-Wendroff numerical scheme was used to solve Equation (3.55) numerically, at two different time-steps ($Nt = 10$ and $Nt = 50$). Again, a block wave was used as the initial condition, moving at an arbitrary speed $v = 1$. The boundary conditions were taken to be $u[0] = 0$, and $u[N] = 0$, with $dx = 0.01$ and $dt = 0.001$. In Figure 3.10, the linear advection of a block wave using the Lax-Wendroff scheme is shown. As seen in the figure, the Lax-Wendroff scheme is highly dispersive (*Trac and Pen*, 2003), and as a result produces numerical oscillations. The fact that these oscillations are expected to grow at larger time-steps is also evident in the figure. The origin of these random oscillations and various ways in which they can be "suppressed" in numerical schemes shall be discussed in Section 3.7. For now, to avoid oscillations due to the phase errors of the Lax-Wendroff scheme, an implementation

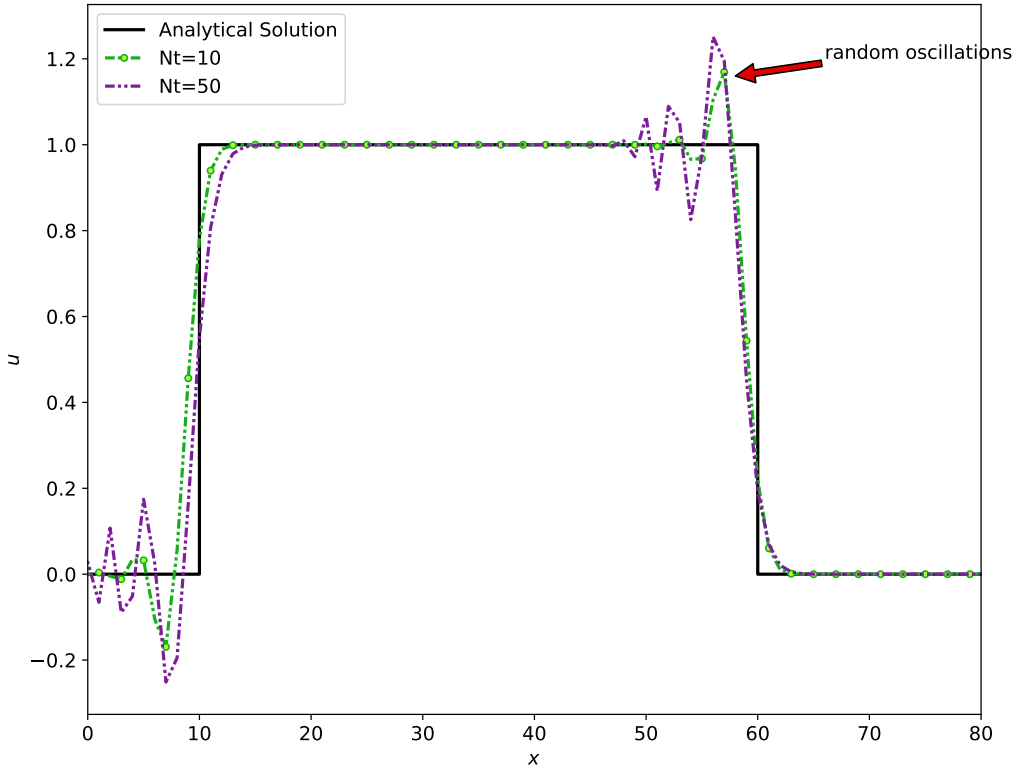

Figure 3.10: *Advection of a linear advective square-wave using the Lax-Wendroff scheme. A square-wave initial condition was used, for a grid of* $Nx = 100$ *cells and* $Nt = 30$ *timesteps, at a speed of* $v = 1$*, with* $dx = 0.01$ *and* $dt = 0.001$*.*

of the first-order upwind scheme in solving the linear advection equation is examined (*Trac and Pen*, 2003).

3.6.3 The Forward Upwind Scheme

The first-order upwind scheme resulted from work done by *Courant et al.* (1967). Upwind methods take into account the direction of flow when assigning fluxes for the discrete solution. The upwind scheme can be classified into either a forward-time forward space (FTFS) or a forward-time backward space (FTBS) scheme, with the convective velocities being negative and positive, respectively.

The first-order upwind scheme can therefore be summarized as follows

$$F^n_{i+1/2} = \begin{cases} F^n_i & \text{if } v > 0 \\ F^n_{i+1} & \text{if } v < 0. \end{cases} \tag{3.64}$$

By looking at Figure 3.7 for $v > 0$, the flux through the cell interface $x_{i+1/2}$ should start from the cell center i and flow to the right, whereas for $v < 0$ the flux should start from the cell center at $i + 1$ and flow to the left. Since the focus here is only on examples with positive flows, the linear advection

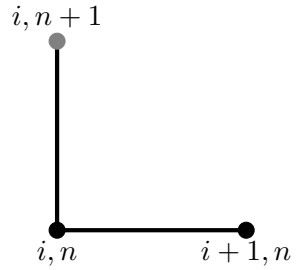

(a) *FTFS numerical scheme stencil, applied when $v < 0$.*

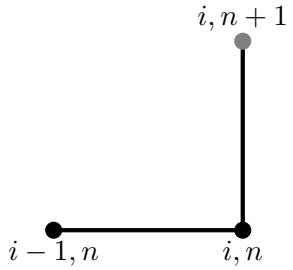

(b) *FTBS numerical scheme stencil, applied when $v > 0$.*

Figure 3.11: *Numerical stencil for the first-order upwind scheme.*

equation is solved with the FTBS numerical scheme, i.e.

$$u_i^{n+1} = u_i^n - \frac{F_i^n - F_{i-1}^n}{\Delta x}\Delta t, \tag{3.65}$$

with its numerical stencil shown in the right panel of Figure 3.11. A block wave was used as the initial

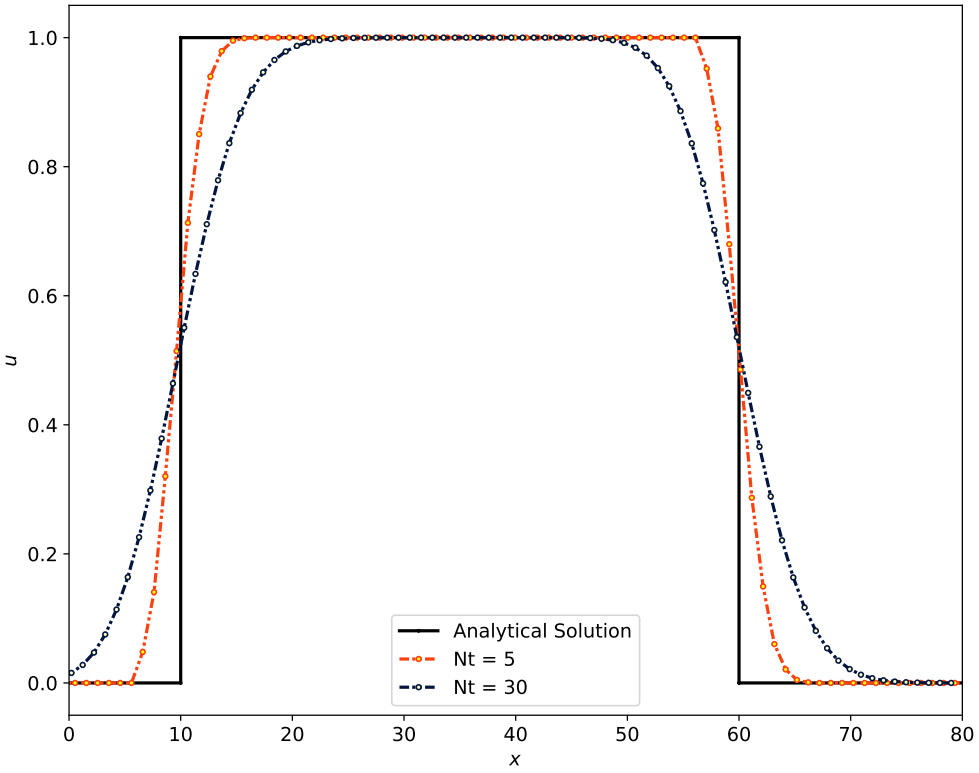

Figure 3.12: *Results of the first-order upwind scheme used to linearly advect a square wave through a box of 100 grid cells at a speed $v = 1$.*

condition, with boundary conditions on the left and right of an interval of $N = 100$ given by $u[0] = 0$ and $u[N] = 0$. A CFL number of 0.7 was assumed, with $dx = 0.010$ and $dt = 0.007$. In Figure 3.12, the results of the first-order upwind scheme for the advection equation are shown. In contrast to the

Lax-wendroff scheme, the first-order upwind scheme produces no spurious oscillations. However, *Trac and Pen* (2003) argue that this scheme is only first-order accurate, and is therefore highly diffusive. The authors further state that the first-order upwind scheme preserves monotonicity (produces no oscillations), whereas the Lax-Wendroff scheme does not, and that this is the cause of the spurious oscillations exhibited in the Lax-Wendroff scheme as visible in Figure 3.10.

Figure 3.12 confirms the highly diffusive nature of the first-order upwind scheme, as stated by *Trac and Pen* (2003). The numerical diffusion exhibited in this figure is expected to grow significantly at larger time-steps. According to *Godunov* (1959), all linear schemes are diffusive and/or dispersive. Fortunately non-linear schemes exist that can minimize these diffusive and/or dispersive numerical effects and give a higher order of accuracy (*Trac and Pen*, 2003).

3.7 Non-physical Oscillations and their Suppression

3.7.1 Origin of Non-physical Oscillations

In most finite numerical solutions the behaviour of the solution over a certain number of cells is known, but the behaviour of the gradient of the solution within the individual cells is unknown. This is the primary reason for sub-cell reconstructions. When doing sub-cell slope reconstructions in finite numerical schemes (in other words creating a sub-cell model based on discrete values at the cell centres) in the piecewise linear scheme, the first-order Godunov theorem is taken into account. This states that, if care is not taken in producing a reconstruction, it is impossible to have a physical solution that is free of oscillations or total variation diminishing (TVD; *Godunov* 1959; *Harten* 1983; *Wang* 2017). A flux assignment scheme is said to be oscillation free, or TVD, if

$$(\delta u^{n+1})^2 < (\delta u^n)^2, \tag{3.66}$$

where $(\delta u^{n+1})^2$ and $(\delta u^n)^2$ are the respective variances of u^{n+1} and u^n. Therefore, Equation (3.66) simply means that the overall number of oscillations is bounded (*Trac and Pen*, 2003). Oscillations are created at extrema, unless a non-linear scheme is employed to solve a linear equation.

Consider the solutions illustrated in Figure 3.13. Discretizing the solution in Figure 3.13a into cells of width Δx can provide insight into the possible slope changes within the individual cells via the cell centre solutions, denoted by ● in Figure 3.13b. To illustrate this point, consider the cell centre solution in cell U_i. A "good" sub-cell slope reconstruction for this cell would be one in which the orange line does not exceed the maximum cell center average value at U_{i-1}, nor does it go below U_{i+1}. A worst case sub-cell reconstruction would be one in which the sub-cell reconstruction exceeds the value of what the analytical solution should be, by either going above and/or below the analytical solution, as shown by the blue line in Figure 3.13b. This is the major reason for random oscillations

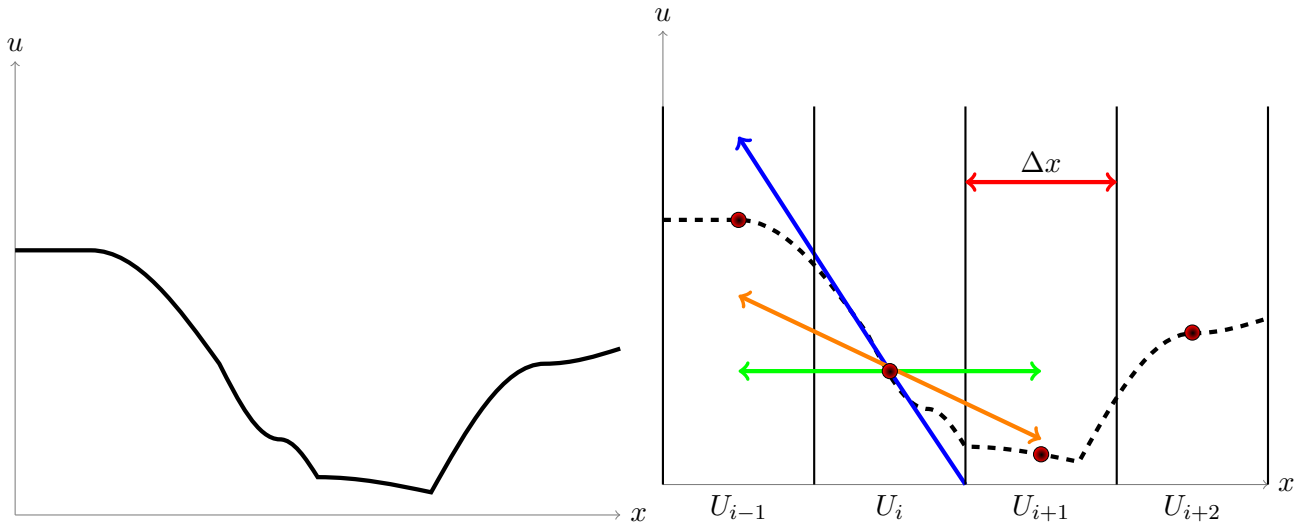

(a) *The function, u, being discretized.*

(b) *Illustration of the discretized solution of the function shown in the left panel.*

Figure 3.13: *An example solution of u on an x-grid, and it's discretization, used in illustrating the origin and/or suppression of numerical oscillations.*

in numerical models (*Wang*, 2017). Of course, sub-cell reconstruction in constant slope regions, as shown by the green line in Figure 3.13b, leads to a zero gradient.

First order accurate schemes are known to suffer from numerical diffusion, whereas classical higher order schemes generate spurious oscillations around discontinuities, while giving higher resolution at these discontinuities (*Sweby*, 1984). A good example of these "random" oscillations can be generated using the Lax-wendroff scheme (*Lax and Wendroff*, 1960), as shown earlier in Figure 3.10.

3.7.2 Slopes Near Discontinuities

From the previous section it is clear that sub-cell slope reconstruction by extrapolation is not the best way to go, especially near discontinuities or sharp jumps. Reconstructing the linear slope Δ within cell U_i, that is to say the gradient between the cell center U_i and the cell interface $U_{i+1/2}$, results in two extreme cases (*Wang*, 2017). The first case,

$$\Delta_{i\to i+1/2} = \frac{U_i - U_{i-1}}{\Delta x}, \tag{3.67}$$

occurs in an assumed linear region, i.e. $U_{i+1} - U_i = U_i - U_{i-1}$. This case allows sub-grid model reconstruction by linear extrapolation due to the linearity of the given region. The second case is given by

$$\Delta_{i\to i+1/2} = 0, \tag{3.68}$$

which can be interpreted as meaning that the cell center U_i is either a local maximum or minimum, and as a consequence the difference in cell centres $U_{i+1} - U_i$ and $U_i - U_{i-1}$ are expected to have

opposite signs, resulting in an overall slope of zero. In this case, a piecewise constant approximation is more applicable.

To minimize the "random" oscillations resulting from discontinuities in a solution, flux-limiters are employed to act as "switches" between first and second order schemes, or equivalently between linear or piecewise-constant approximations. With this in mind, Equation (3.67) is modified accordingly by the addition of a flux-limiter function ϕ, such that

$$\Delta_{i\to i+1/2} = \frac{U_i - U_{i-1}}{\Delta x}\phi\left(\frac{U_{i+1} - U_i}{U_i - U_{i-1}}\right). \tag{3.69}$$

The flux-limiter is a non-linear function that depends on the ratio of consecutive gradients $U_{i+1} - U_i$ and $U_i - U_{i-1}$, defined by

$$r \equiv \left(\frac{U_{i+1} - U_i}{U_i - U_{i-1}}\right). \tag{3.70}$$

From Equation (3.70) it is clear that if $r = 1$ (constant gradient), then $\phi = 1$ (second order) should be chosen and no spurious oscillations will occur, as Equation (3.69) reduces to the exact analytical solution as given by Equation (3.67). If $r \leq 0$, a choice of $\phi = 0$ (first-order) would be more appropriate as this type of scheme (e.g. the upwind scheme) would not lead to numerical oscillations near the larger gradient changes. The drawback is, of course, that the solution will only be first-order accurate near intensity jumps and/or regions where large gradients are present. From this, a piecewise function can be constructed for ϕ,

$$\phi = \begin{cases} 1 & \text{if } r = 1 \\ 0 & \text{if } r \leq 0 \end{cases}. \tag{3.71}$$

The piecewise function above displays the two basic constraints every limiter should satisfy. These constraints and others will be utilized later to construct a new type of limiter. A further constraint on flux-limiters is that the reconstructed sub-grid value should not exceed the value in the next cell (*Wang*, 2017), i.e.

$$U_i + \frac{\Delta x}{2}\Delta_{i\to i+1/2}\phi(r) \leq U_{i+1}. \tag{3.72}$$

Substituting Equation (3.67) into Equation (3.72) leads to

$$U_i + \frac{\Delta x}{2}\frac{U_i - U_{i-1}}{\Delta x}\phi(r) \leq U_{i+1}. \tag{3.73}$$

Thus

$$\phi(r) \leq 2\left(\frac{U_{i+1} - U_i}{U_i - U_{i-1}}\right), \tag{3.74}$$

and using Equation (3.70), this means that

$$\phi(r) \leq 2r. \tag{3.75}$$

Equation (3.75) gives a further constraint on what a limiter should be, that it should not exceed twice the ratio of the left and right derivatives.

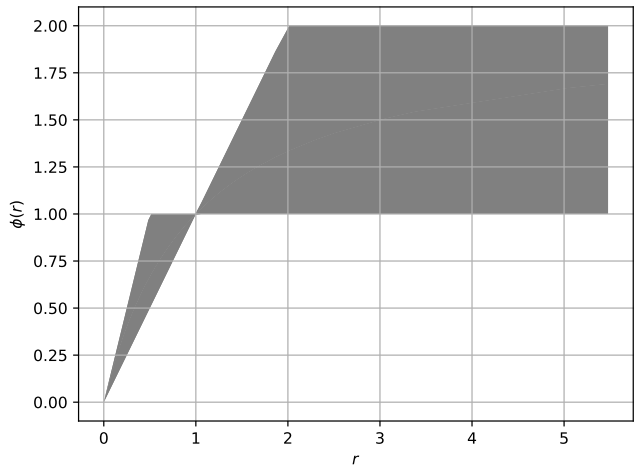

(a) *An illustration of the second-order TVD region associated with flux limiters (Sweby, 1984).*

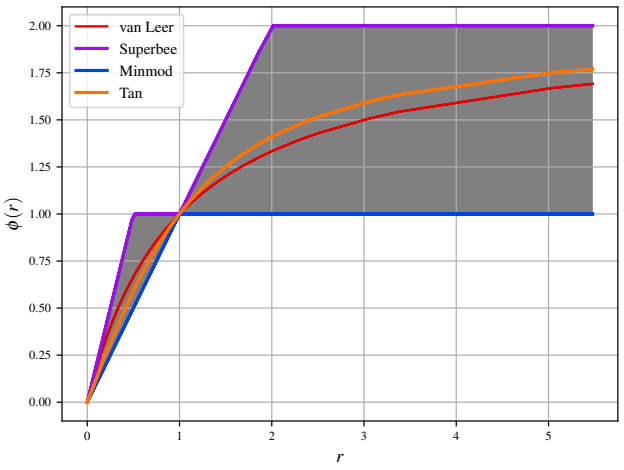

(b) *Similarly to Figure 3.14a, this figure shows the allowable region where a flux limiter can be applied (the shaded region).*

Figure 3.14: *The second-order TVD region, along with four different choices of flux limiters that are considered in this study (Sweby, 1984).*

Combining all three constraints results in the Sweby diagram (*Sweby*, 1984), which shows the viable region in which a non-linear function should operate in order to be called a flux limiter (*Wang*, 2017). This is shown as the shaded region of Figure 3.14a.

With Figure 3.14a in mind, an experimental limiter called the Tan limiter will be developed by constructing a non-linear function that fits well within the viable region and passes through the point $(\phi = 1, r = 1)$ which, according to *Sweby* (1984), is a general requirement for second order accuracy. In the next section, it will be shown that the Superbee (*Roe*, 1985) limiter follows the upper boundary of this region and that the Minmod limiter follows the lower boundary, with the van Leer (*van Leer*, 1974) and the proposed Tan limiter forming smooth curves between the Superbee and Minmod limiters.

3.8 Flux Limiters

3.8.1 Minmod Limiter

The Minmod limiter applies the most conservative reconstruction of all the second order TVD limiters, by choosing the smallest absolute value between the left and right corrections of the shaded region of Figure 3.14a. This limiter is therefore defined as

$$\phi = \min(1, r). \tag{3.76}$$

In analogy with Equation (3.72), the corresponding reconstructed Minmod gradient, with units of slope, is

$$\Delta_{\text{minmod}}(a,b) = \frac{1}{2}[\text{sign}(a) + \text{sign}(b)]\min(|a|,|b|), \tag{3.77}$$

where $a \equiv (U_i - U_{i-1})/\Delta x$ and $b \equiv (U_{i+1} - U_i)/\Delta x$ are the left and right gradients (*Trac and Pen*, 2003) that yield Equation (3.70). The Minmod limiter is shown in Figure 3.14b as the solid blue line.

3.8.2 Superbee Limiter

The Superbee limiter (*Roe*, 1985) does the opposite of the Minmod, in that it forms the upper boundary of the Sweby diagram. This limiter is shown in Figure 3.14b as the solid violet line and given as

$$\phi = \max(0, \min(1, 2r), \min(2, r)), \tag{3.78}$$

with the reconstructed Superbee gradient being

$$\Delta_{\text{superbee}}(a,b) = \begin{cases} \Delta_{\text{minmod}}(a, 2b) & \text{if } |a| \geq |b| \\ \Delta_{\text{minmod}}(2a, b) & \text{if otherwise} \end{cases}. \tag{3.79}$$

Again, $a \equiv (U_i - U_{i-1})/\Delta x$ and $b \equiv (U_{i+1} - U_i)/\Delta x$ are the left and right gradients, respectively. The Superbee limiter makes the most aggressive reconstruction possible by choosing between the larger gradient and twice the smaller gradient, whichever is smaller in magnitude (*Trac and Pen*, 2003).

3.8.3 van Leer Limiter

The van Leer limiter (*van Leer*, 1974) which serves as a compromise between the Superbee and Minmod limiters, is given by

$$\phi = \frac{2r}{1+r}, \tag{3.80}$$

and is shown as the solid red line in Figure 3.14b. As with the previous two limiters, the reconstructed van Leer gradient is

$$\Delta_{\text{vanLeer}}(a,b) = \frac{2ab}{a+b}, \tag{3.81}$$

where $a \equiv (U_i - U_{i-1})/\Delta x$ and $b \equiv (U_{i+1} - U_i)/\Delta x$ are the left and right gradients, respectively.

3.8.4 Tan Limiter

The newly developed Tan limiter forms a smooth curve, similar to that of the van Leer limiter. This limiter is shown as the orange line in Figure 3.14b and given as

$$\phi = \max(0, \tan(0.905)\arctan(r)), \tag{3.82}$$

with the reconstructed Tan gradient being

$$\Delta_{Tan} = \tan(0.905)\arctan\left(\frac{b}{a}\right)a. \tag{3.83}$$

Again, $a \equiv (U_i - U_{i-1})/\Delta x$ and $b \equiv (U_{i+1} - U_i)/\Delta x$ are the left and right gradients, respectively. The Tan limiter exhibits an interesting behaviour with respect to the van Leer limiter, where for $r \leq 0$, it does a "weaker" job at limiting the slope. At the critical point $(r = 1, \phi(r) = 1)$, it meets the general requirement for second order accuracy (*Sweby*, 1984), and after that critical point, the Tan limiter out-performs the van Leer limiter by making a slightly more aggressive reconstruction. It is worth noting that the Tan limiter was developed primarily to demonstrate an understanding on the workings of flux-limiters, and that the parameter values used were strictly obtained by trial and error, with the current parameter choices being the ones that fit well within the viable region of the Sweby diagram (see Figure 3.14a).

3.8.5 Validity of Flux-Limiters

To demonstrate the effectiveness of the various limiters discussed above, the linear advection equation (Equation (3.55)) is solved in the same way as done for Figure 3.12. Again, the FTBS numerical scheme is used, but in this case it is only used to calculate the solution at half the time-step of some quantity u being advected linearly as a block wave. This half-step solution is given by

$$u_i^{n+\frac{1}{2}} = u_i^n - v\frac{\Delta t}{2\Delta x}\left(u_i^n - u_{i-1}^n\right), \tag{3.84}$$

from which the left and right gradients a and b are found to be

$$a_i = \frac{u_i^{n+\frac{1}{2}} - u_{i-1}^{n+\frac{1}{2}}}{2\Delta x}, \tag{3.85}$$

and

$$b_i = \frac{u_{i+1}^{n+\frac{1}{2}} - u_i^{n+\frac{1}{2}}}{2\Delta x}. \tag{3.86}$$

From these gradients and their ratio, as given by Equation (3.70), the various flux-limiters considered in this study are constructed. The half-step solution, as given by Equation (3.84), and a choice of one of the four limiters discussed above is utilized to produce a corrected flux solution u^{COR}, given by

$$u_i^{\mathrm{COR}} = u_i^{n+\frac{1}{2}} + \Delta_{\mathrm{limiter}}\cdot\Delta x, \tag{3.87}$$

where $\Delta_{\mathrm{limiter}}$ is the flux-limiter corrected gradient. These corrected fluxes are then used to calculate the full time-step

$$u_i^{n+1} = u_i^n - v\frac{\Delta t}{2\Delta x}\left(u_i^{\mathrm{COR}} - u_{i-1}^{\mathrm{COR}}\right). \tag{3.88}$$

As can be seen from Figure 3.15, the Superbee limiter gives the best reconstruction, followed by the van Leer and the Tan limiter giving roughly the same reconstruction. The Minmod limiter gives the lowest-accuracy reconstruction.

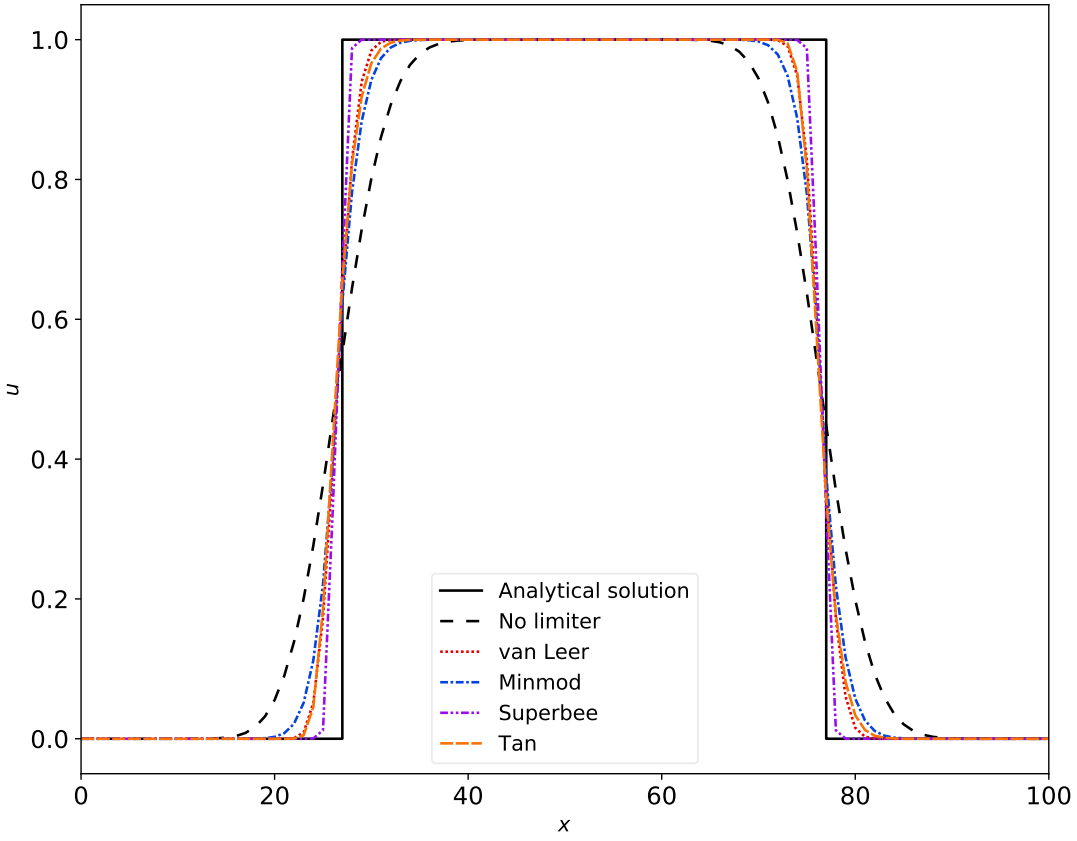

Figure 3.15: *Application of the Minmod, Superbee, van Leer, and the newly developed Tan limiter to the square-wave linear advection problem for a grid of 100 cells, 20 time steps, a velocity of* $v = 1.0$*,* $dx = 0.01$*, and* $dt = 0.0085$*.*

3.9 Summary and Conclusions

In this chapter, the various finite-difference formulae for several techniques are derived from first principles. Insight into the workings of these formulae was gained by means of their application to various examples. The application of FD numerical schemes to the diffusion and advection equations revealed a drawback of these numerical schemes, i.e. that they can be highly dispersive and/or diffusive, resulting in numerical oscillations in some cases. Fortunately, this drawback was shown to be significantly limited by the use of non-linear functions called flux-limiters. The workings of flux-limiters were illustrated, and subsequently led to the development of a new flux-limiter called the Tan limiter.

The Tan limiter was benchmarked against other well-known limiters such as the Superbee, Minmod, and van Leer limiters. It was found that when it comes to handling highly diffusive numerical schemes, the Superbee limiter gives the best reconstruction, followed by the van Leer and the Tan limiter, with the Minmod giving the lowest-accuracy reconstruction. It is thus safe to conclude that the Tan limiter holds its own against the well-known limiters.

CHAPTER 4

The Solar Energetic Particle Transport Model

4.1 Introduction

This chapter aims to develop a numerical scheme that can approximate the solution of the *Roelof* (1969) equation. This will be done by considering the various aspects of the transport model, the use of FD methods in model implementation, and the various assumptions on which the model is based.

4.2 Aspects of the Transport Model

The model takes into account the standard Parker (*Parker*, 1958) HMF described in Section 2.4.1, which is recast here into the form

$$B(r,\theta) = \frac{B_o r_o^2}{r^2}(\hat{r} - \tan\psi\hat{\phi}), \tag{4.1}$$

where B_o denotes the magnetic field strength at some position r_o, and ψ is the HMF spiral angle. This angle is rewritten from Equation (2.4) as

$$\tan\psi = \frac{\omega_\odot r \sin\theta}{v_{sw}}, \tag{4.2}$$

with $\omega_\odot$, v_{sw}, and θ being the earlier-defined angular rotation speed of the Sun, solar wind speed, and heliographic latitude, respectively. From the definition of the spiral angle, the variation of the radial

distance r with respect to the spiral angle ψ along a magnetic field line is found to be

$$dr = \frac{v_{sw}}{\omega_\odot \sin\theta} d(\tan\psi). \tag{4.3}$$

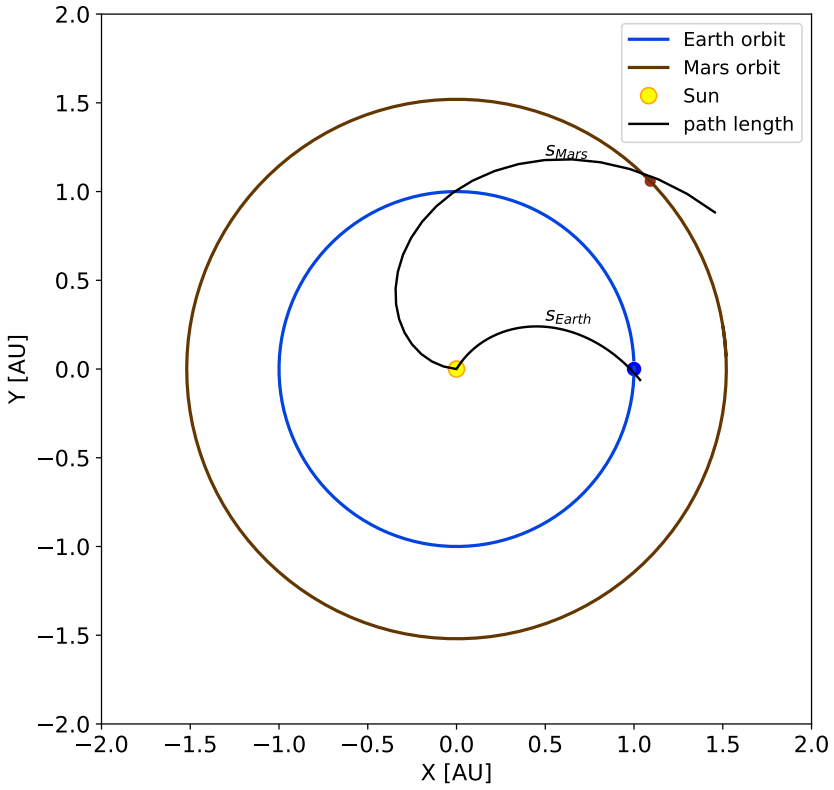

Figure 4.1: *The circular orbits of Earth and Mars along with two Parker HMF spirals connecting the planets to the Sun.*

Figure 4.1 shows the circular orbits of Earth and Mars, along with two Parker spirals connecting these planets to the Sun. According to *Lampa* (2011), energetic particles moving along a Parker magnetic field line will cover a path length s, given by

$$s = \int_0^{r_2} \sqrt{1 + \left(\frac{\omega_\odot \sin\theta r}{v_{sw}}\right)^2}\, dr. \tag{4.4}$$

To solve Equation (4.4), Equations (4.2) and (4.3) are used, yielding

$$s = \int \sqrt{1+\tan^2\psi}\, \frac{v_{sw}}{\omega_\odot sin\theta} d(\tan\psi), \tag{4.5}$$

and thus

$$s = \frac{v_{sw}}{\omega_\odot \sin\theta}\left[\frac{\tan\psi}{2}\sqrt{1+\tan^2\psi} + \frac{1}{2}\ln\left(\tan\psi + \sqrt{1+\tan^2\psi}\right)\right] + C_0. \tag{4.6}$$

Using initial conditions of $\tan\psi = 0$ at $s = 0$, the constant C_0 is found to be zero. Assuming $v_{sw} = 400$ km·s^{-1}, the path lengths to Earth ($r = 1.0$ AU) and Mars ($r = 1.52$ AU) are found to be $s_{\text{Earth}} \approx 1.17$ AU, and $s_{\text{Mars}} \approx 2.04$ AU, respectively. These HMF lines are shown in Figure 4.1.

The Roelof equation (Equation (2.36)) is rewritten in the form

$$\frac{\partial f}{\partial t} + \frac{\partial}{\partial z}(\mu v f) + \frac{\partial}{\partial \mu}\left(\frac{1-\mu^2}{2L} v f\right) = \frac{\partial}{\partial \mu}\left(D_{\mu\mu}(x,\mu)\frac{\partial f}{\partial \mu}\right), \tag{4.7}$$

which holds for 1D SEP motion along a magnetic field directed along $\mathbf{e}_z$.

The model is limited to the ecliptic regions of the inner heliosphere, an inclination of $\theta \approx 90°$ and thus an assumption of $\sin\theta = 1$ is acceptable throughout. The terms in Equation (4.7) describe particle streaming along the magnetic field in the z-direction, focusing in diverging field lines, and pitch-angle scattering, respectively (see Section 2.7.3). When the streaming and focusing terms dominate, the overall equation tends to display a hyperbolic nature, whereas when the diffusion term dominates the equation tends to be increasingly parabolic (see e.g., *Strauss and Fichtner*, 2015). Given the above, it is not possible for a single numerical scheme to solve this equation. To overcome this problem, the so-called operator splitting technique (see e.g., *Marchuk*, 1990; *Hatzky*, 1999; *Lampa*, 2011) is utilized.

4.3 Locally One-Dimensional (LOD) Method

The locally one-dimensional (LOD) method is one of the operator splitting methods commonly called fractional-step and split-step methods (see e.g., *Steenkamp*, 1995). These methods are based on the idea that, when PDEs encompass different terms, with each term describing some distinct physical process, a numerical scheme is required that takes the different processes into consideration.

The LOD method (see e.g., *Steenkamp*, 1995; *Holden et al.*, 2010) involves splitting a PDE along the respective coordinates. Consider a PDE of the form

$$\frac{\partial u}{\partial t} = b_1 \frac{\partial^2 u}{\partial x^2} + b_2 \frac{\partial^2 u}{\partial y^2}. \tag{4.8}$$

The differential operator for Equation (4.8) is defined as

$$\mathcal{L} = b_1 \frac{\partial^2}{\partial x^2} + b_2 \frac{\partial^2}{\partial y^2}. \tag{4.9}$$

Given that the coefficients b_1 and b_2 are independent of u, the differential operator $\mathcal{L}$ can be written as a linear combination of individual differential operators $\mathcal{L}_1 = b_1\partial^2/\partial x^2$ and $\mathcal{L}_2 = b_2\partial^2/\partial y^2$, to yield

$$\mathcal{L} = \mathcal{L}_1 + \mathcal{L}_2. \tag{4.10}$$

Thus Equation (4.8), in terms of the linear combinations, can be expressed as

$$\frac{\partial u}{\partial t} = \mathcal{L}_1 u + \mathcal{L}_2 u, \tag{4.11}$$

or

$$u_t = \mathcal{L}_1 u + \mathcal{L}_2 u. \tag{4.12}$$

The LOD method in this case involves splitting the PDE along both spatial dimensions x and y, to yield

$$\frac{1}{2}u_t = b_1 u_{xx} \tag{4.13}$$

and

$$\frac{1}{2}u_t = b_2 u_{yy} \tag{4.14}$$

for each half time step, given that $\mathcal{L}$ is linear (*Steenkamp*, 1995).

4.3.1 LOD solution of the Roelof Equation

The Roelof equation is split along both spatial and pitch-angle coordinates, as well as along the second-order term. This results in three 1D differential equations, two of which are first-order and one being of second-order, given by

$$\frac{1}{3}\frac{\partial f}{\partial t'} = \frac{\partial f}{\partial t} = -\frac{\partial}{\partial z}(\mu v f), \tag{4.15}$$

$$\frac{1}{3}\frac{\partial f}{\partial t'} = \frac{\partial f}{\partial t} = -\frac{\partial}{\partial \mu}\left(\frac{1-\mu^2}{2L} v f\right), \tag{4.16}$$

and

$$\frac{1}{3}\frac{\partial f}{\partial t'} = \frac{\partial f}{\partial t} = \frac{\partial}{\partial \mu}\left(D_{\mu\mu}\frac{\partial f}{\partial \mu}\right) = \frac{\partial D_{\mu\mu}}{\partial \mu}\frac{\partial f}{\partial \mu} + D_{\mu\mu}\frac{\partial^2 f}{\partial \mu^2}. \tag{4.17}$$

where $\partial t' = \partial t/3$. The operator-splitting technique allows different numerical schemes and/or different boundary conditions to be applied to each equation. However, it is only accurate to first order (*Strauss and Fichtner*, 2015).

4.4 Finite-Difference solution of the Roelof equation

Applying the numerical schemes described in Chapter 3 to the split equations, i.e. Equations (4.15-4.17), the programmable equations are

$$\frac{f_i^{n+1} - f_i^n}{\Delta t} = -\frac{F_i^n - F_{i-1}^n}{\Delta z}, \tag{4.18}$$

with $F_i^n = \mu v f_i^n$,

$$\frac{f_i^{n+1} - f_i^n}{\Delta t} = -\frac{F_i^n - F_{i-1}^n}{\Delta \mu}, \tag{4.19}$$

with $F_i^n = v\left((1-{\mu_i}^2)/2L\right) f_i^n$, and

$$\frac{f_i^{n+1}-f_i^n}{\Delta t} = \frac{\partial D_{\mu\mu}}{\partial \mu}\left[\frac{f_{i+1}^n - f_{i-1}^n}{2\Delta\mu}\right] + D_{\mu\mu}\left[\frac{f_{i+1}^n - 2f_i^n + f_{i-1}^n}{\Delta\mu^2}\right]. \tag{4.20}$$

The advection (streaming and focusing) terms use the upwind scheme (see Section 3.6.3) with an option of four limiters, namely the Superbee, Minmod, van Leer, and the newly-constructed Tan limiter. In the next chapter the effectiveness of various flux-limiter combinations for the z, and μ coordinates will be shown. The diffusion term, on the other hand, is solved using a FTCS scheme (see section 3.4), as done by *Strauss and Fichtner* (2015).

4.5 Model Assumptions

Several assumptions are made, one of which is that of a uniform background medium. This implies a constant solar wind speed and a Parker spiral field. Furthermore, a constant radial mean free path λ_{rr} is assumed, from which the parallel mean free path $\lambda_{\parallel}$ is calculated. Lastly, the model solves only for the SEP distribution along a single HMF line.

4.5.1 Boundary conditions

The overall numerical scheme involves prescribing an injection function at the inner boundary z_0 of the form

$$f(z) = C\cdot \exp\left[-\frac{(z-z_0)^2}{z_0^2}\right], \tag{4.21}$$

with C being some constant. A delta-like injection in z is assumed at $z_0 = 0.05$ AU, with $z_0^2 = 0.0005$ AU^2, and an absorbing boundary situated at a heliocentric distance well beyond Mars orbit (see e.g., *Strauss and Fichtner*, 2015).

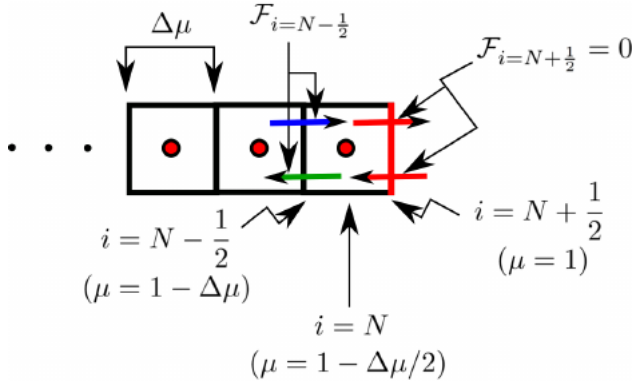

Figure 4.2: *An illustration of flux propagation across cell interfaces in solving for μ (Strauss and Fichtner, 2015).*

On the other hand, the boundary conditions for μ demand a logical way of keeping track of the fluxes moving along a grid of N-cells, across cells of width $\Delta\mu$ via cell interfaces situated at $i = N \pm 1/2$ as shown in Figure 4.2. Consider the cell for which $i = N$, with a cell-centre solution f_i, which in terms of the μ-grid is positioned at $\mu = 1 - \Delta\mu/2$. To determine the flux boundary conditions for f_i, a technique employed by *Strauss and Fichtner* (2015) is used. This involves scrutinizing the fluxes entering and exiting this cell, as shown by the blue and green arrows in Figure 4.2. The flux through the cell interface $i = N + 1/2$, denoted by the red arrows in Figure 4.2, is always zero due to the behaviour of the pitch-angle diffusion and focussing coefficients at the extrema of μ. These author's technique allows f_i to be computed in the following manner at the boundaries

$$f_{i=N}^{n+\Delta n} = f_{i=N}^{n} + \frac{\Delta t}{\Delta \mu} F_{i=N-1/2}^{n}, \tag{4.22}$$

with $F_{i=N-1/2}^{n}$ denoting the flux traversing back and forth through cell interface $i = N - 1/2$. Thus

$$F_{i=N-1/2}^{\text{advective}} = \frac{v\,(1-\mu_i)^2}{2L} f_i^n\Big|_{i=N-1} \tag{4.23}$$

for the μ-advection term, whereas the pitch-angle diffusion term is given by

$$F_{i=N-1/2}^{\text{diffusive}} = -\tilde{D}_{\mu\mu} \frac{\partial f}{\partial \mu}\Big|_{i=N-1/2}, \tag{4.24}$$

where

$$\tilde{D}_{\mu\mu} \approx \frac{1}{2}\{D_{\mu\mu,i=N} + D_{\mu\mu,i=N-1}\}. \tag{4.25}$$

The quantity $\partial f/\partial\mu\big|_{i=N-1/2}$ is approximated by a backward-difference formula, as given in Equation (3.27) to yield

$$\frac{\partial f}{\partial \mu}\Big|_{i=N-1/2} \approx \frac{f_{i=N}^{n} - f_{i=N-1}^{n}}{\Delta\mu}. \tag{4.26}$$

4.5.2 Coefficients

The coefficients of importance to this study are the focusing and pitch-angle diffusion coefficient (PADC). The focusing coefficient $\mathscr{B}$ is given by

$$\mathscr{B} = v\left(\frac{1-\mu^2}{2L}\right), \tag{4.27}$$

where the focusing length L is taken to be of the form (*He and Wan*, 2012)

$$L(r,\theta,V) = \frac{r(v_{sw}^2 + \omega_\odot^2 r^2 \sin^2\theta)^{3/2}}{v_{sw}(2v_{sw}^2 + \omega_\odot^2 r^2 \sin^2\theta)}, \tag{4.28}$$

again noting the assumption of $\sin\theta = 1$ in the present model. Figure 4.3 shows the behaviour of both the focusing length L and $\mathscr{B}$ with respect to the distance along the magnetic field z. A particle

speed of $v = 0.66$ AU·h^{-1} is assumed. As shown in the figure, the focusing term becomes increasingly important close to the Sun.

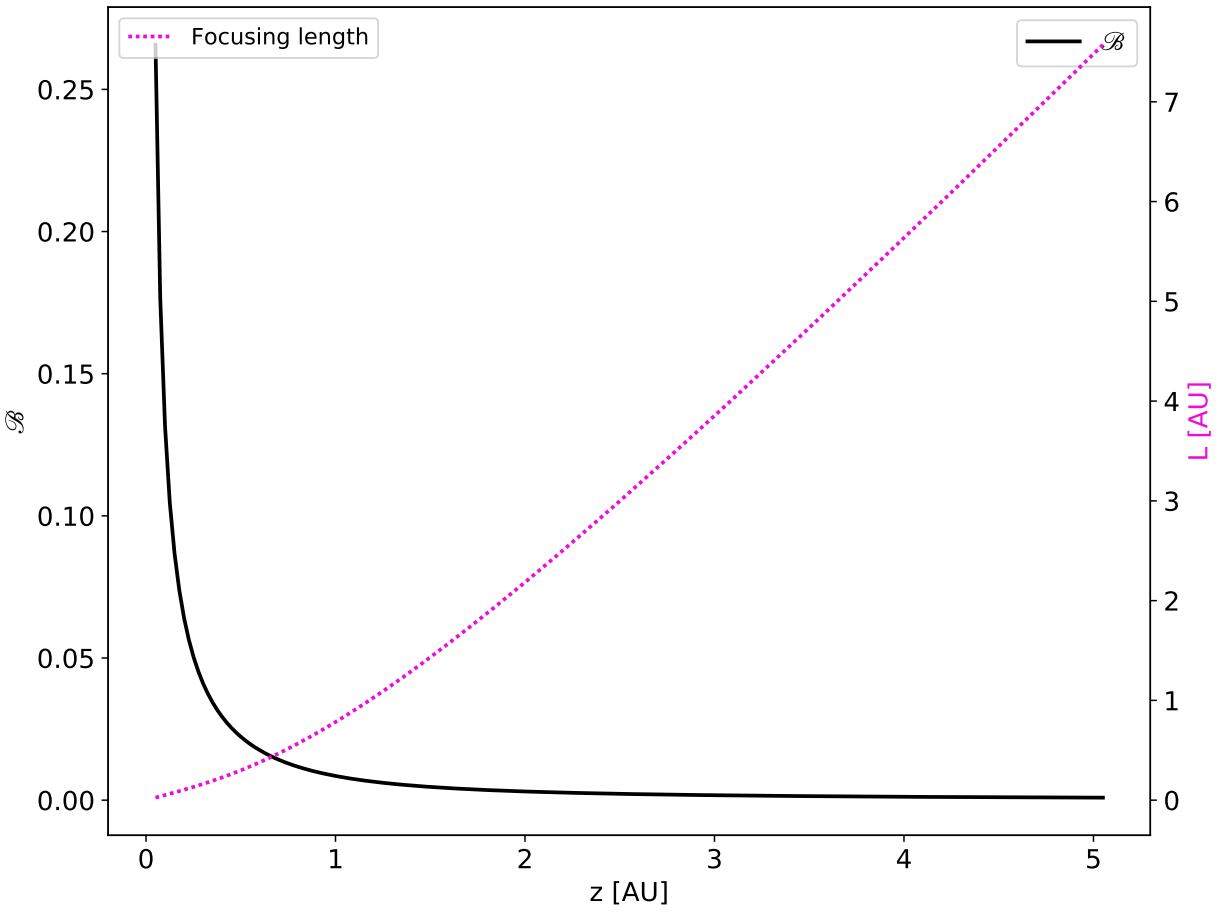

Figure 4.3: *Behaviour of the focusing length L and coefficient $\mathscr{B}$, with respect to the distance along the magnetic field line z.*

The PADC, discussed in Section 2.7.3.3, is parametrized as

$$D_{\mu\mu} = D_{\mu\mu,0} \left\{ |\mu|^{q-1} + H \right\} (1 - \mu^2). \tag{4.29}$$

In Figure 4.4, various forms of the PADC are shown. The model involves specifying a constant radial mean free path λ_{rr} (see e.g., *Bieber et al.*, 1994; *Strauss and Fichtner*, 2015) from which the parallel mean free path $\lambda_{\parallel}$ can be obtained. This is subsequently used to calculate the required magnitude $D_{\mu\mu,0}$. This is carried out by using $\lambda_{\parallel}$ in Equation (2.48), given by

$$\lambda_{\parallel} = \frac{3v}{8} \int_{-1}^{+1} \frac{(1 - \mu^2)^2}{D_{\mu\mu}} d\mu. \tag{4.30}$$

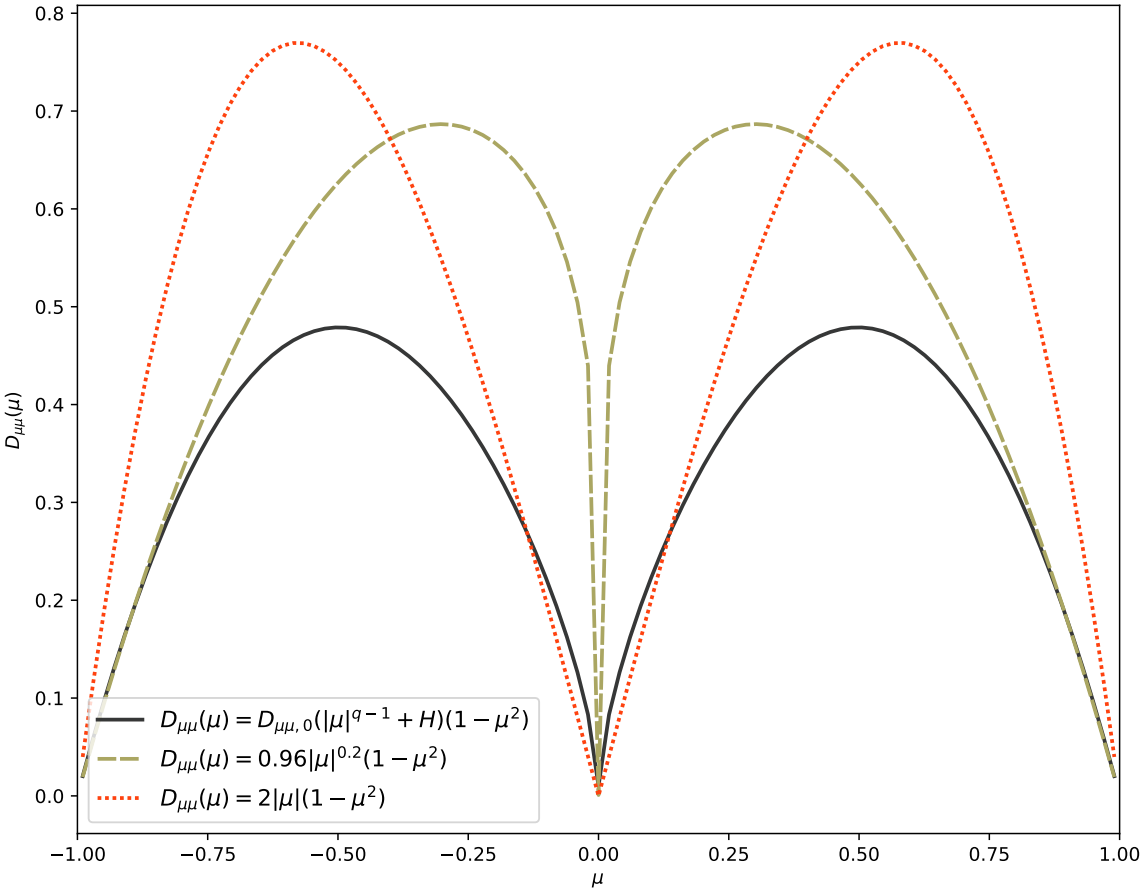

Figure 4.4: *Various forms of the pitch-angle diffusion coefficient with a consistent minimum near* $\mu = 0$. $D_{\mu\mu,0} = 1.0$ *is assumed throughout.*

Substitution of Equation (4.29) into Equation (4.30) yields

$$\lambda_{\parallel} = \frac{3v}{8}\int_{-1}^{+1} \frac{(1-\mu^2)^2}{D_{\mu\mu,0}\left\{|\mu|^{q-1} + H\right\}(1-\mu^2)} d\mu \tag{4.31}$$

$$= \frac{3v}{8}\frac{1}{D_{\mu\mu,0}} \cdot I,$$

where I is taken to be

$$I = \int_{-1}^{+1} \frac{(1-\mu^2)}{\{|\mu|^{q-1} + H\}} d\mu. \tag{4.32}$$

Thus from Equation (4.31) it can be shown that

$$D_{\mu\mu,0} = \frac{3v}{8} \cdot I \cdot \frac{1}{\lambda_{\parallel}}, \tag{4.33}$$

further noting that $\lambda_{\parallel}$ is related to λ_{rr} through (see e.g., *Bieber et al.*, 1994)

$$\lambda_{\parallel} = \lambda_{rr}/\cos^2\psi. \tag{4.34}$$

Using Equations (4.34) and (4.33) it can be shown that

$$D_{\mu\mu,0} = \frac{3v}{8} \cdot I \cdot \frac{\cos^2 \psi}{\lambda_{rr}}, \tag{4.35}$$

which is the required magnitude of $D_{\mu\mu}$. This quantity additionally serves as the model input, and more crucially, provides insight into the extent of particle scattering (see e.g., *He et al.*, 2011; *Strauss et al.*, 2017).

4.6 Standard model parameters

Table 4.1 shows the various standard parameters and corresponding values employed in this study. In the following chapters, these parameter values will serve as the basis for assorted simulation runs.

Parameter	**Value**	**Description**
v	0.66 AU·h^{-1}	particle's speed corresponding to 4 MeV protons
v_{sw}	0.0096 AU·h^{-1}	solar wind speed (v_{sw} = 400 km·s^{-1})
q	1.67	spectral index of inertial Kolmogorov range
H	0.05	non-linear effects correction parameter
r_0	0.05 AU	injection position
θ	1.5708 rad	heliographic latitude ($\theta \approx 90°$)
μ	$-1 \leq \mu \leq 1$	pitch-angle cosine
λ_{rr}	0.3 AU	radial mean free path
z	$0.05 \leq z \leq 5$ AU	distance along the HMF line

Table 4.1: *Standard set of parameters and corresponding values used in the study.*

4.7 Summary

This chapter treats the implementation of the finite-difference methods discussed earlier in developing a numerical scheme that can approximate the propagation of SEPs, as described by the *Roelof* (1969) equation. Furthermore, various assumptions crucial to the model were also examined, including boundary conditions for both the spatial and μ coordinates. Forms of the focusing and pitch-angle diffusion coefficients adapted in the study were also discussed.

CHAPTER 5

Benchmarking and Model Characteristics

5.1 Introduction

To test the validity and accuracy of the numerical model discussed in the previous chapter, this chapter shall primarily show how the model compares with various contemporary models. These are a finite-difference model by *Strauss and Fichtner* (2015), three stochastic differential equation (SDE) based models by *Effenberger and Litvinenko* (2014), *Dröge et al.* (2010), and a recent model by *van den Berg* (2018). Furthermore, key features of the model will be characterized with respect to an SEP event observed by the STEREO-B spacecraft on 7 February 2010. A secondary objective of this chapter is to infer the best flux-limiter combinations for the z and μ coordinates, which will ultimately be used in subsequent model simulations. Unless stated otherwise, all the simulation results presented in this chapter are based on the parameter values given in Table 4.1.

5.2 Validation

5.2.1 Contemporary Models

The model by *Effenberger and Litvinenko* (2014) includes isotropic scattering and a constant adiabatic focusing length. The model compares the diffusion and telegraph approximations in solving the *Roelof* (1969) equation, with the latter approximation being found to be more accurate. Figures 5.1, 5.2, and 5.3 show some examples of the benchmarking studies carried out using the present model. The focusing and no focusing cases mentioned in these figures arise from very small and very large values

of the so-called focusing parameter ξ, which is highly dependent on the focusing length L (*Effenberger and Litvinenko*, 2014). For all the aforementioned figures, the *Roelof* (1969) equation is solved using the numerical scheme discussed in Chapter 4, for transport parameters identical to those used by *Effenberger and Litvinenko* (2014).

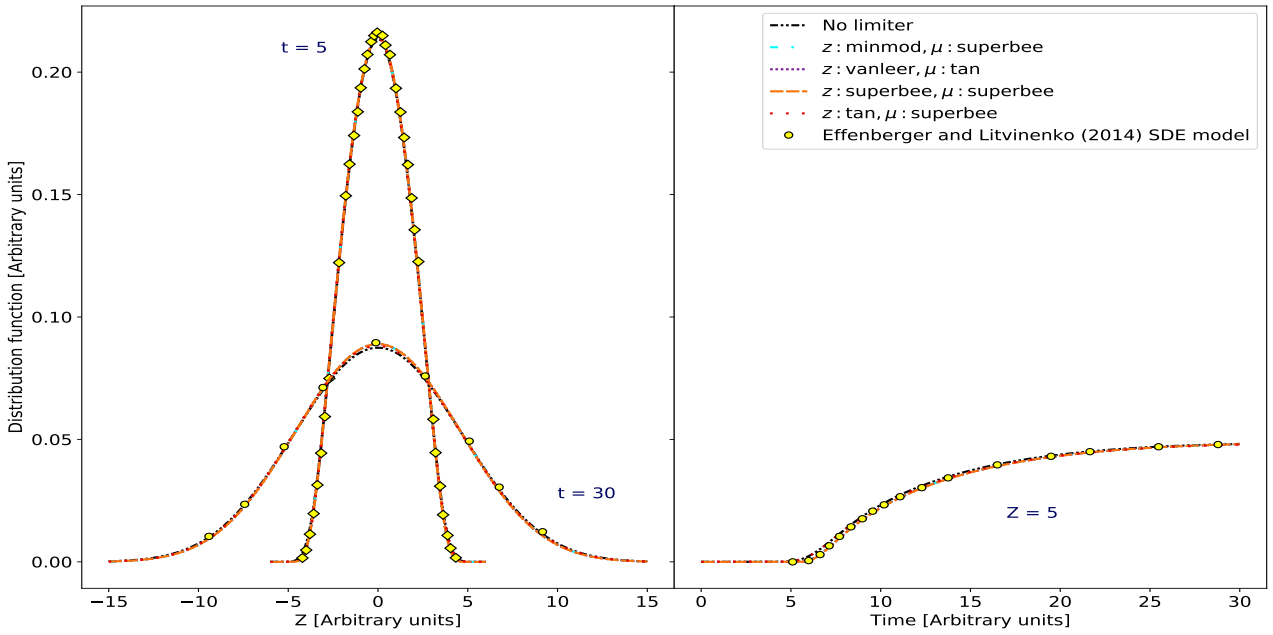

Figure 5.1: *Comparison of the present model, using different flux-limiter combinations for the z and μ coordinates, with the SDE based model of Effenberger and Litvinenko (2014) for the no focusing case.*

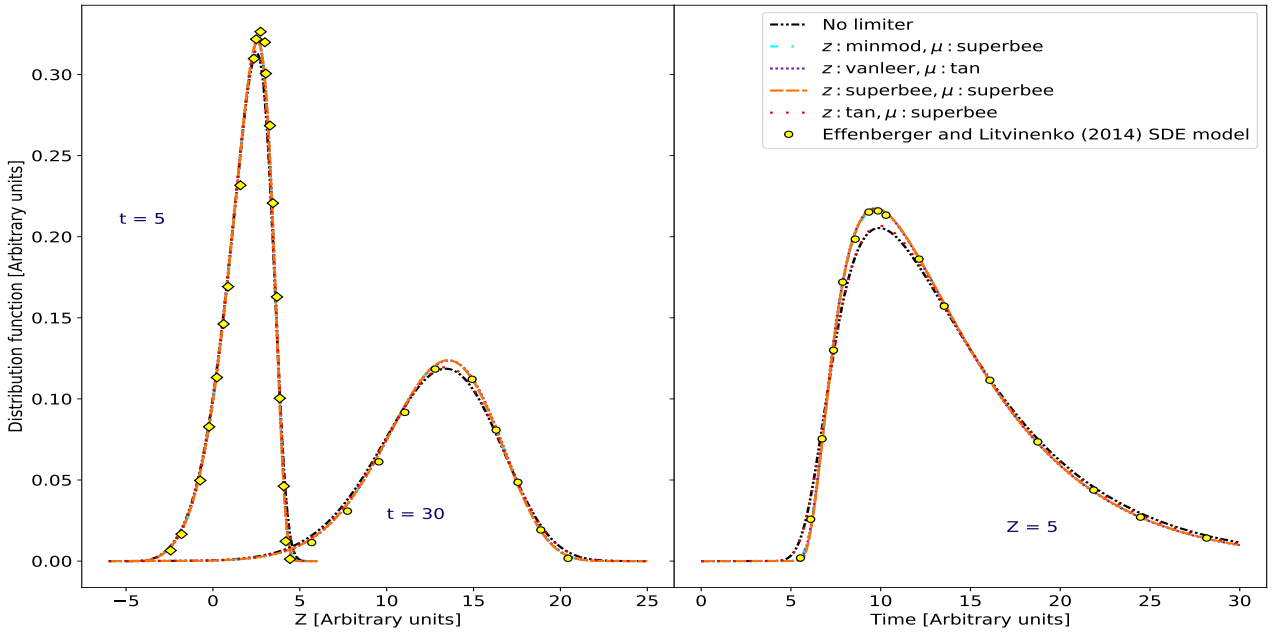

Figure 5.2: *Comparison of the present model, using different flux-limiter combinations for the z and μ coordinates, with the SDE based model of Effenberger and Litvinenko (2014) for the focusing case.*

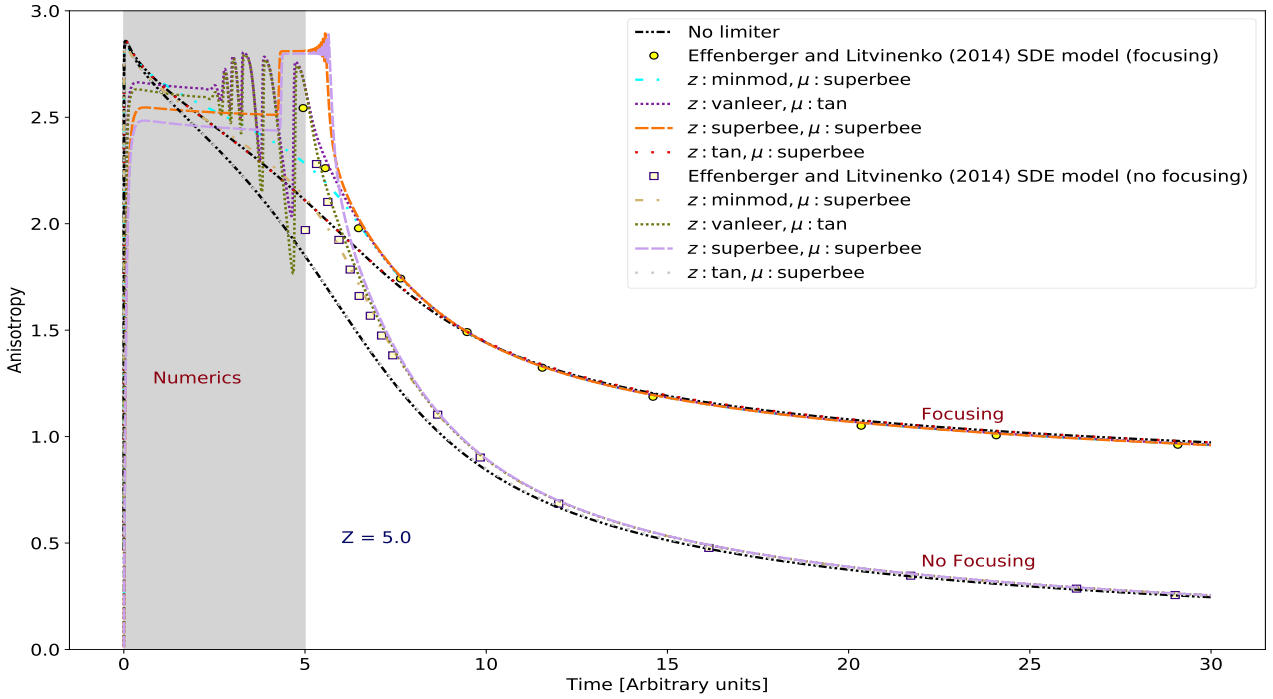

Figure 5.3: *Comparison of the calculated anisotropy profiles to those of Effenberger and Litvinenko (2014), for both the focusing and no focusing cases. A fixed position ($z = 5$) is chosen.*

As seen in Figures 5.1, 5.2, and 5.3 the present model compares well to that of *Effenberger and Litvinenko* (2014), for both focusing and no focusing cases. A relatively small value ($L = 2/3$) is used to signify strong focusing, whereas the no focusing case is implemented by choosing an arbitrarily large value for L, so that the focusing coefficient as given in Equation (4.27) approaches zero. Figure 5.3 emphasizes the physical meaning of both the focusing and no focusing cases, in that the anisotropy for the focusing case is substantially higher compared to that for the no focusing case. Physically, less particles are "swept out" along the magnetic field line in the case of weak or "absent" focusing.

SEPs moving along a path length s (see Figure 4.1), at a speed v, will be detected at the so called onset time $t_{onset} \approx s/v$, marking the right edge of the gray highlighted region in Figures 5.3, 5.4, and 5.5. For $s = s_{\text{Earth}}$ the onset time is ~ 1.8 hours. SEPs are not expected to reach Earth before this time. Therefore, SEP intensities calculated in these highlighted regions are solely due to the numerical calculations (numerics) and do not require a physical interpretation. This behaviour is especially prominent in the anisotropy profiles due to extremely small values of the omni-directional intensity early in the simulation, leading to zero division in calculating the anisotropy. To keep particles out of this area, a small background intensity can be introduced in the model, thus avoiding division by zero. This is done in the next chapter.

Figures 5.4 and 5.5 show further validations of the present model with respect to the finite-difference model of *Strauss and Fichtner* (2015) and the SDE models of *Dröge et al.* (2010) and *van den Berg* (2018). In contrast to the SDE model of *Effenberger and Litvinenko* (2014), these three models have a non-constant focusing length (as governed by a *Parker* (1958) magnetic field), thus making them

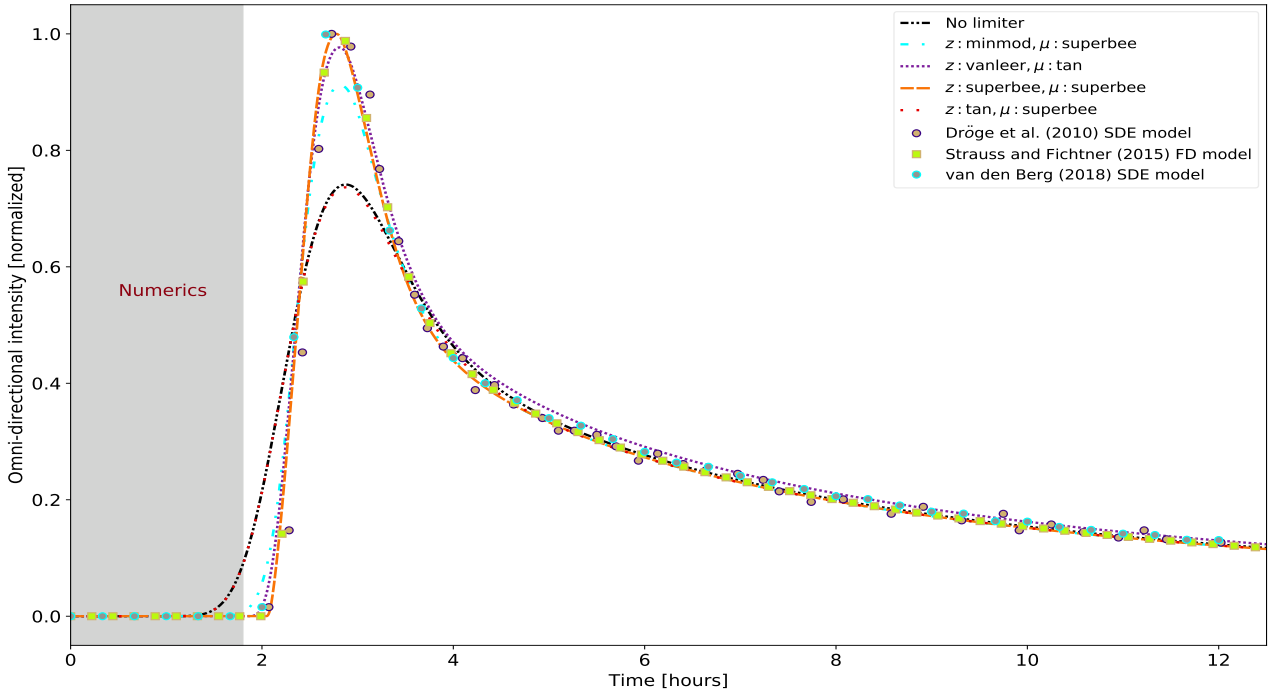

Figure 5.4: *The present model's normalized omni-directional intensity profile for 4 MeV protons, compared to the models by Dröge et al. (2010), Strauss and Fichtner (2015), and van den Berg (2018). Again, various flux-limiter combinations for the z and μ coordinates are used.*

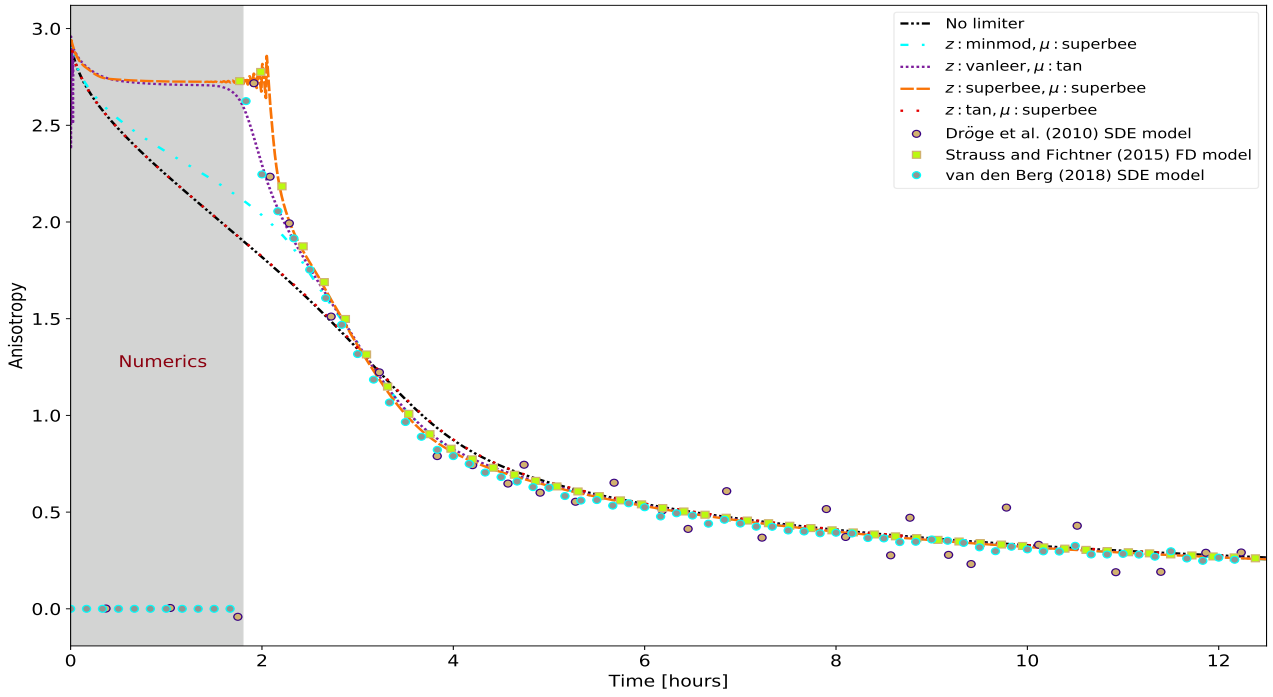

Figure 5.5: *The present model's anisotropy profile for 4 MeV protons compared to those of Dröge et al. (2010), Strauss and Fichtner (2015), and van den Berg (2018). Different flux-limiter combinations are used for the z and μ coordinates.*

more "realistic" to a certain degree. Similar to the current model, these three models also assume a constant solar wind speed, a Parker spiral, a constant radial mean free path λ_{rr}, and solve only for the SEP distribution along a single HMF line. Figure 5.4 shows the omni-directional intensity versus time profile, whereas Figure 5.5 shows the anisotropy versus time profile. An isotropic injection at the Sun is assumed in both cases. Again, the present model compares well with contemporary modelling approaches.

From the comparisons done in this section, a choice of the Superbee limiter for both the z and μ coordinates is inferred as the best flux-limiter combination, with the overall best comparison with respect to the finite-difference and SDE models discussed in this section.

5.3 Model Characteristics

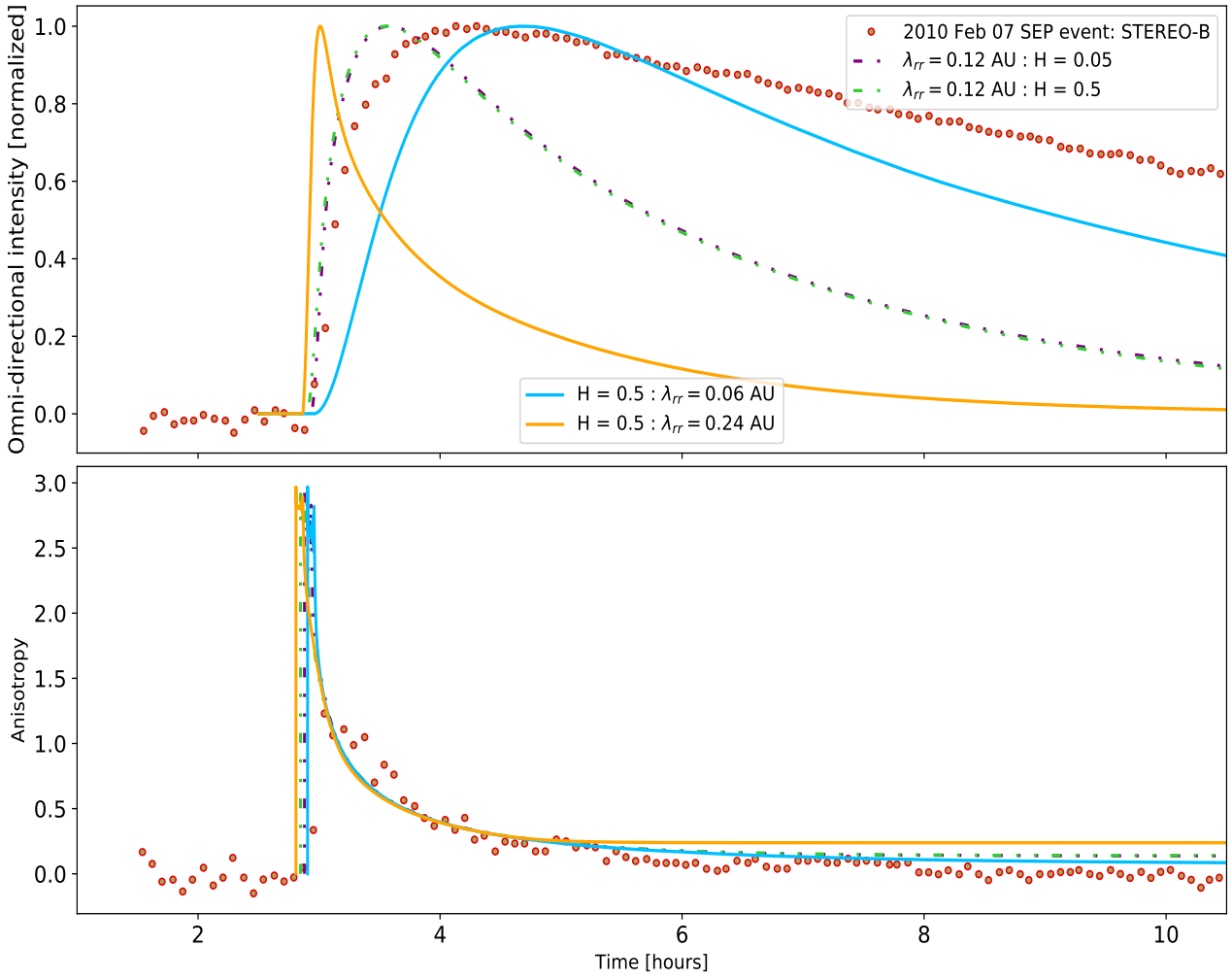

Figure 5.6: *The normalized omni-directional intensity and anisotropy profiles, for 80 keV electrons, compared to the February 07, 2010 SEP event. Parameters used are* $\lambda_{rr} = 0.06, 0.12,$ *and* 0.24 AU, $v_{sw} = 413$ km·s^{-1}, $H = 0.05$ *and* 0.5, *and an outer boundary at* $z = 3$ AU. *Data from Dröge et al. (2014).*

In this section, results calculated using the present model are compared to a solar electron event observed by STEREO-B for 80 keV electrons on 7 February 2010 (see e.g., *Dröge et al.*, 2014). It is worth noting that this section does not seek to provide a best fit to the observations, but rather give insight into the attributes of the model. To achieve this, the radial mean free path λ_{rr} and the parameter H are varied.

For the first case, the radial mean free path value of $\lambda_{rr} = 0.12$ AU is kept constant, and the parameter H varied between it's minimum and maximum values of 0.05 and 0.5, respectively. In the second case, the parameter $H = 0.5$ is now kept constant, and the radial mean free path varied between $\lambda_{rr} = 0.06$ and 0.24 AU, signifying strong and weak scattering.

In Figure 5.6, one can see that different values of the parameter H lead to very small changes in the corresponding omni-directional intensity (dash-dot-dotted lines in the top panel), and anisotropy (dash-dot-dotted lines in the bottom panel) temporal profiles. Variations in the radial mean free path, however, lead to distinct omni-directional intensity temporal profiles (solid lines in the top panel), and, to a lesser degree, anisotropy temporal profiles (solid lines in the bottom panel). A key feature, observed in the top panel, is the relatively faster intensity increases for $\lambda_{rr} = 0.24$ AU, as opposed to the gradual increases of $\lambda_{rr} = 0.06$, and 0.12 AU. These can be attributed to the lower degree of scattering associated with large radial mean free path values. The latter effect is investigated in more detail in Chapter 6.

5.4 Summary

This chapter served to provide a validation of the numerics of the present model, comparing simulation results with those of existing models and an electron SEP event. Different flux-limiter combinations were used for the z and μ coordinates, with the goal of determining the combination that agrees best with the other models. Overall it was found that the present model compares well with respect to the other models.

For the *Effenberger and Litvinenko* (2014) comparison, it was found that a choice of the Superbee limiter for both the z and μ coordinates gives the best fit (see Figures 5.1, 5.2, and 5.3), due to it's aggressiveness in reconstructing gradients (see Section 3.8.2). This Superbee - Superbee trend was found to continue with respect to the even more "realistic" models by *Dröge et al.* (2010), *Strauss and Fichtner* (2015), and *van den Berg* (2018). In addition, the present model's good agreement with the SDE simulation results vindicates the numerical approach discussed in Chapter 4, due to the fact that SDE models conserve particles by construction (*Strauss and Fichtner*, 2015).

It is worth noting that the van Leer and Tan limiter combination for the respective z and μ coordinates also provide reasonably good comparisons when compared to the other combinations. Subsequently, the Superbee - Superbee combination will be used for all model runs.

CHAPTER 6

Modelling Solar Energetic Particle Transport along the Hohmann Transfer Orbit

6.1 Introduction

Recent interest by NASA and SpaceX in interplanetary space missions has catapulted the study of SEPs to the forefront of space physics and space weather research due to the significant danger they pose to future space missions (*Hu et al.*, 2009). To date, the most energy-efficient means of transferring between two planetary orbits is the Hohmann transfer orbit (*Hohmann*, 1925). In order to study SEP transport along these transfer orbits, the question arises as to whether there is an SEP magnetic "highway" between the respective planetary orbits (Earth and Mars in this study) along which the charged particles can propagate very effectively.

In this chapter, the Hohmann-Parker effect (*Posner et al.*, 2013) shall be discussed in answering this question. In addition, model solutions, as observed by "virtual" spacecraft at various distances along the Hohmann transfer orbit for different parameters, will be provided. Following on from these simulation results, the spatial dependence of the peak intensities and anisotropies will be examined. Functional forms $I_{\max}(z) = z^{-\alpha}$ and $A_{\max}(z) = z^{-\beta}$ will be fitted to the simulated intensity and anisotropy profiles. The spatial dependence of the time of maximum $T_{\max}(z)$ will also be investigated. The latter is expected to provide insight into particle scattering. The chapter will conclude by considering the idea of a "warning time" of an SEP event for a future manned space mission to Mars along the Hohmann minimum-energy transfer orbit. It is worth noting that energetic protons are harmful to astronauts (due to their larger momentum), whereas energetic electrons mostly affect spacecraft components (*Kubo et al.*, 2015).

6.2 The Hohmann-Parker Effect

6.2.1 Defining The Hohmann-Parker Effect

The Hohmann transfer orbit (*Hohmann*, 1925) has been the go-to method for all lunar and interplanetary space travel for the past few decades. It involves accelerating a spacecraft onto an elliptical orbit such that its perihelion is at the inner planet and the aphelion at the outer planet's orbit (*Posner et al.*, 2013). Figure 6.1 shows a recent application of the Hohmann transfer (gray dotted line) to the Mars Science Laboratory (MSL) mission to Mars, which took approximately 8.5 months.

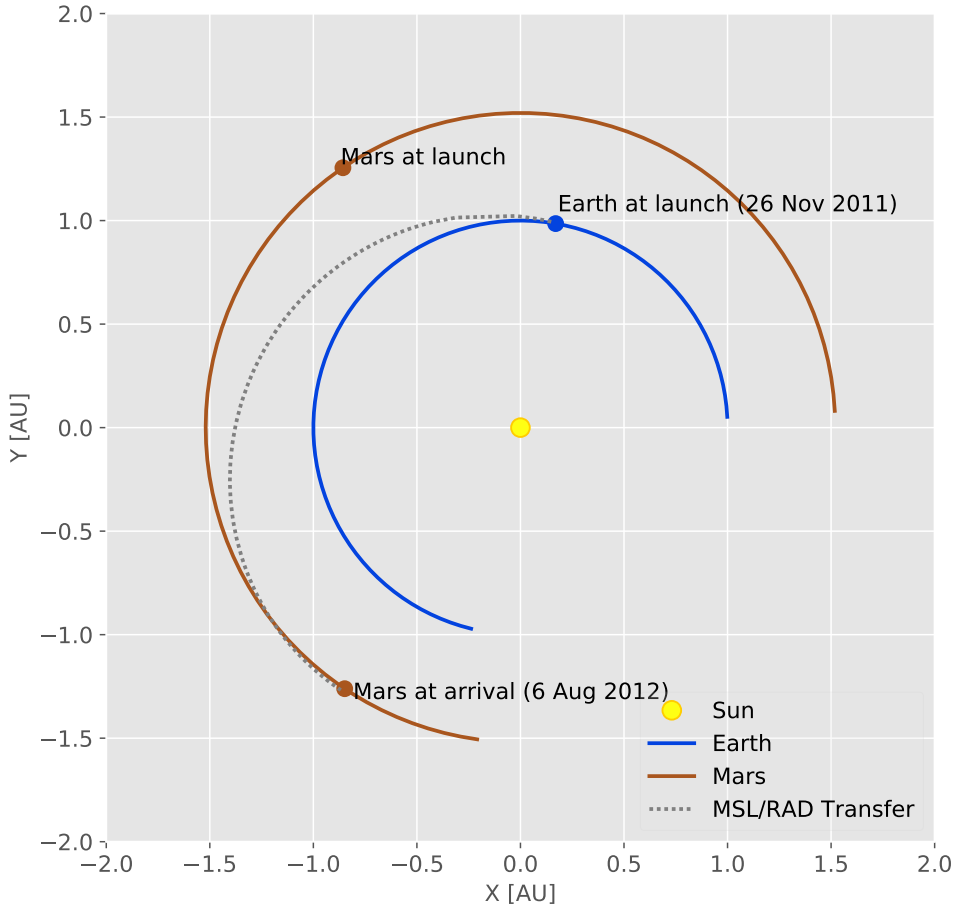

Figure 6.1: *The Hohmann transfer trajectory of the Mars Science Laboratory (MSL) mission to Mars from its launch on the 26 November 2011 until its arrival at Mars approximately 258 days later. The circular orbits of Earth and Mars are also shown in the figure. Data provided by Guo (2018).*

The Hohmann-Parker effect is based on findings by *Posner et al.* (2013). With the assumption of simple orbital analyses and idealized solar wind conditions, the authors found that a spacecraft performing a Hohmann transfer between two planets in the inner solar system retains a small angular

magnetic connection distance to either planet during different phases of the transfer. The magnetic connection distance is defined as the longitudinal angular distance between two position's magnetic field lines, connecting them to the source surface of the Sun. In addition, the authors further found that the rather small orbital inclinations of the inner solar system planets with respect to the Laplace invariable plane result in very small latitudinal magnetic connection distances for these planets. This finding fits well into the present modelling approach due to it being constrained to the ecliptic regions.

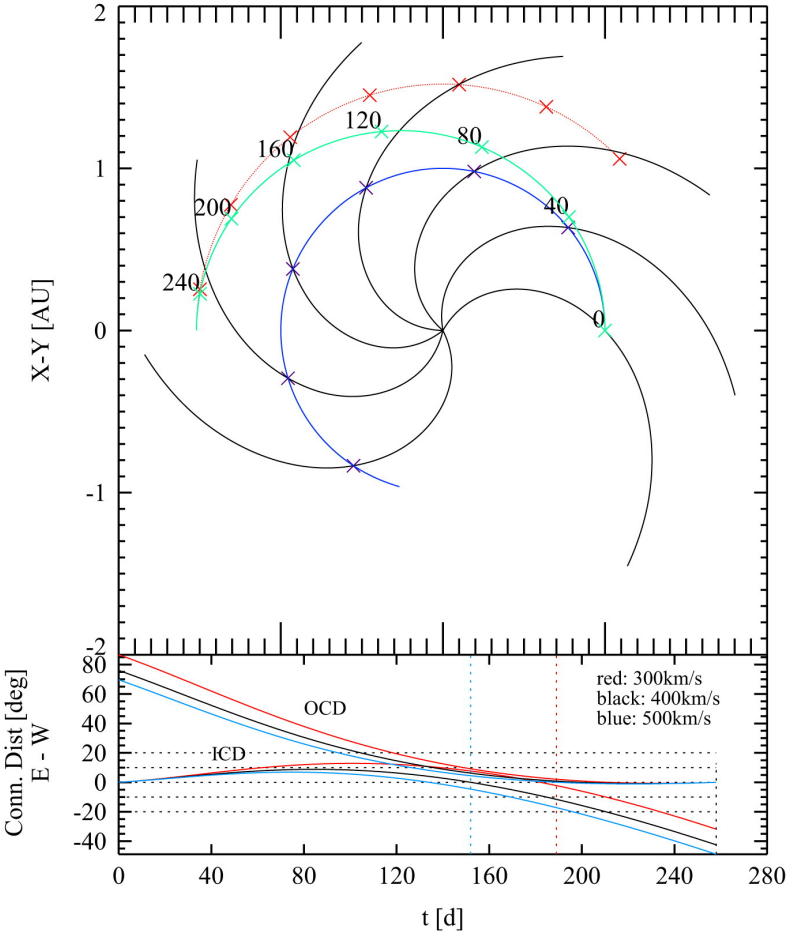

Figure 6.2: *A Hohmann transfer orbit between Earth and Mars. The transfer orbit is shown as the green line in the top panel, along with the orbits of Earth and Mars, shown in blue and red, respectively. Parker HMF spirals for a* 400 km·s^{-1} *solar wind are also shown. The crosses on the different orbits denote 40 day time intervals. The inner and outer connection distances for three different solar wind speeds are shown in the bottom panel. Figure taken from Posner et al. (2013).*

The magnetic connection distance is divided into an inner and outer connection distance, respectively ICD and OCD (see the bottom panel of Figure 6.2) (*Posner et al.*, 2013). These connection distances refer to the longitudinal angular distance between the magnetic field lines of the inner and outer planet from the spacecraft. Thus, a spacecraft transferring from Earth to Mars via the Hohmann transfer trajectory will initially have a small ICD with the Earth, and with time this ICD will increase considerably. From Figure 6.2 it can be seen that the ICD reaches a maximum of $\sim 10 - 15°$ around

day 80 for a below-average solar wind speed of 300 km·s^{-1}. The period from approximately day $80-190$ sees a decrease in the ICD for the different solar wind speeds. In the late phase of the journey (day $200-240$) the ICD begins to exceed $\sim 10°$ for the slow solar wind speed with the ICDs for the 400 and 500 km·s^{-1} solar wind speeds having exceeded the 10° mark much earlier.

The OCD starts out at $\sim 90°$, but by day $150-190$ (marked by the vertical blue and red dashed lines in the bottom panel of Figure 6.2) the OCDs reach values smaller than the ICDs for the respective solar wind speeds, defining the "handshake" time period (*Posner et al.*, 2013). This time period denotes the "handover" of the magnetic connection from Earth-Spacecraft over to Spacecraft-Mars.

To summarize, *Posner et al.* (2013) show that the combined magnetic field connections keep the spacecraft within 13° of angular distance from either Earth (during the initial phase of the transfer) or Mars (in the late phase of the transfer orbit).

6.2.2 Scientific Implications

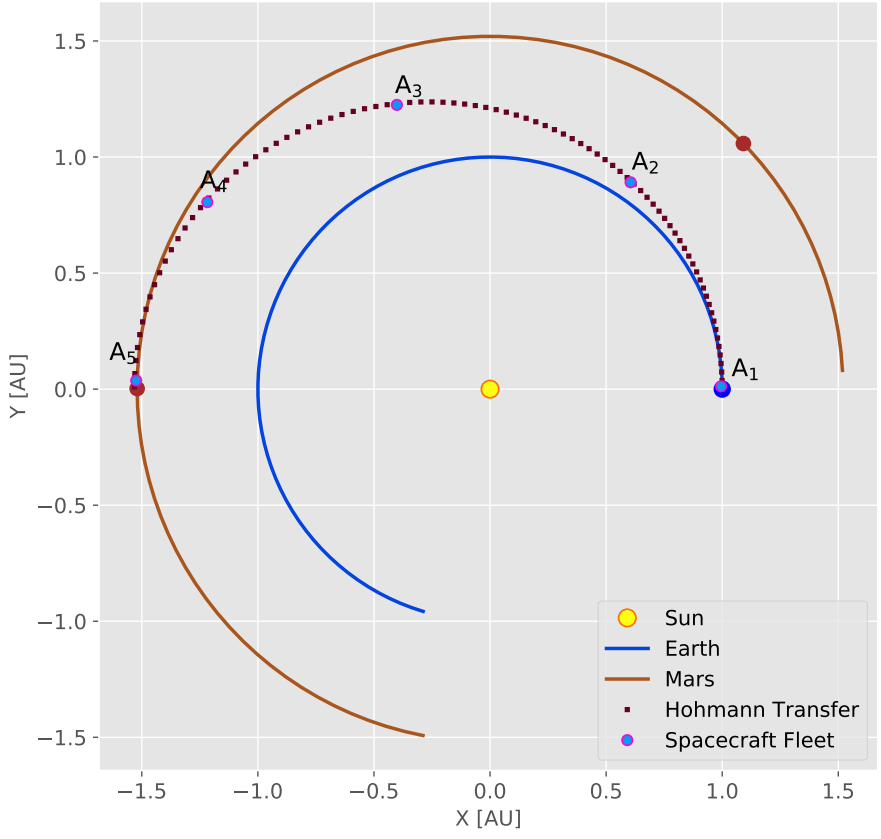

Figure 6.3: *The position of a spacecraft fleet along an arbitrarily chosen Hohmann transfer trajectory. The labels* $A_i (i = 1, 2, 3, 4, 5)$ *correspond to the distances along the field line* z *of* $1.18, 137, 1.58, 1.80,$ *and* 2.04 AU *respectively. The circular orbits of Earth and Mars are also shown in the figure.*

A key consequence of the Hohmann-Parker effect (especially to the present study) is that a spacecraft performing a Hohmann transfer orbit, and the planet with which it has the smallest magnetic

connection distance, are anticipated to experience correlated SEP conditions assuming a quasi-steady heliosphere (*Posner et al.*, 2013). This makes a 1D modelling approach as presented in this study viable to simulate SEP propagation along this magnetic "highway".

Motivated by the findings of *Posner et al.* (2013) and the subsequent implications, Figure 6.3 shows a "virtual" spacecraft fleet positioned along the Hohmann transfer trajectory at varying distances of 1.18, 1.37, 1.58, 1.80, and 2.04 AU. Simulations of SEP intensities and anisotropies for these spacecraft are presented below.

6.3 Modelling Results

In this section, the simulation results of SEP intensity and anisotropy temporal profiles for 4 and 32 MeV protons as observed by the spacecraft fleet described in Section 6.2.2 will be presented. Moreover, different values of the radial mean free path λ_{rr}, ranging from $0.25 - 0.35$ AU, will be employed. The latter will be used primarily to test the dependence of the simulation results on the assumed radial mean free path.

Figure 6.4 shows the intensity-time profiles of 4 MeV protons observed along the Hohmann transfer orbit (as shown in Figure 6.3), whereas Figure 6.5 shows the corresponding anisotropy-time profiles. In both Figures 6.4 and 6.5, a radial mean free path $\lambda_{rr} = 0.25$ AU (corresponding to a parallel mean free path $\lambda_{\parallel} \approx 0.5$ AU at Earth's position) is used. Furthermore, the different color curves in both figures denote the intensity and anisotropy-time profiles observed at distances of 1.18, 137, 1.58, 1.80, and 2.04 AU. As expected, it can be seen in Figure 6.4 that the SEP intensity falls off with increasing distance along the Hohmann transfer orbit, so that the spacecraft at Earth (A_1) detects a much higher SEP intensity than that observed at Mars (A_5). The open circles in Figures 6.4 and 6.5 denote the peak intensities and anisotropies of the simulation results.

Similarly, Figures 6.6 and 6.7 again show the intensity and anisotropy-time profiles for 4 MeV protons. However, in this case, a relatively larger value of the radial mean free path $\lambda_{rr} = 0.30$ AU (corresponding to a parallel mean free path $\lambda_{\parallel} \approx 0.6$ AU at Earth's position) is assumed. It is clear from Figures 6.4 and 6.6 that increasing values of λ_{rr} lead to higher peak intensities in the corresponding SEP cases, with no clearly discernible differences in the anisotropy-time profiles shown in Figures 6.5 and 6.7. In a later section, these observations shall be investigated in greater detail. Again, the open circles in both figures denote the peak intensities and anisotropies of the simulation results.

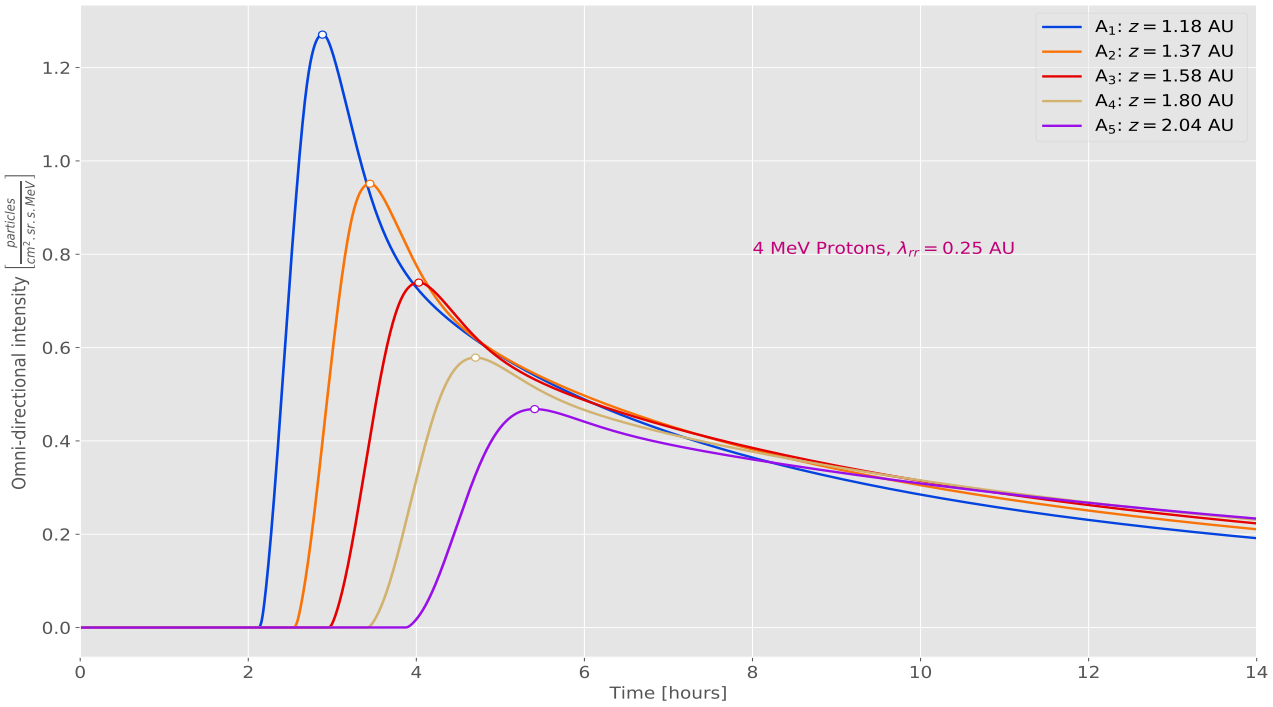

Figure 6.4: *Simulation results of intensity-time profiles of 4 MeV protons with a radial mean free path of* $\lambda_{rr} = 0.25$ AU*, observed along the Hohmann transfer orbit. The different color curves indicate the intensity-time profiles observed at distances of* $1.18, 137, 1.58, 1.80,$ *and* 2.04 AU*.*

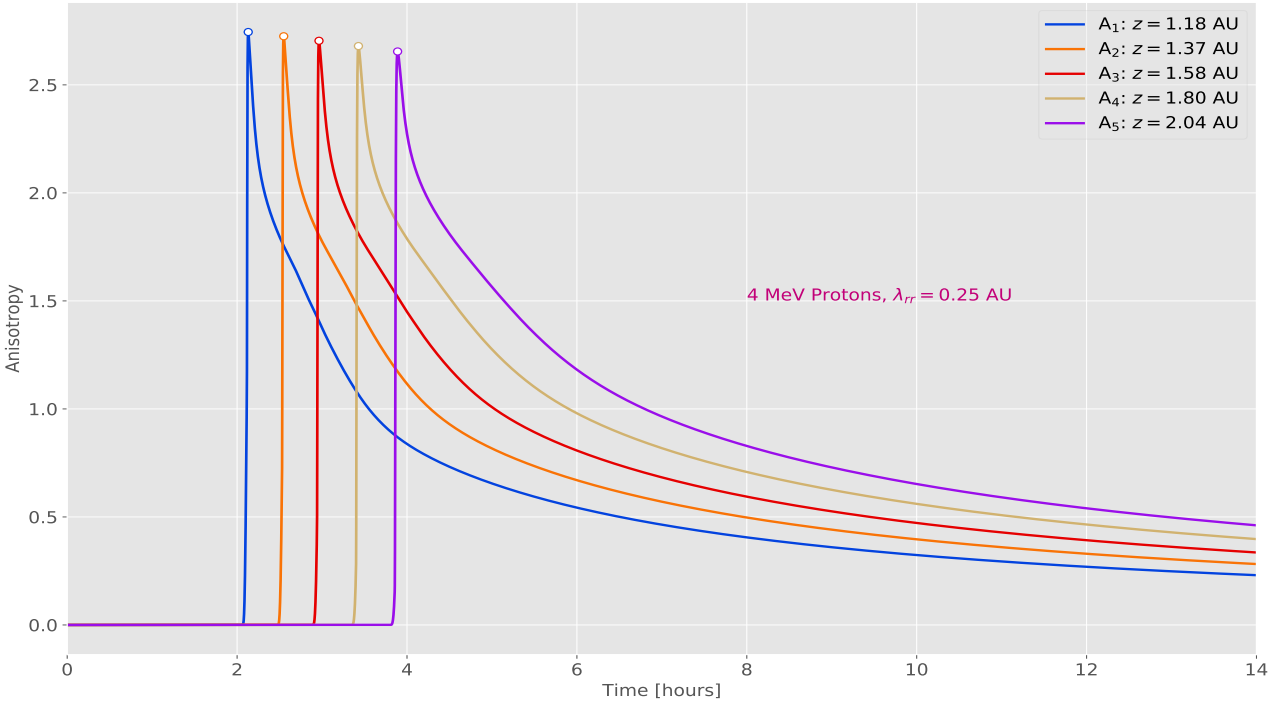

Figure 6.5: *The anisotropy-time profiles corresponding to the intensity-time profiles shown in Figure 6.4.*

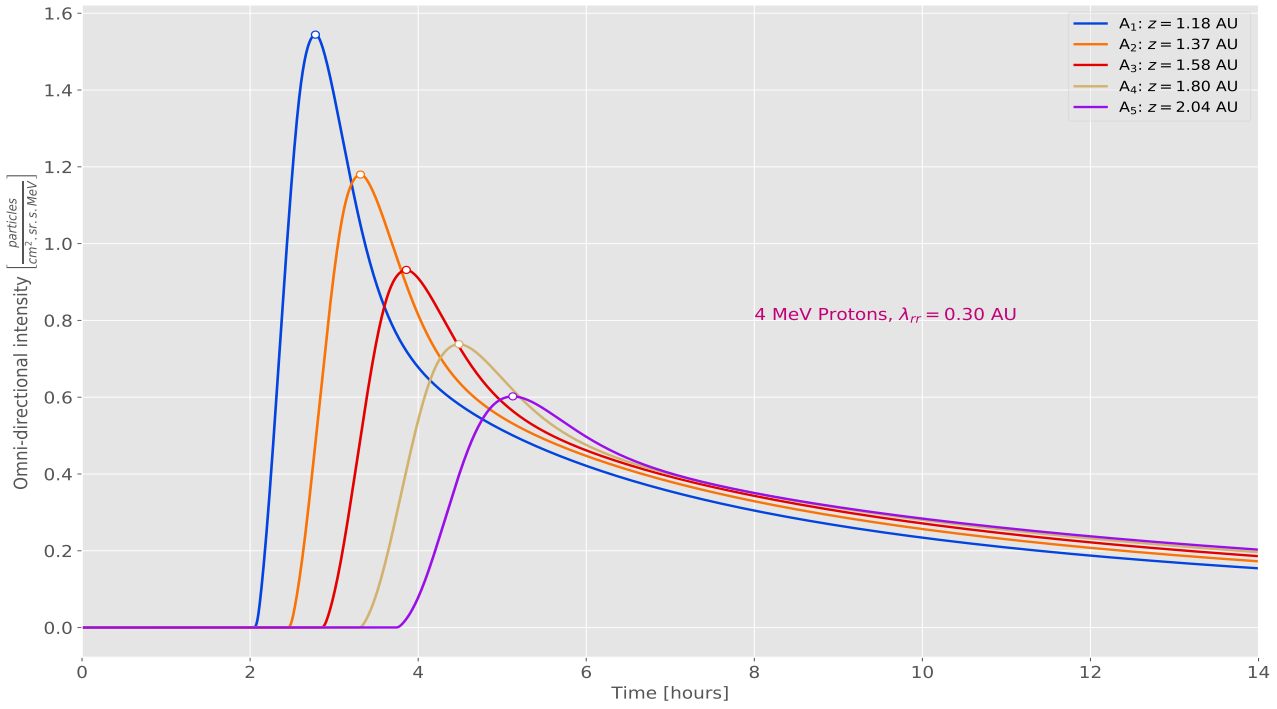

Figure 6.6: *Similar intensity-time profiles as shown in Figure 6.4, but now a radial mean free path of* $\lambda_{rr} = 0.30$ AU *is used.*

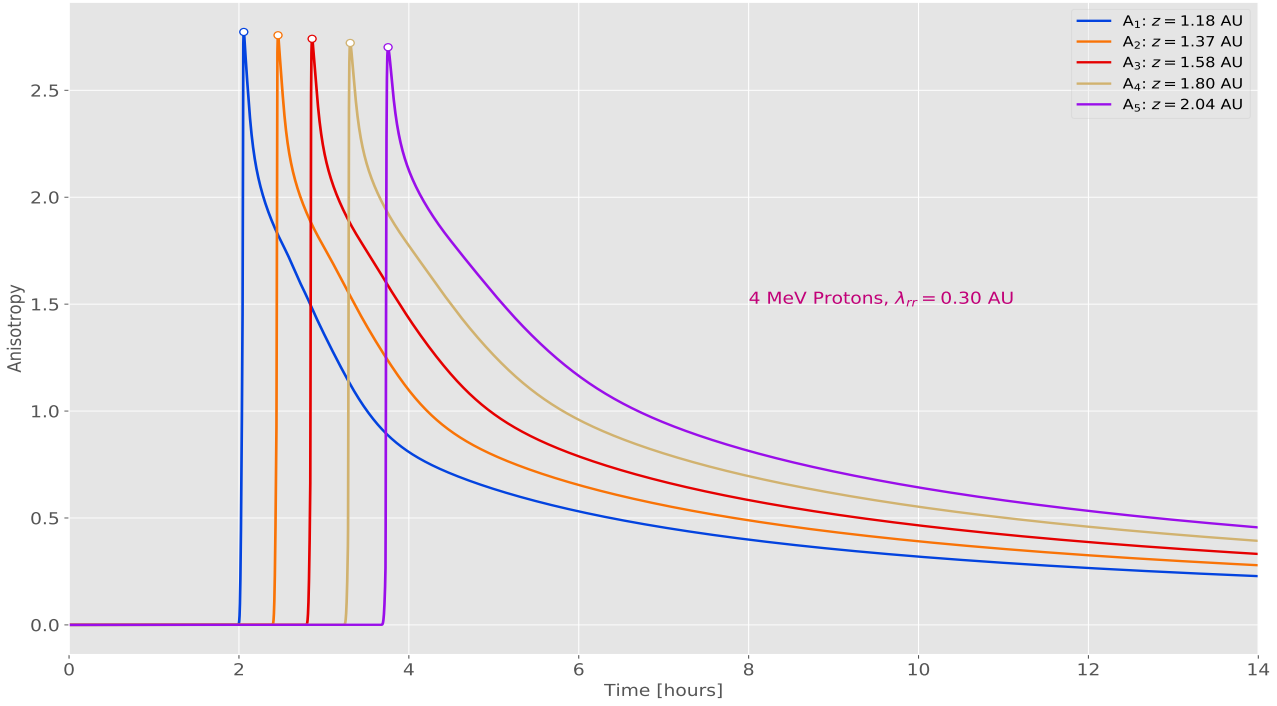

Figure 6.7: *The anisotropy-time profiles corresponding to the intensity-time profiles shown in Figure 6.6.*

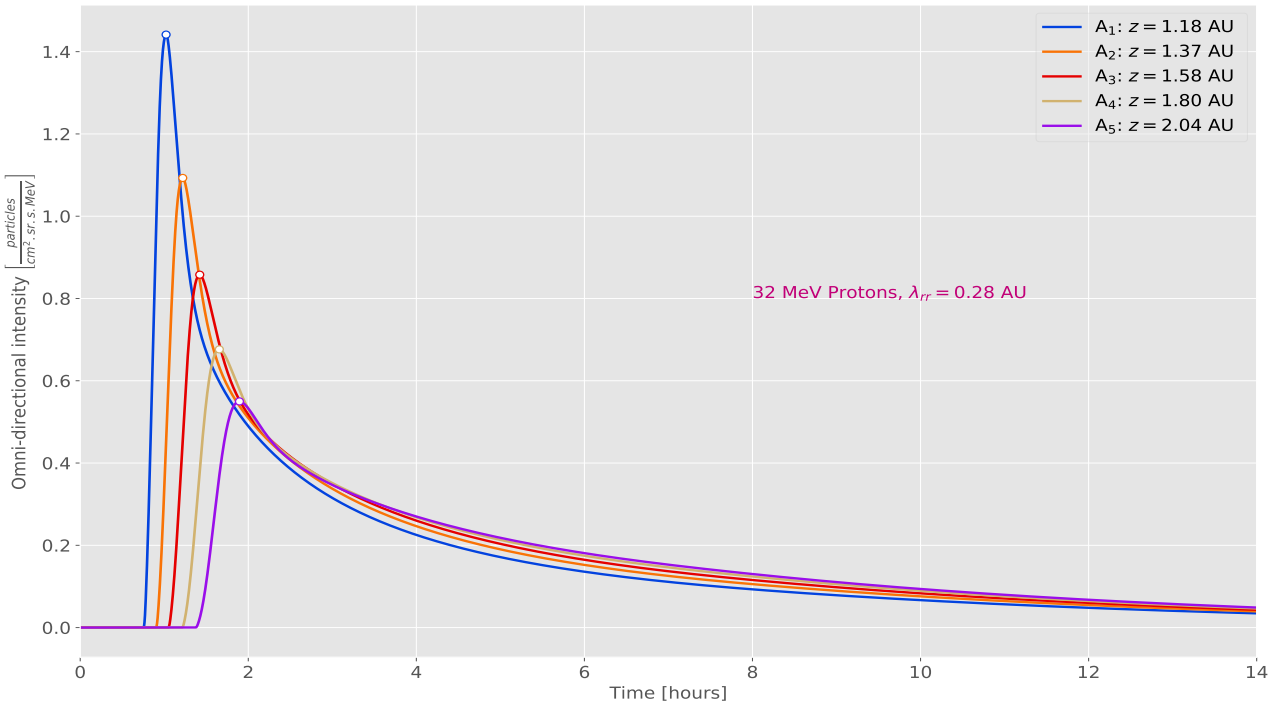

Figure 6.8: *Simulation results of intensity-time profiles of 32 MeV protons, assuming a radial mean free path of* $\lambda_{rr} = 0.28$ AU*, observed along the Hohmann transfer orbit. The different color curves indicate the intensity-time profiles observed at distances of* $1.18, 137, 1.58, 1.80,$ *and* 2.04 AU*.*

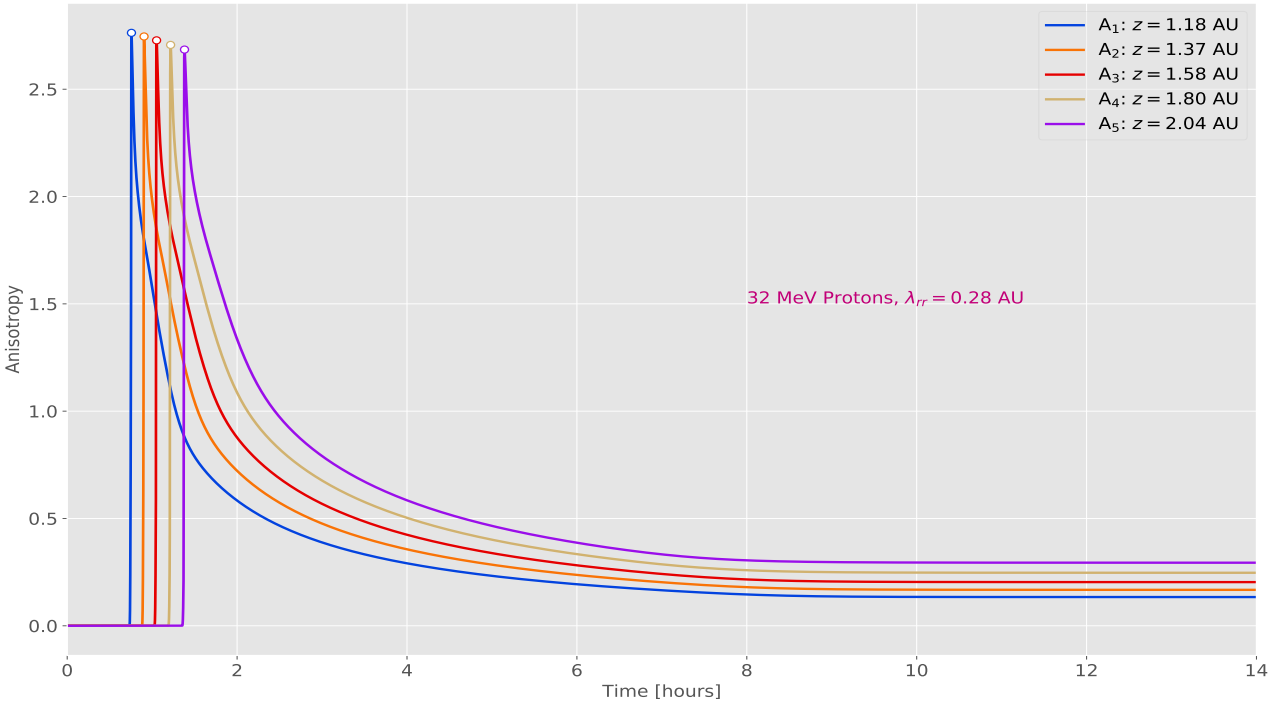

Figure 6.9: *The anisotropy-time profiles corresponding to the intensity-time profiles shown in Figure 6.8.*

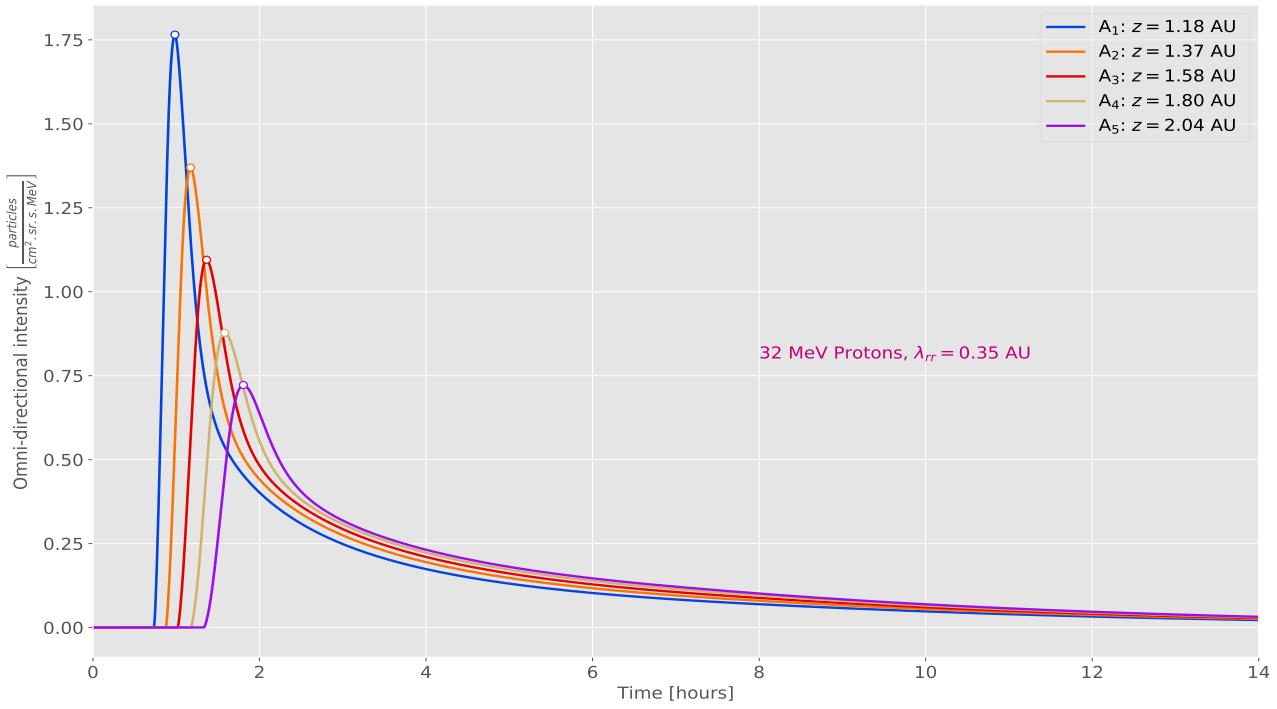

Figure 6.10: *Similar intensity-time profiles as shown in Figure 6.8, but now a radial mean free path of* $\lambda_{rr} = 0.35$ AU *is used.*

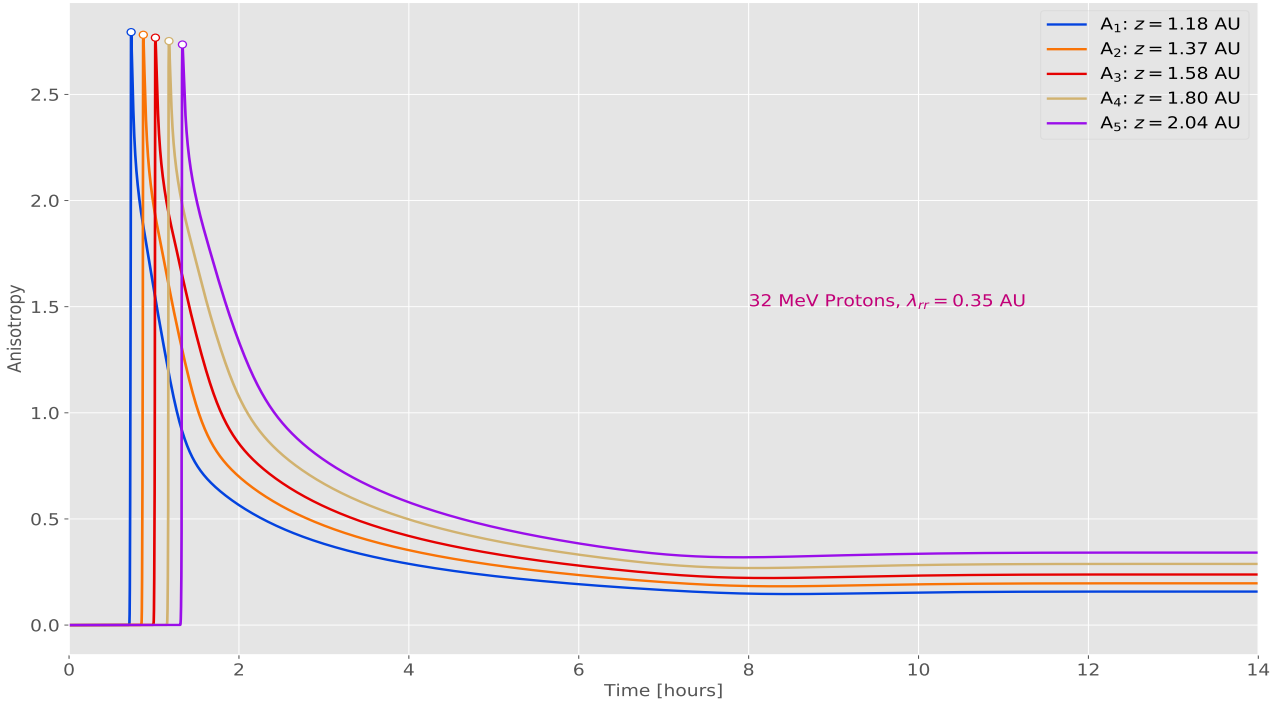

Figure 6.11: *The anisotropy-time profiles corresponding to the intensity-time profiles shown in Figure 6.10.*

Moving on to a higher energy, Figure 6.8 shows the intensity-time profiles of 32 MeV protons, assuming a radial mean free path of $\lambda_{rr} = 0.28$ AU (corresponding to a parallel mean free path of $\lambda_{\parallel} \approx 0.56$ AU

at Earth). Figure 6.9 shows the corresponding anisotropy-time profiles. Similar to Figures 6.4 and 6.6, Figure 6.8 also shows that the SEP intensity decreases with increasing distance. It is worth noting the relatively smaller onset times in Figures 6.8 and 6.9, in contrast with those shown in Figures 6.4, 6.5, 6.6, and 6.7. This is mainly attributed to the significantly higher proton particle energy of 32 MeV, which corresponds to a particle speed $v \approx 1.83$ AU·h^{-1}, as opposed to $v \approx 0.66$ AU·h^{-1} for 4 MeV protons. Once more, the open circles in both figures denote the peak intensities and anisotropies of the simulation results.

Figures 6.10 and 6.11 again show the intensity and anisotropy-time profiles for 32 MeV protons, assuming a larger radial mean free path of $\lambda_{rr} = 0.35$ AU (corresponding to a parallel mean free path of $\lambda_{\parallel} \approx 0.7$ AU at Earth). Similarly, the open circles denote the peak intensities and anisotropies of the simulation results. Furthermore, as for the 4 MeV proton simulations, an increase in λ_{rr} leads to higher peak intensities with no significant differences in the corresponding peak anisotropies.

An interesting feature observed in all the intensity-time profiles (Figures 6.4, 6.6, 6.8, and 6.10) is that there is a convergence of particle intensities during the late phase of the SEP events, defining the SEP reservoir phenomenon described by *Reames* (2013). The SEP intensity in this reservoir is also characterized by a nearly isotropic particle distribution

6.4 Spatial Dependence

6.4.1 Peak Intensities and Anisotropies

To better quantify the potential radiation risk posed by SEPs, various studies (see e.g., *McGuire et al.*, 1983; *Hamilton et al.*, 1990) have investigated the spatial dependence of SEP peak intensities and fluences. Their investigation involved using a functional form $I_{\max}(r) = kr^{-\alpha}$, with k being some constant, r the radial distance of the spacecraft, and α a power-law index, in modelling the spatial dependence of peak intensities. A recent study by *He et al.* (2017), however, opted for a different approach. Instead of using this functional form from the onset, these authors numerically solve a five-dimensional Fokker-Planck equation, from which they obtain the spatial dependence of the SEP peak intensities by quantitatively determining the index α. Their model incorporates perpendicular diffusion, two spacecraft fleet orientations, with one along the radial direction, and the other along a *Parker* (1958) magnetic field line, and considers heliocentric distances of 0.25 to 1.0 AU.

He et al. (2017) found that the peak particle intensities in the SEP events decrease almost in a power-law fashion with increasing distance. In addition, they also found that the index α is not strongly dependent on particle energy, the width of the SEP sources, or the ratios of relatively reasonable values of the perpendicular and parallel mean free paths, but rather depends more on physical properties such as the location of the SEP sources and the magnetic connection between the observer and the SEP source.

Inspired by the study of *He et al.* (2017), the current study aims to investigate the spatial dependence of SEP peak intensities along the Hohmann transfer orbit (*Hohmann*, 1925). It is worth noting that the major differences between the present study and that of *He et al.* (2017) are that their model solves a five-dimensional Fokker-Planck equation, and includes most (if not all) SEP transport mechanisms. The present model, on the other hand, solves the 1D *Roelof* (1969) equation, and includes three SEP transport mechanisms (see Section 4.2).

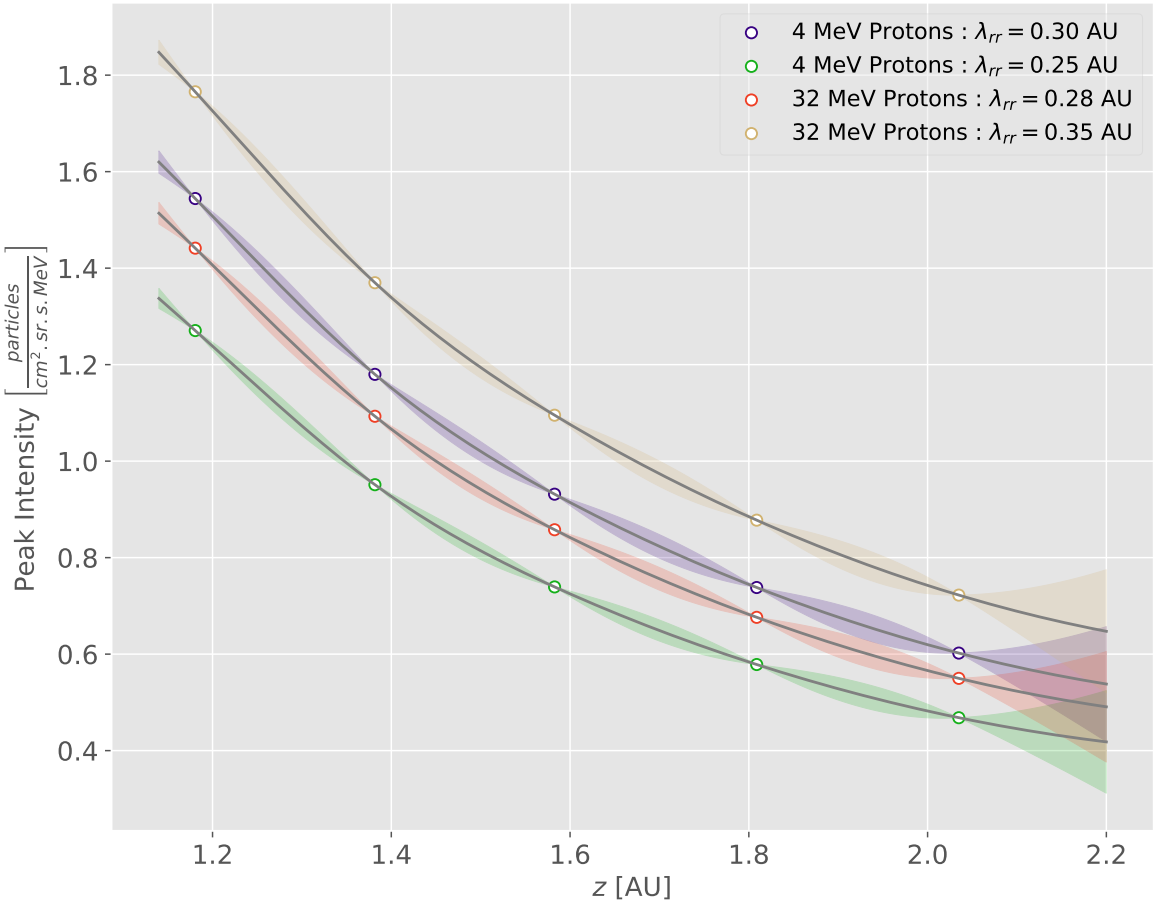

Figure 6.12: *Distribution of SEP peak intensities extracted from Figures 6.4 (green), 6.6 (indigo), 6.8 (tomato), and 6.10 (tan), as a function of spatial distance z. The open circles denote the peak intensities of the SEP events observed along the Hohmann transfer orbit. The corresponding lighter filled regions represent the respective errors.*

To accomplish this, the peak intensities (denoted by the open circles) and their corresponding spatial distances are extracted from Figures 6.4 (green), 6.6 (indigo), 6.8 (tomato), and 6.10 (tan). These results are combined in Figure 6.12. The lighter filled regions denote the continuous errors as obtained by the use of a gaussian process regression (GPR), which is used in probability theory and statistics in providing a continuous measure of the uncertainty (see e.g., *Mackay*, 2003).

Unlike *He et al.* (2017), the present study also examines the spatial dependence of the peak anisotropies. Figure 6.13 shows the peak anisotropies (corresponding to Figure 6.12) extracted from Figures 6.5 (green), 6.7 (indigo), 6.9 (tomato), and 6.11 (tan). The open circles denote the peak anisotropies of

the SEP events observed along the Hohmann transfer orbit. Again the lighter filled regions denote the continuous errors obtained via GPR. It is worth noting their relatively smaller sizes in comparison to the peak intensity continuous errors shown in Figure 6.12.

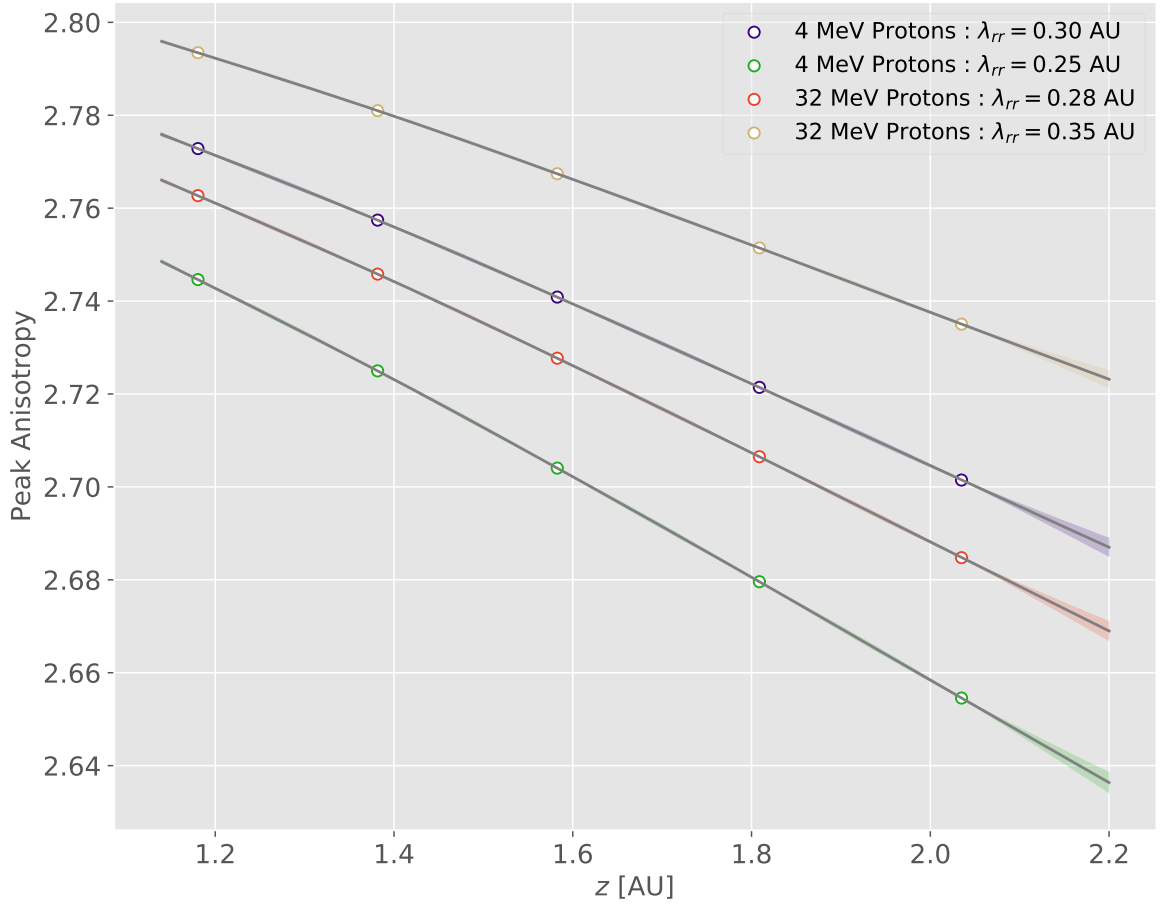

Figure 6.13: *Distribution of SEP peak anisotropies corresponding to the peak intensities shown in Figure 6.12, as a function of spatial distance z. The open circles denote the peak anisotropies of the SEP events observed along the Hohmann transfer orbit. The corresponding lighter filled regions (although minor) represent the respective errors.*

6.4.2 Functional Forms

In order to obtain the functional forms of the peak intensities and anisotropies, $I_{\max}(z) = z^{-\alpha}$ and $A_{\max}(z) = z^{-\beta}$, a best fit/regression line is calculated for the different SEP cases shown in both Figures 6.12 and 6.13. This allows the power-law indices α and β to be determined for each of the SEP event scenarios. Figures 6.14 and 6.15 show the corresponding power-law spatial dependences of the SEP peak intensities and anisotropies, respectively. The respective functional forms $z^{-\alpha}$ and $z^{-\beta}$ along with the different values of α and β are also included in the figures.

In Figure 6.14, the various functional forms $I_{\max} = z^{-\alpha}$ for the four different SEP event scenarios along the Hohmann transfer orbit are shown. This figure reinforces the earlier observed (see Section

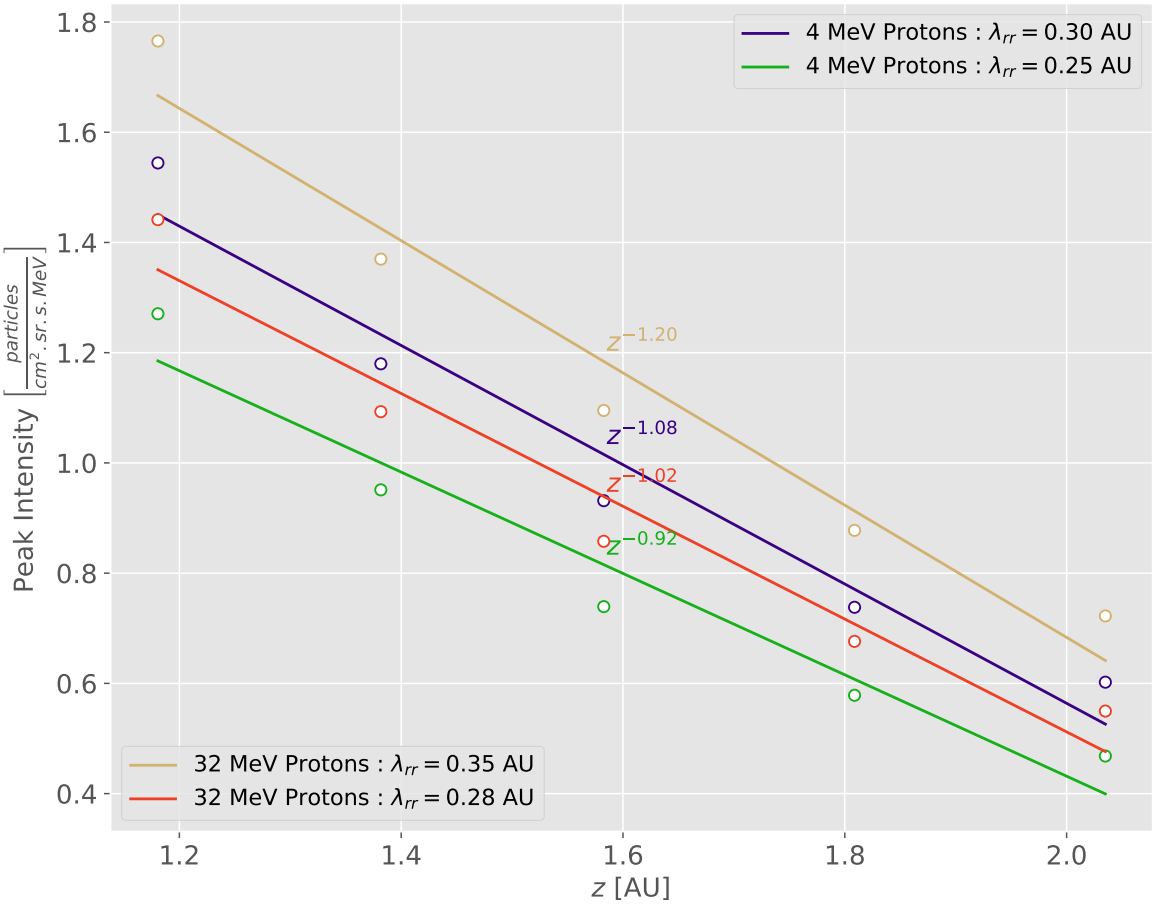

Figure 6.14: *Similar to Figure 6.12, except in this case, the power-law spatial dependence of the SEP peak intensities is shown. The functional form $z^{-\alpha}$ with varying values of α, denoting the simulation results of the different SEP cases is also included.*

6.3) peak intensities power-law decrease with increasing spatial distance. Interestingly, the reservoir phenomenon (*Reames*, 2013) is seen in this figure via the observable convergence of the peak intensities with increasing spatial distance z. The values of α are found to be roughly in the range $[0.92, 1.20]$, with a median value of 1.06. Thus the average peak intensity functional form is found to be approximately $z^{-1.06}$.

Particle intensities within the inner heliosphere are mostly affected by the mean free path, details of particle injection, and focusing effects (see e.g., *Lario et al.*, 2007). In this study, the radial mean free path λ_{rr} is varied, and thus from Figure 6.14 it can be seen that smaller λ_{rr} values lead to a slower decrease of the peak intensities (i.e. a smaller positive value of α) with spatial distance. This finding is not in agreement with *Lario et al.* (2007), who find the opposite in that a smaller mean free path leads to a steeper peak intensity decrease. Taking the average of the power-law indices of the 4 and 32 MeV protons, it is found that $\alpha = 1.0$ and $\alpha = 1.11$, respectively. Thus it is safe to conclude that, on average particles with higher energies have a faster peak intensity decrease (i.e. a larger positive value of α) with spatial distance, in comparison to the less-energetic particles.

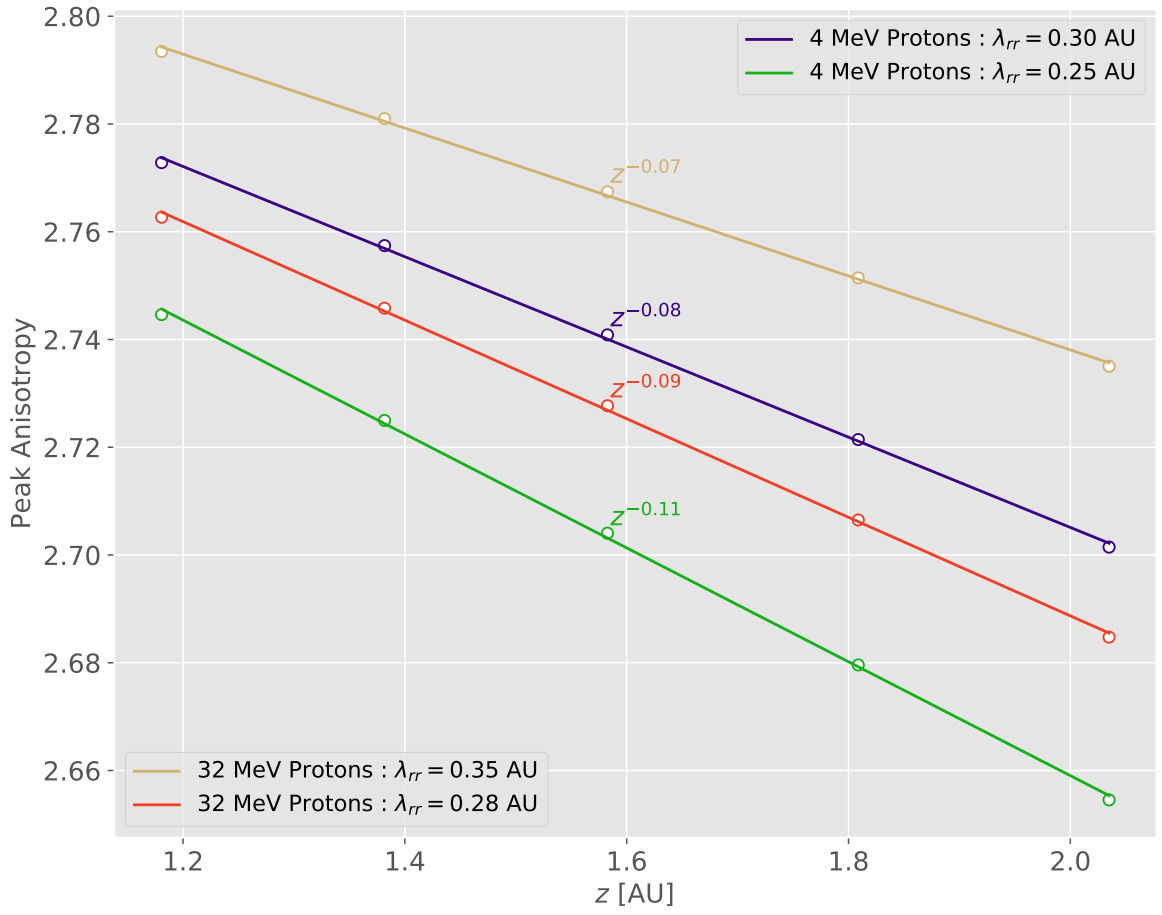

Figure 6.15: *Similar to Figure 6.13, except in this case, the power-law spatial dependence of the SEP peak anisotropies is shown. The functional form $z^{-\beta}$ with varying values of β, denoting the modelling results of the different SEP cases, is also included.*

The power-law spatial dependences of the SEP peak anisotropies are shown in Figure 6.15, along with the functional forms $A_{\max}(z) = z^{-\beta}$, with varying values of β. The values of β are found to be roughly in the range $[0.07, 0.11]$, with a median value of 0.18. The average peak anisotropy functional form is therefore approximately $z^{-0.18}$.

In terms of the transport effects from Figure 6.15, one can see that smaller λ_{rr} values lead to a faster peak anisotropy decrease with spatial distance (i.e. a larger positive value of β), contrary to what was observed for the peak intensities. In the physical sense, a small mean free path would lead to more interactions and/or scattering, which ultimately causes significant changes to the particle anisotropy, whereas a larger mean free path would lead to almost no interactions, and thus the anisotropy would remain nearly constant. The average power-law indices of the 4 and 32 MeV protons are found to be $\beta = 0.10$ and $\beta = 0.08$, respectively, which in this case means that, on average, less-energetic particles have a faster peak anisotropy decrease (i.e. a larger positive value of β) with spatial distance.

6.5 Radial distance vs. distance along the HMF

In this section, the radial dependence of SEP peak intensities observed along the Hohmann transfer orbit is studied, as is done by *Lario et al.* (2007) and *He et al.* (2017). Figure 6.16 shows the almost directly proportional relationship between the distance along the HMF z and the radial distance r, as described by Equation (4.6) between the Earth and Mars.

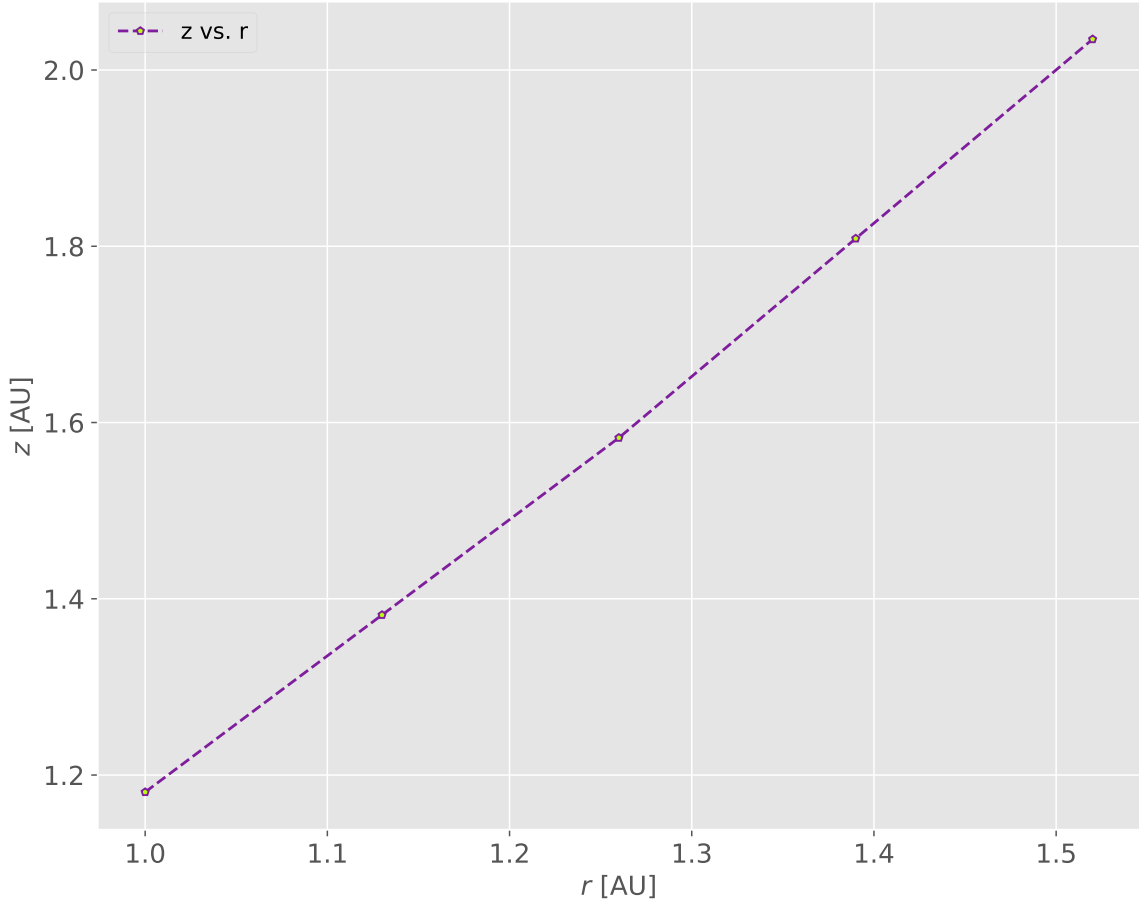

Figure 6.16: *The distance along the HMF z versus the radial distance r.*

The radial dependence of the SEP peak intensities is shown in Figure 6.17, along with the respective functional forms $r^{-\alpha}$. As shown in the figure, the power-law index α values are found to be in the range $[1.52, 1.98]$, with a median value of 1.74, which yields the average functional form of approximately $r^{-1.74}$.

Interestingly enough, the functional form found here corresponds relatively well to the lower limit of $r^{-1.7\pm0.1}$ obtained for a spacecraft fleet positioned along a HMF line proposed by *He et al.* (2017). In addition, the power-law index values found here are in agreement with those reported by *Lario et al.* (2007), where the radial dependence of 8.3 MeV proton peak intensities for a radial distance of $0.2-2$ AU was investigated. Similar to this study and that of *He et al.* (2017), *Lario et al.* (2007) also report a power-law decrease in the SEP peak intensities. They further found α to be parameter-dependent,

and varying from $\alpha = 1.56$ to $\alpha = 3.60$. This range includes the values presented here. Furthermore, *Lario et al.* (2013) considered five SEP events observed by various spacecraft. Looking at both proton and electron data, they found that the majority of the events yield functional forms $r^{-\alpha}$ with $\alpha < 3$, which is also in agreement with this study.

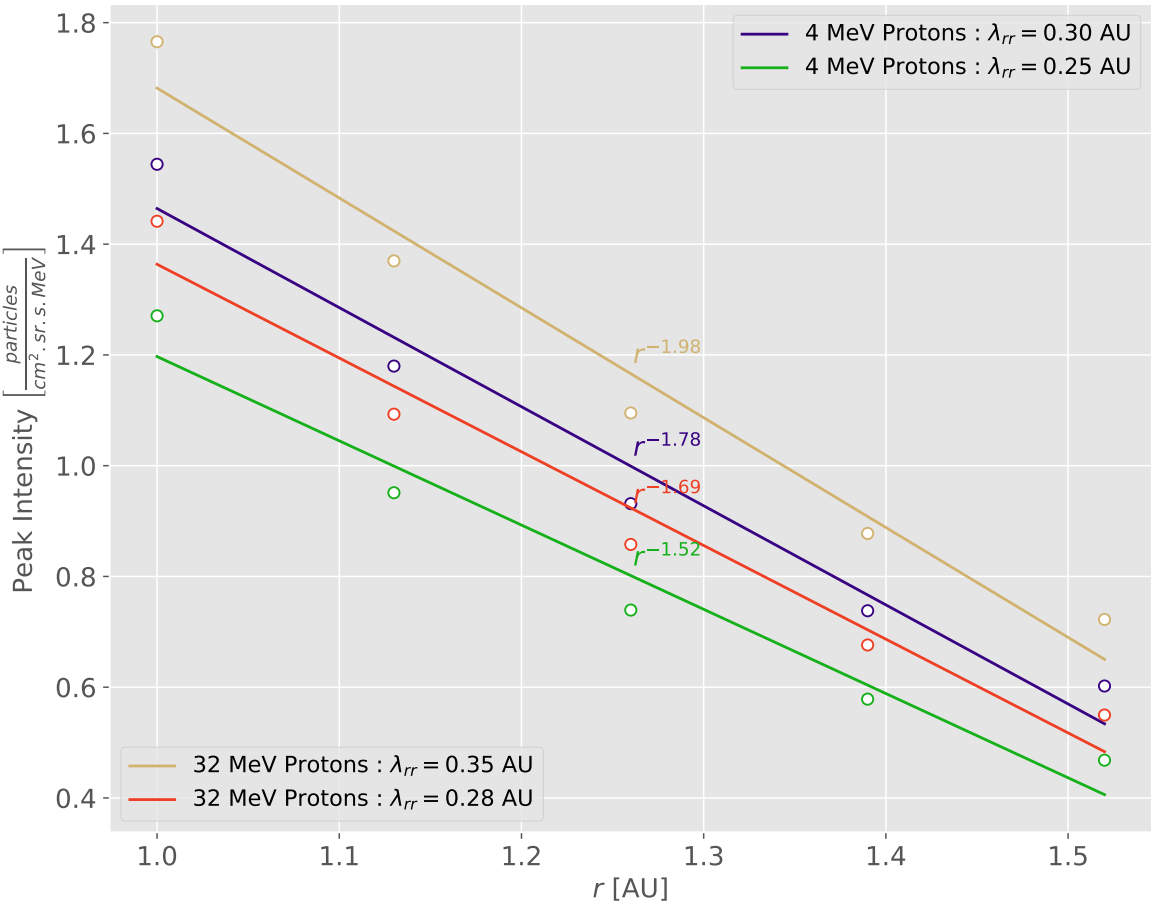

Figure 6.17: *Similar to Figure 6.14, except that the power-law radial dependence of the SEP peak intensities is shown. The functional form $r^{-\alpha}$ with varying values of α, corresponding to the simulation results of the different SEP cases, is also included.*

The significantly steeper decreases found in this section, relative to those of the previous section, are worth noting. This is mostly due to the much smaller radial distances involved when calculating particle intensities in terms of radial distance (r), rather than in terms of the distance along the HMF (z).

6.6 Time of Maximum

To better illustrate the importance of the radial mean free path on SEP transport, while simultaneously shedding light on the findings in Section 6.4.2, the spatial dependence of the so-called time of maximum $T_{\max}(z)$ along the Hohmann transfer orbit is studied. To achieve this, five scenarios are considered

for 4 MeV protons, with varying radial mean free path values of $0.25, 0.50, 0.75, 1.18$, and 2.0 AU. All other parameter values used are as listed in Table 4.1. In each of the SEP event scenarios, the time of maximum peak intensity at each of the fleet spacecraft is recorded.

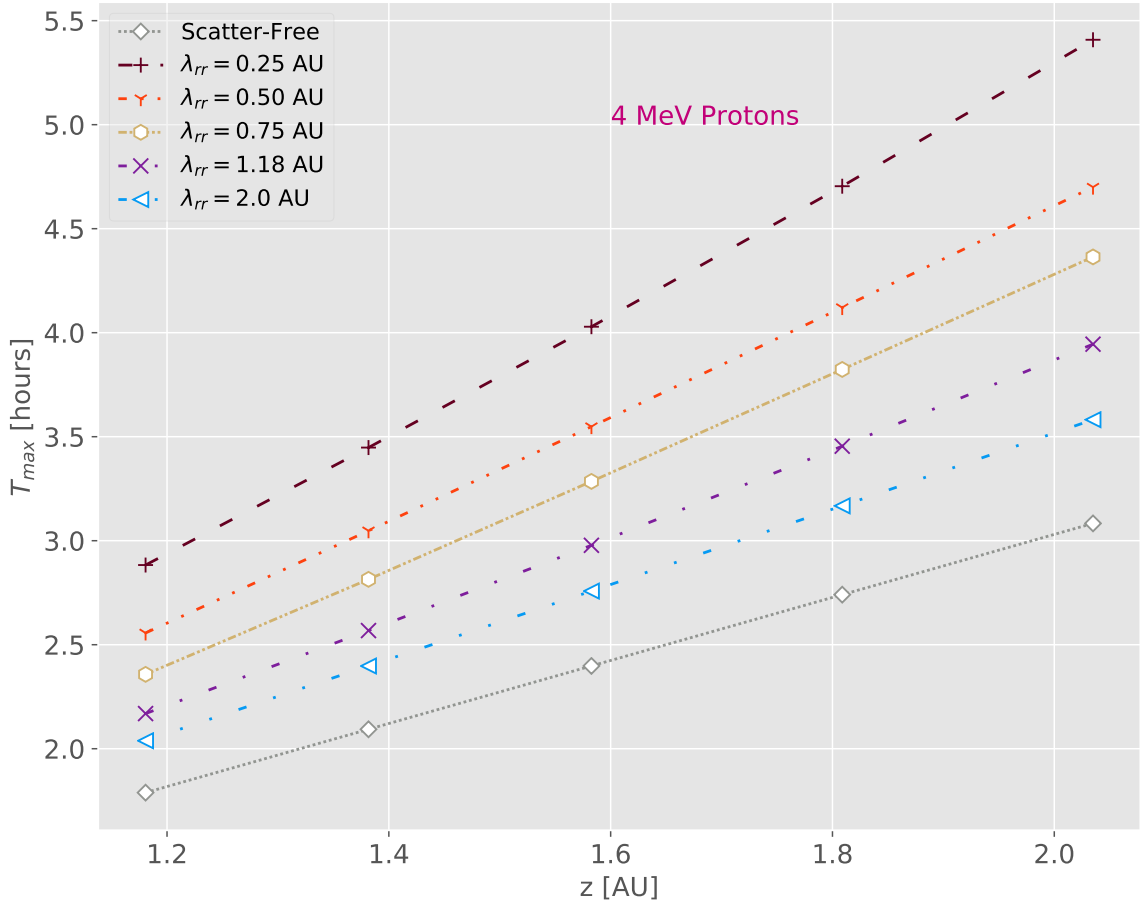

Figure 6.18: *The spatial dependence of the time of maximum $T_{\max}$, for five SEP events of 4 MeV protons along a Hohmann transfer orbit, and varying values for the radial mean free path λ_{rr}. The gray dashed line represents scatter-free SEP propagation.*

Figure 6.18 shows the spatial distribution of these recorded times. Also included in the figure is the scatter-free line (gray dashed line), which constitutes the idealistic case of scatter free propagation, and thus represents ballistic motion, i.e. $T_{\max}(z) = z/v$. From the figure, it can be seen that the smallest value of the radial mean free path ($\lambda_{rr} = 0.25$ AU; maroon loosely dashed line) leads to the largest maximum times at the various spacecraft positions. Using the largest mean free path value ($\lambda_{rr} = 2.0$ AU; azure loosely dash-dot-dotted line) leads to the smallest maximum times at each of the spacecraft positions. From this, one can then conclude that the time of maximum increases significantly with decreasing radial mean free path. To make sense of this, consider the fact that small values of the radial mean free path imply that there is more interaction between the particles, meaning that particles are significantly scattered and thus take longer to reach the spacecraft/observer. As expected, larger values of λ_{rr} lead to less interaction, and correspondingly smaller values of $T_{\max}$.

In addition, if one considers the magnitude of the PADC, given in Equation (4.35) as

$$D_{\mu\mu,0} = \frac{3v}{8} \cdot I \cdot \frac{\cos^2 \psi}{\lambda_{rr}}, \tag{6.1}$$

it is easy to see that smaller values of λ_{rr} lead to a larger value of $D_{\mu\mu,0}$, whereas larger values of λ_{rr} lead to smaller values of $D_{\mu\mu,0}$. As seen in Figure 6.18, larger values of λ_{rr} are expected to approximately result in scatter free SEP propagation.

Reconciling the findings of this and the previous section, one can infer that the slower decrease in the peak intensities found in the previous section is a result of small values of λ_{rr} leading to large maximum times, whereas the faster peak intensity decreases found in the previous section are due to the significantly smaller maximum times that arise from large values of λ_{rr}.

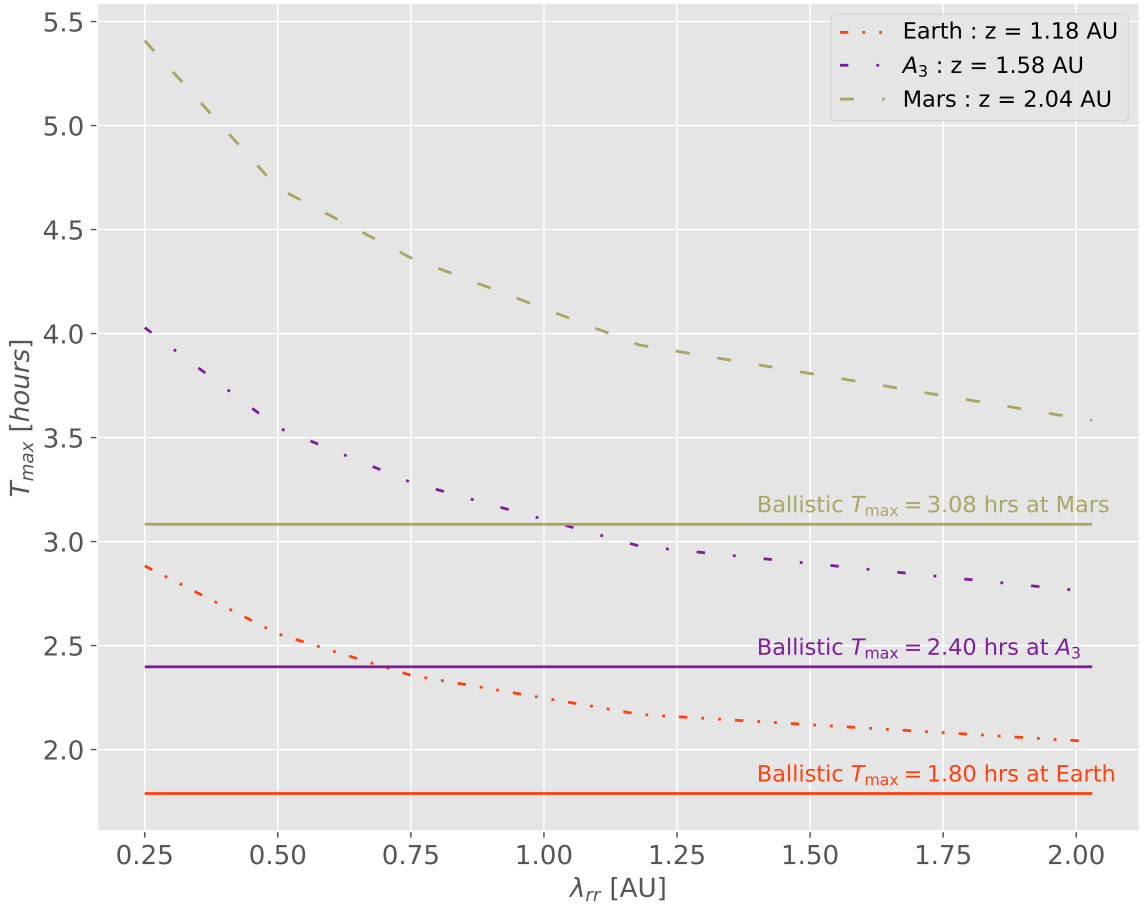

Figure 6.19: *The variability of the time of maximum $T_{\max}$ with respect to the radial mean free path λ_{rr}, shown for three different positions. The corresponding ballistic motion $T_{\max}$ values (denoting SEP scatter-free propagation) are also included (solid lines).*

Figure 6.19 shows the times of maximum observed at three different positions, Earth ($z = 1.18$ AU), an intermediate spacecraft position ($z = 1.58$ AU), and Mars ($z = 2.04$ AU), as function of the radial mean free path λ_{rr}. For a given λ_{rr} value, the corresponding $T_{\max}$ values denote the moments at which the SEP event intensity reaches its peak at the three different positions. Peak intensities are

expected to be most harmful. From the figure it can also be seen that for larger values of λ_{rr} the calculated values of $T_{\max}$ approach the no scattering ballistic scenario values.

The time $T_{\max}$ varies at Earth from a maximum value of $\sim$ 2.8 hours (highest scattering case) to a minimum of $\sim$ 2.04 hours (lowest scattering case), with an average $T_{\max}$ value of $\sim$ 2.4 hours. Spacecraft A_3 sees $T_{\max}$ vary from a maximum of $\sim$ 4 hours (highest scattering case), and reach a minimum of $\sim$ 2.7 hours (low scattering case), with an average $T_{\max}$ value of $\sim$ 3.3 hours. Finally, at Mars $T_{\max}$ varies from $T_{\max} \sim$ 5.4 hours (highest scattering case) to $T_{\max} \sim$ 3.6 hours (lowest scattering case), and has an average of $\sim$ 4.4 hours. Therefore, using only these three positions and the respective average $T_{\max}$ values, one can infer crude "warning times" of $\sim$ 54 minutes between Earth and spacecraft A_3, and $\sim$ 66 minutes between spacecraft A_3 and Mars. In a practical sense, an SEP event peak intensity detected at Earth would give a spacecraft crew halfway along a Hohmann transfer to Mars approximately 1 hour before the same SEP event's intensity peaks at their position. This time would give the spacecraft crew ample time to access their SEP event storm shelter, as described by *Townsend et al.* (2018). A would-be Mars colony would have an approximately 2 hour warning after event detection at Earth, and approximately half of that once the SEP event peaks at Spacecraft A_3, before the "Martians" bear the brunt of the SEP event.

6.7 Summary and Conclusions

In this chapter, the Hohmann-Parker effect (*Posner et al.*, 2013) was introduced, and its scientific implications in relation to SEP propagation along Hohmann transfer orbits (*Hohmann*, 1925) were discussed. It was concluded that the Hohmann-Parker effect makes the one-dimensional modelling of SEP propagation along Hohmann transfer orbits viable. Thereafter, the simulated SEP intensities of 4 and 32 MeV protons for varying radial mean free paths λ_{rr} were presented and discussed.

From these simulation results, the peak intensities $I_{\max}(z)$ and anisotropies $A_{\max}(z)$ were extracted from the corresponding SEP intensity and anisotropy temporal profiles. Their spatial (co-ordinate along the field line) dependence was then investigated. Thereafter, functional forms $I_{\max}(z) = z^{-\alpha}$ and $A_{\max}(z) = z^{-\beta}$ were obtained for the peak intensity and peak anisotropy, respectively. The power-law index α for the peak intensities was found to be in the range $[0.92, 1.20]$, with a median value of 1.06, thus displaying an average functional form of $I_{\max}(z) = z^{-1.06}$. Moreover, it was shown that small values of the radial mean free path lead to a slower decrease of the peak intensities with spatial distance due to the larger maximum times associated with more scattering interactions between SEPs and the underlying turbulence. The faster peak intensity decreases were attributed to the significantly smaller maximum times arising from large values of the radial mean free path. The power-law index β for the peak anisotropies was found to be in the relatively narrow range of $[0.07, 0.11]$, with a median value of 0.18, which yields an average functional form of $A_{\max}(z) = z^{-0.18}$. Additionally, it was found that smaller radial mean free path values lead to a faster peak anisotropy decrease with

spatial distance, due to the significantly higher level of scattering associated with smaller mean free paths.

The present study did not solely look at the spatial dependence of SEP peak intensities, but also investigated their radial dependence. In the latter case, an average functional form of $r^{-1.74}$ was found, which was found to be in relative agreement (although steeper) with the lower limit functional form $r^{-1.7\pm0.1}$ proposed by *He et al.* (2017). Furthermore, the power-law index values ($\alpha = 1.52, 1.69, 1.78,$ and 1.98) were found to be well within the range of $\alpha = 1.56$ to $\alpha = 3.60$ obtained by *Lario et al.* (2007).

Given the radiation risk SEPs (especially highly energetic protons) would pose to a manned mission along the Hohmann transfer, three different positions, one at Earth, the other at A_3; situated at an intermediate distance between Earth and Mars, and the third at Mars were considered. "Warning times" of approximately 1 hour were found between both the Earth-A_3, and the A_3-Mars distances. These times would ideally be used to provide ample warning for the spacecraft crew to seek shelter during a particle storm.

A study by *Lario et al.* (2013) investigated the radial dependence of SEP peak intensities from five events observed by STEREO, ACE, SOHO, GOES, and MESSENGER. They considered both proton and electron observations at varying energies. They found the power-law index α to vary significantly, with three out of the five events being found to have a functional form $r^{-\alpha}$ with $\alpha < 3$ (as found in this study), whereas for the other two events a functional form for which $\alpha > 3$ was found. It is a goal of this study that the findings provided in this chapter be used to predict and/or explain the observational data taken by future spacecraft undergoing a Hohmann transfer orbit between Earth and Mars, in the same vein as the study of *Lario et al.* (2013).

CHAPTER 7

Summary and Conclusions

The current interest in interplanetary space travel, although very exciting, has raised critical questions pertaining to the potential impact of SEPs on both man and machine in space. This has made the topic of SEP transport a priority in space weather research. This study, using the Hohmann-Parker effect (*Posner et al.*, 2013), attempted to provide insight into SEP transport along a Hohmann transfer trajectory (*Hohmann*, 1925) between the Earth and Mars by using a 1D finite-difference SEP transport model based on the *Roelof* (1969) equation.

The necessary background on solar activity (solar flares, coronal mass ejections, and the solar wind), and the *Parker* (1958) HMF was discussed. An overview of SEPs, along with their relevant transport mechanisms (1D streaming along the mean HMF, focusing in diverging field lines, and pitch-angle scattering) was given.

Introductions to the finite-difference (FD) method and general second-order PDEs were given. The application of the FD numerical schemes/techniques to the diffusion and advection equations revealed that FD numerical schemes can be highly dispersive and/or diffusive, leading to numerical oscillations in certain cases. Fortunately, flux-limiters such as the van Leer, Minmod, and Superbee were found to minimize the diffusiveness present in especially the Forward Upwind scheme. A new flux-limiter, called the Tan limiter due to its use of the trigonometric tan function was developed, and thereafter found to compare relatively well with respect to the other well known limiters.

The relevant mathematical expressions (1D streaming along the mean HMF, focusing in diverging field lines, and pitch-angle scattering) forming part of the *Roelof* (1969) equation were discussed, along with their finite-difference numerical implementation. The key assumptions of the model, relevant SEP transport coefficients, and standard model parameters were also given.

The 1D finite-difference SEP transport model was shown to compare well with the contemporary modelling approaches of *Dröge et al.* (2010), *Effenberger and Litvinenko* (2014), *Strauss and Fichtner* (2015), and *van den Berg* (2018). From the latter, it was found that a choice of the Superbee limiter for both the distance along the magnetic field line z and the pitch-angle cosine μ coordinates provided the best comparison with respect to the models mentioned above. It is worth noting that the van Leer and Tan limiter combination for the respective z and μ coordinates also provided a reasonably good comparison.

The Hohmann-Parker effect (*Posner et al.*, 2013) was introduced, along with a discussion as to why it allows for the modelling of SEP transport along the Hohmann transfer trajectory (*Hohmann*, 1925). The simulation results for 4 and 32 MeV protons, using different values of λ_{rr}, were shown and discussed. The spatial and radial dependences of the SEP peak intensities, and the anisotropies of these simulation results, were discussed. Thereafter, functional forms $I_{\max}(z) = z^{-\alpha}$ and $A_{\max}(z) = z^{-\beta}$, were obtained for the peak intensities and anisotropies, with α and β being the power-law indices. The peak intensities were shown to have an average functional form of $\sim z^{-1.06}$, which was found to decrease with decreasing λ_{rr} values. The peak anisotropies were shown to display a relatively flatter average functional form of $\sim z^{-0.18}$, which was found to increase with decreasing λ_{rr} values. The radial dependence of the SEP peak intensities was also investigated, and an average functional form of $\sim r^{-1.74}$ was obtained. The latter was shown to be in general agreement with results from similar numerical studies by *Lario et al.* (2007), and *He et al.* (2017), and with an observational study by *Lario et al.* (2013).

The so-called time of maximum was discussed, and it was shown that a spacecraft crew halfway to Mars along the Hohmann transfer trajectory, assuming 4 MeV protons and varying scattering conditions, will have a "warning time" of approximately one hour once an SEP event peaks at Earth. This corresponds to a "warning time" of $\sim$ 2 hours should the crew be at Mars itself.

In the future, the radial dependence of intensities of electrons can also be investigated, due to the danger they pose to spacecraft components, and a detailed comparison between spacecraft observations along a Hohmann transfer and simulation results can be used to further constrain the warning time.

Acknowledgements

- To undoubtedly the coolest supervisor one could ever have, Prof. R.D. Strauss. Many thanks for all the thought-provoking research discussions regarding this study, expert guidance, and your detailed and assiduous revision of this thesis.
- I am grateful to Dr. N.E. Engelbrecht, for going through this study to ensure that the language and grammar, and to a certain degree the physics, are in order.
- A very special word of gratitude goes out to Mrs Petro Sieberhangen (Tannie Petro) for handling all my administrative queries.
- I am thankful to Mr. Holleran for his outstanding technical support.
- I am also grateful to the South African National Research Foundation, and the Center for Space Research of the NWU, for financial support throughout my studies.
- Finally, I am profoundly grateful to my mother, Ruth, for her love, support, and motivation.

Phillip Heita

Centre for Space Research, North-West University, South Africa

November 2018

Bibliography

Aharonian, F., A. Bykov, E. Parizot, V. Ptuskin, and A. Watson, Cosmic rays in galactic and extragalactic magnetic fields, *Space Science Reviews*, *166*(1), 97–132, 2012.

Antiochos, S. K., C. R. DeVore, and J. A. Klimchuk, The structure of solar prominences, in *American Astronomical Society Meeting Abstracts #194*, *Bulletin of the American Astronomical Society*, vol. 31, p. 868, 1999.

Antonia, R. A., L. Djenidi, L. Danaila, and S. L. Tang, Small scale turbulence and the finite reynolds number effect, *Physics of Fluids*, *29*(2), 20–715, 2017.

Axford, W. I., E. Leer, and G. Skadron, The acceleration of cosmic rays by shock waves, *International Cosmic Ray Conference*, *11*, 132–137, 1977.

Balogh, A., and E. J. Smith, The heliospheric magnetic field at solar maximum: Ulysses observations, *Space Science Review*, *97*(1), 147–160, 2001.

Balogh, A., E. J. Smith, B. T. Tsurutani, D. J. Southwood, R. J. Forsyth, and T. S. Horbury, The heliospheric magnetic field over the south polar region of the sun, *Science*, *268*(5213), 1007–1010, 1995.

Balogh, A., L. J. Lanzerotti, and S. T. Suess, The Heliosphere through the Solar Activity Cycle, Springer, Berlin, Heidelberg, 2008.

Belcher, J. W., and L. Davis, Jr., Large-amplitude Alfvén waves in the interplanetary medium, 2, *Journal of Geophysical Research*, *76*, 3534–3563, 1971.

Bell, A. R., The acceleration of cosmic rays in shock fronts. i, *Monthly Notices of the Royal Astronomical Society*, *182*, 147–156, 1978.

Bieber, J. W., W. H. Matthaeus, C. W. Smith, W. Wanner, M.-B. Kallenrode, and G. Wibberenz, Proton and electron mean free paths: The Palmer consensus revisited, *The Astrophysical Journal*, *420*, 294–306, 1994.

Bieber, J. W., W. Wanner, and W. H. Matthaeus, Dominant two-dimensional solar wind turbulence with implications for cosmic ray transport, *Journal of Geophysical Research*, *101*, 2511–2522, 1996.

Biermann, L., Kometenschweife und solare korpuskularstrahlung, *Zentrum für Arbeit und Politik*, *29*, 274, 1951.

Biermann, L., Solar corpuscular radiation and the interplanetary gas, *The Observatory*, *77*, 109–110, 1957.

Brio, M., A. Zakharian, and G. Webb, Numerical Partial Differential Equations for Scientists and Engineers, Academic Press, New York, 2010.

Bruno, R., and B. Bavassano, On the winding of the imf spiral for slow and fast wind within the inner heliosphere, *Geophysical Research Letters*, *24*(18), 2267–2270, 1997.

Bruno, R., and V. Carbone, The solar wind as a turbulence laboratory, *Living Reviews in Solar Physics*, *10*(1), 2, 2013.

Burger, R. A., T. P. J. Kr??uger, M. Hitge, and N. E. Engelbrecht, A fisk-parker hybrid heliospheric magnetic field with a solar-cycle dependence, *The Astrophysical Journal*, *674*, 511–519, 2008.

Burlaga, F., Interplanetary stream interfaces, *Journal of Geophysical Research*, *79*, 1974.

Chen, F., Introduction to plasma physics, 1974.

Choudhuri, A. R., The physics of fluids and plasmas : an introduction for astrophysicists, Cambridge University Press, 1998.

Coleman, P. J., Jr., Turbulence, viscosity, and dissipation in the solar-wind plasma, *The Astrophysical Journal*, *153*, 371, 1968.

Courant, R., K. Friedrichs, and H. Lewy, On the partial difference equations of mathematical physics, *IBM Journal of Research and Development*, *11*, 215–234, 1967.

Cranmer, S. R., Coronal holes, *Living Reviews in Solar Physics*, *6*, 3, 2009.

Cummings, C., and C. Stone, Anomalous cosmic rays, *AIP Conference Proceedings*, *1516*, 97–101, 2013.

Czechowski, A., M. Strumik, J. Grygorczuk, S. Grzedzielski, R. Ratkiewicz, and K. Scherer, Structure of the heliospheric current sheet from plasma convection in time-dependent heliospheric models, *Astronomy and Astrophysics*, *516*, A17, 2010.

de Blank, H. J., Guiding center motion, *Fusion Science and Technology*, *49*(2T), 59–66, 2006.

Dorman, L. I., and L. Pustil'Nik, Expected radiation hazard at different phases of solar cycle based on statistical properties of solar energetic particle fluencies, *Sun and Geosphere*, *3*, 7–9, 2008.

Dresing, N., R. Gómez-Herrero, A. Klassen, B. Heber, Y. Kartavykh, and W. Dröge, The large longitudinal spread of solar energetic particles during the 17 January 2010 solar event, *Solar Physics*, *281*(1), 281–300, 2012.

Dresing, N., R. GÃşmez-Herrero, B. Heber, A. Klassen, O. Malandraki, W. Droege, and Y. Kartavykh, Statistical survey of widely spread out solar electron events observed with STEREO and ACE with special attention to anisotropies, *Astronomy and Astrophysics*, *567*, 27, 2014.

Dröge, W., Y. Y. Kartavykh, B. Klecker, and G. A. Kovaltsov, Anisotropic three-dimensional focused transport of solar energetic particles in the inner heliosphere, *The Astrophysical Journal*, *709*(2), 912, 2010.

Dröge, W., Y. Y. Kartavykh, N. Dresing, B. Heber, and A. Klassen, Wide longitudinal distribution of interplanetary electrons following the 7 February 2010 solar event: Observations and transport modeling, *Journal of Geophysical Research: Space Physics*, *119*(8), 6074–6094, 2014.

Effenberger, F., and Y. Litvinenko, The diffusion approximation versus the telegraph equation for modeling solar energetic particle transport with adiabatic focusing. i. isotropic pitch-angle scattering, *783*, 2014.

Ellison, D. C., and S. P. Reynolds, Electron acceleration in a nonlinear shock model with applications to supernova remnants, *The Astrophysical Journal*, *382*, 242–254, 1991.

Engelbrecht, N. E., On the heliospheric diffusion tensor and its effect on 26-day recurrent cosmic-ray variations, Master's thesis, North-West University (Potchefstroom Campus), 2008.

Erdős, G., Waves and turbulence in the solar wind, in *Turbulence, Waves and Instabilities in the Solar Plasma*, edited by R. Erdélyi, K. Petrovay, B. Roberts, and M. Aschwanden, pp. 367–386, Springer Netherlands, Dordrecht, 2003.

Ferreira, S., The heliospheric transport of galactic cosmic rays and jovian electrons, Ph.D. thesis, Potchefstroom University for CHE, South Africa, 2002.

Ferreira, S. E. S., M. S. Potgieter, R. A. Burger, B. Heber, and H. Fichtner, Modulation of Jovian and galactic electrons in the heliosphere: 1. latitudinal transport of a few mev electrons, *Journal of Geophysical Research*, *106*, 24,979–24,988, 2001.

Fichtner, H., Anomalous cosmic rays: Messengers from the outer heliosphere, *Space Science Reviews*, *95*(3), 639–754, 2001.

Fisk, L. A., B. Kozlovsky, and R. Ramaty, An interpretation of the observed oxygen and nitrogen enhancements in low-energy cosmic rays, *The Astrophysical Journal Letters*, *190*, 35, 1974.

Florinski, V., and N. V. Pogorelov, Four-dimensional transport of galactic cosmic rays in the outer heliosphere and heliosheath, *The Astrophysical Journal*, *701*(1), 642, 2009.

Forbush, S. E., Three unusual cosmic-ray increases possibly due to charged particles from the sun, *Physical Review*, *70*, 771–772, 1946.

Gazis, P. R., Observations of plasma bulk parameters and the energy balance of the solar wind between 1 and 10 AU, *Journal of Geophysical Research*, *89*, 775–785, 1984.

Giacalone, J., J. R. Jokipii, and W. H. Matthaeus, Structure of the turbulent interplanetary magnetic field, *The Astrophysical Journal Letters*, *641*(1), 61, 2006.

Giordano, N. J., and H. Nakanishi, Computational physics, 2nd ed., Upper Saddle River, NJ : Pearson/Prentice Hall, 2006.

Godunov, S. K., A difference scheme for numerical solution of discontinuous solution of hydrodynamic equations, *Math. Sbornik, translated US Joint Publ. Res. Service, JPRS 7226*, *47*, 271–306, 1959.

Gombosi, T. I., *Physics of the Space Environment*, Cambridge Atmospheric and Space Science Series, Cambridge University Press, 1998.

Gosling, J., and V. Pizzo, Formation and evolution of corotating interaction regions and their three dimensional structure, *Space Science Reviews*, *89*(1), 21–52, 1999.

Gosling, J., J. R. Asbridge, S. J. Bame, and W. C. Feldman, Solar wind stream interfaces, *Journal of Geophysical Research*, *83*, 1978.

Grigoryan, V., Partial differential equations, retrieved from http://www.math.ucsb.edu/ grigoryan/124a.pdf, PDF Document, 2010.

Guo, J., Private Communication, 2018.

Hale, G. E., On the probable existence of a magnetic field in sun-spots, *The Astrophysical Journal*, *28*, 315, 1908.

Hamilton, C. D., M. G. Mason, and B. F. McDonald, The radial dependence of the peak flux and fluence in solar energetic particle events, *International Cosmic Ray Conference*, *5*, 237, 1990.

Harten, A., High resolution schemes for hyperbolic conservation laws, *Journal of Computational Physics*, *49*(3), 357–393, 1983.

Hasselmann, K., and G. Wibberenz, Scattering of charged particles by random electromagnetic fields, *Zeitschrift für Geophysik*, *34*, 1968.

Hassler, D. M., et al., The radiation assessment detector investigation, *Space Science Reviews*, *170*, 503–558, 2012.

Hassler, D. M., et al., Mars' surface radiation environment measured with the mars science laboratory's curiosity rover, *Science*, *343*(6169), 2014.

Hathaway, D. H., The solar cycle, *Living Reviews in Solar Physics*, *7*(1), 2010.

Hatzky, R., Numerics of interplanetary transport, *International Cosmic Ray Conference*, *6*, 320, 1999.

He, H.-Q., and W. Wan, A direct method to determine the parallel mean free path of solar energetic particles with adiabatic focusing, *The Astrophysical Journal*, *747*(1), 38, 2012.

He, H.-Q., G. Qin, and M. Zhang, Propagation of solar energetic particles in three-dimensional interplanetary magnetic fields: In view of characteristics of sources, *The Astrophysical Journal*, *734*(2), 74, 2011.

He, H.-Q., G. Zhou, and W. Wan, Propagation of solar energetic particles in three-dimensional interplanetary magnetic fields: Radial dependence of peak intensities, *The Astrophysical Journal*, *842*(2), 71, 2017.

Hitge, M., and R. Burger, Cosmic ray modulation with a fisk-type heliospheric magnetic field and a latitude-dependent solar wind speed, *Advances in Space Research*, *45*(1), 18–27, 2010.

Hoffman, J., and S. Frankel, Numerical Methods for Engineers and Scientists, *Boca Raton: CRC Press*, 2001.

Hohmann, W., *Die Erreichbarkeit der Himmelskörper*, München, Germany: R. Oldenbourg, 1925.

Holden, H., K. Karlsen, K.-A. Lie, and H. Risebro, Splitting methods for partial differential equations with rough solutions. Analysis and Matlab programs, *European Mathematical Society*, 2010.

Hu, S., M.-H. Y Kim, G. E McClellan, and F. Cucinotta, Modeling the acute health effects of astronauts from exposure to large solar particle events, *96*, 465–76, 2009.

Hundhausen, A. J., Coronal Expansion and Solar Wind, 101 pp., *Springer, Berlin, Heidelberg*, 1972.

Iserles, A., Numerical solution of partial differential equations: finite difference methods (3rd edition), by G.D. Smith. pp 337. 1985. (Oxford University Press), *The Mathematical Gazette*, *70*(454), 330–332, 1986.

Jokipii, J., and E. Parker, On the convection, diffusion, and adiabatic deceleration of cosmic rays in the solar wind, *The Astrophysical Journal*, *160*, 1970.

Jokipii, J. R., Cosmic-ray propagation. i. charged particles in a random magnetic field, *The Astrophysical Journal*, *146*, 480, 1966.

Jokipii, J. R., and J. Kota, The maximum energy of anomalous cosmic rays, *International Cosmic Ray Conference*, *4*, 718, 1995.

Jokipii, J. R., and B. Thomas, Effects of drift on the transport of cosmic rays. iv - modulation by a wavy interplanetary current sheet, *The Astrophysical Journal*, *243*, 1115–1122, 1981.

Kallenrode, M.-B., Current views on impulsive and gradual solar energetic particle events, *Journal of Physics G Nuclear Physics*, *29*, 965–981, 2003.

Kallenrode, M.-B., Space physics : an introduction to plasmas and particles in the heliosphere and magnetospheres, *Springer-Verlag Berlin Heidelberg*, 2004.

Kolmogorov, A., The local structure of turbulence in incompressible viscous fluid for very large Reynold's numbers, *Akademiia Nauk SSSR Doklady*, *30*, 301–305, 1941.

Kubo, Y., R. Kataoka, and T. Sato, Interplanetary particle transport simulation for warning system for aviation exposure to solar energetic particles, *Earth, Planets and Space*, *67*(1), 117, 2015.

Laitinen, T., S. Dalla, and M. Marsh, Energetic particle cross-field propagation early in a solar event, *773*, 2013.

Lampa, F., Modeling solar cosmic ray transport within the ecliptic plane, Ph.D. thesis, Osnabrück, 2011.

Lapidus, L., and G. F. Pinder, Numerical solution of partial differential equations in science and engineering, *John Wiley & Sons, New York*, 1982.

Lario, D., A. Aran, N. Agueda, and B. Sanahuja, Radial dependence of proton peak intensities and fluences in sep events: Influence of the energetic particle transport parameters, *Advances in Space Research*, *40*(3), 289–294, 2007.

Lario, D., A. Aran, R. Gómez-Herrero, N. Dresing, B. Heber, G. C. Ho, R. B. Decker, and E. C. Roelof, Longitudinal and radial dependence of solar energetic particle peak intensities: STEREO, ACE, SOHO, GOES, and MESSENGER observations, *The Astrophysical Journal*, *767*(1), 41, 2013.

Larson, D. E., et al., The MAVEN solar energetic particle investigation, *Space Science Reviews*, *195*, 153–172, 2015.

Lax, P., and B. Wendroff, Systems of conservation laws, *Communications on Pure and Applied Mathematics*, *13*(2), 217–237, 1960.

Lockwood, M., and R. Stamper, Long-term drift of the coronal source magnetic flux and the total solar irradiance, *Geophysical Research Letters*, *26*, 2461–2464, 1999.

Mackay, D. J. C., Information Theory, Inference and Learning Algorithms, 640 pp., Cambridge, UK: *Cambridge University Press*, 2003.

MacQueen, R. M., J. A. Eddy, J. T. Gosling, E. Hildner, R. H. Munro, G. A. Newkirk, Jr., A. I. Poland, and C. L. Ross, The outer solar corona as observed from Skylab: Preliminary results, *The Astrophysical Journal*, *187*, 85, 1974.

Manchester, W. B., A. J. Ridley, T. I. Gombosi, and D. L. Dezeeuw, Modeling the Sun-to-Earth propagation of a very fast CME, *Advances in Space Research*, *38*, 253–262, 2006.

Manuel, R., Time-dependent modulation of cosmic rays in the outer heliosphere, Ph.D. thesis, North-West University (Potchefstroom Campus), South Africa, 2013.

Marchuk, G., Splitting and alternating direction methods, pp. 197–462, North-Holland, Amsterdam: *Elsevier*, 1990.

Matthaeus, W. H., M. L. Goldstein, and D. A. Roberts, Evidence for the presence of quasi-two-dimensional nearly incompressible fluctuations in the solar wind, *Journal of Geophysical Research*, *95*, 20,673–20,683, 1990.

Matthaeus, W. H., P. C. Gray, D. H. Pontius, Jr., and J. W. Bieber, Spatial structure and field-line diffusion in transverse magnetic turbulence, *Physical Review Letters*, *75*, 2136–2139, 1995.

Matthaeus, W. H., G. Qin, J. W. Bieber, and G. P. Zank, Nonlinear collisionless perpendicular diffusion of charged particles, *The Astrophysical Journal Letters*, *590*(1), 53, 2003.

Mazumder, S., Numerical methods for partial differential equations: finite difference and finite volume methods, *Academic Press*, 2015.

McComas, D. J., et al., Solar wind observations over Ulysses' first full polar orbit, *Journal of Geophysical Research*, *105*, 10,419–10,434, 2000.

McComas, D. J., et al., Integrated Science Investigation of the Sun (ISIS): Design of the energetic particle investigation, *Space Science Reviews*, *204*(1), 187–256, 2016.

McGuire, R. E., M. A. I. Van Hollebeke, and N. Lal, A multi-spacecraft study of the coronal and interplanetary transport of solar cosmic rays. i, ii, *International Cosmic Ray Conference*, *10*, 353–360, 1983.

McKibben, R. B., et al., Ulysses COSPIN observations of cosmic rays and solar energetic particles from the south pole to the north pole of the Sun during solar maximum, *Annales Geophysicae*, *21*, 1217–1288, 2003.

Meyer-Vernet, N., Basics of the Solar Wind, *Cambridge University Press*, 2007.

Moldwin, M., An Introduction to Space Weather, *Cambridge University Press*, 2008.

Ng, C. K., and K.-Y. Wong, Solar particle propagation under the influence of pitch-angle diffusion and collimation in the interplanetary magnetic field, *International Cosmic Ray Conference*, *5*, 252, 1979.

Ofman, L., The origin of the slow solar wind in coronal streamers, *Advances in Space Research*, *33*, 681–688, 2004.

Parker, E. N., Dynamics of the interplanetary gas and magnetic fields., *The Astrophysical Journal*, *128*, 664, 1958.

Parker, E. N., Interplanetary dynamical processes, *Interscience Publishers*, 1963.

Parker, E. N., Sunspots and the physics of magnetic flux tubes. i - the general nature of the sunspot. ii - aerodynamic drag, *The Astrophysical Journal*, *230*, 905–923, 1979.

Phillips, K., Guide to the Sun, *Cambridge University Press*, 1992.

Posner, A., et al., The Hohmann-Parker effect measured by the Mars science laboratory on the transfer from Earth to Mars: Consequences and opportunities, *Planetary Space Science*, *89*, 127–139, 2013.

Reames, D. V., Bimodal abundances in the energetic particles of solar and interplanetary origin, *The Astrophysical Journal Letters*, *330*, 71–75, 1988.

Reames, D. V., Solar energetic particle variations, *Advances in Space Research*, *34*, 381–390, 2004.

Reames, D. V., The two sources of solar energetic particles, *Space Science Reviews*, *175*(1), 53–92, 2013.

Riley, P., J. A. Linker, and Z. Mikić, Modeling the heliospheric current sheet: Solar cycle variations, *Journal of Geophysical Research: Space Physics*, *107*(A7), 81–86, 2002.

Roe, P. L., Some contributions to the modelling of discontinuous flows, in *Large-Scale Computations in Fluid Mechanics*, edited by R. L. Lee, R. L. Sani, T. M. Shih, and P. M. Gresho, pp. 163–193, American Mathematical Society, 1985.

Roelof, E. C., Propagation of solar cosmic rays in the interplanetary magnetic field, in *Lectures in High-Energy Astrophysics*, edited by H. Ögelman and J. R. Wayland, p. 111, 1969.

Ruffolo, D., Effect of adiabatic deceleration on the focused transport of solar cosmic rays, *The Astrophysical Journal*, *442*, 861–874, 1995.

Schlaepfer, H., Cosmic rays, *Spatium*, *11*, 1–15, 2003.

Schwabe, H., Solar observations during 1843, *Astronomische Nachrichten*, (20), 495, 1843.

Schwenn, R., Solar wind sources and their variations over the solar cycle, *Space Science Review*, *124*, 51–76, 2006.

Scott, S., The method of characteristics with applications to conservation laws, *Journal of Online Mathematics and Applications*, *3*, 2003.

Sethian, J., A fast marching level set method for monotonically advancing fronts, *Proceedings of the National Academy of Sciences*, *93*, 1591–1595, 1996.

Simpson, J., Cosmic-radiation neutron intensity monitor, *Annals of the International Geophysical Year*, *4*, 351–373, 1957.

Simpson, J. A., D. C. Hamilton, R. B. McKibben, A. Mogro-Campero, K. R. Pyle, and A. J. Tuzzolino, The protons and electrons trapped in the jovian dipole magnetic field region and their interaction with io, *Journal of Geophysical Research*, *79*, 3522, 1974.

Smith, E., The Sun, solar wind, and magnetic field. i, in course cxlii, edited by A. Ferrari and E. Sindoni, in proc. int. sch. of phys. Enrico Fermi, 2000.

Smith, E. J., The heliospheric current sheet, *Journal of Geophysical Research: Space Physics*, *106*(A8), 15,819–15,831, 2001.

Smith, E. J., Solar cycle evolution of the heliospheric magnetic field: The Ulysses legacy, *Journal of Atmospheric and Solar-Terrestrial Physics*, *73*, 277–289, 2011.

Smith, J., and H. Wolfe, Observations of interaction regions and corotating shocks between one and 5 AU-pioneer-10 and pioneer-11, *Geophysical Research Letters*, *3*, 1976.

Snodgrass, H. B., Magnetic rotation of the solar photosphere, *The Astrophysical Journal*, *270*, 288–299, 1983.

Springel, V., High performance computing and numerical modelling, *Springer-Verlag Berlin Heidelberg*, *43*, 251, 2016.

Steenkamp, R., Shock acceleration as source of the anomalous component of cosmic rays in the heliosphere, Ph.D. thesis, Potchefstroom University for CHE, South Africa, 1995.

Sternal, O., N. E. Engelbrecht, R. A. Burger, S. E. S. Ferreira, H. Fichtner, B. Heber, A. Kopp, M. S. Potgieter, and K. Scherer, Possible evidence for a Fisk-type heliospheric magnetic field. i. analyzing Ulysses/KET electron observations, *The Astrophysical Journal*, *741*, 23, 2011.

Stone, E. C., A. C. Cummings, F. B. McDonald, B. C. Heikkila, N. Lal, and W. R. Webber, An asymmetric solar wind termination shock, *Nature*, *454*, 71–74, 2008.

Strauss, R. D., and H. Fichtner, On aspects pertaining to the perpendicular diffusion of solar energetic particles, *The Astrophysical Journal*, *801*(1), 29, 2015.

Strauss, R. D., M. S. Potgieter, S. E. S. Ferreira, and M. E. Hill, Modelling anomalous cosmic ray oxygen in the heliosheath, *Astronomy and Astrophysics*, *522*, A35, 2010.

Strauss, R. D., M. Potgieter, A. Kopp, and I. Büsching, On the propagation times and energy losses of cosmic rays in the heliosphere, *Journal of Geophysical Research: Space Physics*, *116*, 12,105, 2011.

Strauss, R. D., M. Potgieter, and S. Ferreira, Modelling and observing Jovian electron propagation times in the inner heliosphere, *Advances in Space Research*, *51*(3), 339–349, 2013.

Strauss, R. D., O. Ogunjobi, H. Moraal, K. G. McCracken, and R. A. Caballero-Lopez, On the pulse shape of ground-level enhancements, *Solar Physics*, *292*(4), 51, 2017.

Sweby, P., High resolution schemes using flux limiters for hyperbolic conservation laws, *SIAM Journal on Numerical Analysis*, pp. 995–1011, 1984.

Taylor, G. I., The spectrum of turbulence, *Proceedings of the Royal Society of London Series A*, *164*, 476–490, 1938.

Teufel, A., and R. Schlickeiser, Analytic calculation of the parallel mean free path of heliospheric cosmic rays. ii. dynamical magnetic slab turbulence and random sweeping slab turbulence with finite wave power at small wavenumbers, *Astronomy and Astrophysics*, *397*, 15–25, 2003.

Thomas, B. T., and E. J. Smith, The parker spiral configuration of the interplanetary magnetic field between 1 and 8.5 au, *Journal of Geophysical Research: Space Physics*, *85*(A12), 6861–6867, 1980.

Torsti, J., et al., Energetic particle experiment ERNE, *Solar Physics*, *162*, 505–531, 1995.

Tousey, R., The solar corona., in *Space Research Conference*, *Space Research Conference*, vol. 2, edited by M. J. Rycroft and S. K. Runcorn, pp. 713–730, Berlin: Akademie-Verlag, 1973.

Townsend, L. W., et al., Solar particle event storm shelter requirements for missions beyond low Earth orbit, *Life Sciences and Space Research*, *17*, 32–39, 2018.

Trac, H., and U. Pen, A primer on Eulerian computational fluid dynamics for astrophysics, *Publications of the Astronomical Society of the Pacific*, *115*(805), 303, 2003.

Usoskin, I., A history of solar activity over millennia, *Living Reviews in Solar Physics*, *5*, 2008.

Vainio, R., Diffusive shock acceleration, in *Plasma Turbulence and Energetic Particles in Astrophysics*, edited by M. Ostrowski and R. Schlickeiser, pp. 232–245, 1999.

van den Berg, J., Modelling of solar energetic particles by stochastic processes, Master's thesis, North-West University, Potchefstroom, South Africa, 2018.

van Leer, B., Towards the ultimate conservation difference scheme. ii. monotonicity and conservation combined in a second-order scheme, *Journal of Computational Physics*, *14*, 361–370, 1974.

Wang, Q., Numerical methods for partial differential equations [lecture notes], uRL: https://learning-modules.mit.edu/materials/index.html?uuid=/course/16/fa17/16.920#materials. Last visited on 2018/05/10, 2017.

Wang, Y. M., Coronal holes and open magnetic flux, *Space Science Review*, *144*, 383–399, 2009.

Wang, Y. M., Semiempirical models of the slow and fast solar wind, *Space Science Review*, pp. 1–21, 2011.

Wang, Y. M., and N. R. Sheeley, Solar implications of Ulysses interplanetary field measurements, *The Astrophysical Journal*, *447*, 143, 1995.

Zhang, M., J. R. Jokipii, and R. B. McKibben, Perpendicular transport of solar energetic particles in heliospheric magnetic fields, *The Astrophysical Journal*, *595*(1), 493, 2003.

Zhang, M., G. Qin, and H. Rassoul, Propagation of solar energetic particles in three-dimensional interplanetary magnetic fields, *The Astrophysical Journal*, *692*(1), 109, 2009.